

AD_____

Award Number: W81XWH-07-1-0247

TITLE: Transrectal Near-Infrared Optical Tomography for Prostate Imaging

PRINCIPAL INVESTIGATOR: Daqing Piao, Ph.D.

CONTRACTING ORGANIZATION: Oklahoma State University
Stillwater, OK 74078

REPORT DATE: March 20F€

TYPE OF REPORT: Annual

PREPARED FOR: U.S. Army Medical Research and Materiel Command
Fort Detrick, Maryland 21702-5012

DISTRIBUTION STATEMENT: Approved for Public Release;
Distribution Unlimited

The views, opinions and/or findings contained in this report are those of the author(s) and should not be construed as an official Department of the Army position, policy or decision unless so designated by other documentation.

REPORT DOCUMENTATION PAGE				Form Approved OMB No. 0704-0188	
Public reporting burden for this collection of information is estimated to average 1 hour per response, including the time for reviewing instructions, searching existing data sources, gathering and maintaining the data needed, and completing and reviewing this collection of information. Send comments regarding this burden estimate or any other aspect of this collection of information, including suggestions for reducing this burden to Department of Defense, Washington Headquarters Services, Directorate for Information Operations and Reports (0704-0188), 1215 Jefferson Davis Highway, Suite 1204, Arlington, VA 22202-4302. Respondents should be aware that notwithstanding any other provision of law, no person shall be subject to any penalty for failing to comply with a collection of information if it does not display a currently valid OMB control number. PLEASE DO NOT RETURN YOUR FORM TO THE ABOVE ADDRESS.					
1. REPORT DATE (DD-MM-YYYY) 31-03-2010		2. REPORT TYPE Annual		3. DATES COVERED (From - To) 1 MAR 2009 - 28 FEB 2010	
4. TITLE AND SUBTITLE Transrectal Near-Infrared Optical Tomography for Prostate Imaging				5a. CONTRACT NUMBER W81XWH-07-1-0247	
				5b. GRANT NUMBER PC060814	
				5c. PROGRAM ELEMENT NUMBER	
6. AUTHOR(S) Daqing Piao Go ckn" f cslpi t kqB qmxcv g f w				5d. PROJECT NUMBER	
				5e. TASK NUMBER	
				5f. WORK UNIT NUMBER	
7. PERFORMING ORGANIZATION NAME(S) AND ADDRESS(ES) Oklahoma State University Stillwater, Ok 74078				8. PERFORMING ORGANIZATION REPORT NUMBER	
9. SPONSORING / MONITORING AGENCY NAME(S) AND ADDRESS(ES) U.S. Army Medical Research and Material Command Fort Detrick, Maryland 21702-5012				10. SPONSOR/MONITOR'S ACRONYM(S)	
				11. SPONSOR/MONITOR'S REPORT NUMBER(S)	
12. DISTRIBUTION / AVAILABILITY STATEMENT Approved for public release; distribution unlimited					
13. SUPPLEMENTARY NOTES					
14. ABSTRACT Purpose 1: to evaluate whether trans-rectal spectral optical tomography of total hemoglobin concentration [HbT] can be used to detect prostate cancer development. Findings: Spectral detection at 785nm and 830nm enabled quantitation of [HbT]. Canine TVT cells were injected into the right lobe of a dog's prostate gland. Longitudinal imaging assessment of the post-injection prostate was performed by trans-rectal US-coupled spectra optical tomography over a 45-day duration. The average [HbT] in an area of TVT concentrated tumor foci changed from 120 µM to 375 µM over the 45-day duration. Transrectal US-coupled spectral optical tomography seems capable of detecting the development and lateral involvement of prostate cancer earlier than by transrectal US alone. Purpose 2: to evaluate the challenges of the optical heterogeneities of prostate imposed on in vivo imaging of prostate cancer. Findings: a comprehensive review of the published data on optical properties of canine and human prostate is conducted. Purpose 3: to develop a theory of photon diffusion that accounts for the cylinder-shape applicator used in prostate imaging. Findings: a unified theory of steady-state photon diffusion for using cylinder-shape applicator to image internally or externally is developed.					
15. SUBJECT TERMS Prostate cancer, optical tomography, transmissible venereal tumor, ultrasound, hemoglobin					
16. SECURITY CLASSIFICATION OF:			17. LIMITATION OF ABSTRACT UU	18. NUMBER OF PAGES 82	19a. NAME OF RESPONSIBLE PERSON USAMRMC
a. REPORT U	b. ABSTRACT U	c. THIS PAGE U			19b. TELEPHONE NUMBER (include area code)

Table of Contents

	<u>Page</u>
Introduction.....	01
Body.....	01
Key Research Accomplishments.....	17
Reportable Outcomes.....	18
Conclusion.....	19
References.....	20
Appendices.....	22

ANNUAL REPORT

PCRP 060814----“Transrectal Near-Infrared Optical Tomography for Prostate Imaging”

INTRODUCTION

The objective of this research is to explore the technology of trans-rectal near-infrared (NIR) optical tomography for accurate, selective prostate biopsy. Prostate cancer is the most common non-dermatologic cancer in American men. Prostate cancer suspicion is typically based on an elevated serum prostate-specific antigen (PSA) level or a suspicious nodule found during a digital rectal exam (DRE). When the PSA level is elevated or the DRE shows abnormal, there is a 25 % chance that cancer is present. The existence of prostate cancer can only be confirmed by a needle biopsy that is guided by trans-rectal ultrasound (TRUS). Since there are no pathognomonic findings for prostate cancer on ultrasound imaging, biopsies are taken following a systematic pattern throughout the prostate with preference given to the peripheral zone wherein most cancer are found. The accuracy of biopsy is questionable and many men undergo multiple biopsies due to the lack of a more specific/sensitive imaging modality. Pathologic studies have demonstrated positive correlation between increased micro-vessel density and the onset of the disease. Near-infrared (NIR) optical tomography is known of sensitive to blood-based contrast, therefore trans-rectally implemented NIR optical tomography may provide a new way of assessing the prostate cancer. One of the outcomes of trans-rectal NIR tomography of the prostate would be a more accurate imaging guidance for targeted prostate biopsy.

BODY

1. Proposed specific aims:

- (1) To demonstrate that endoscopic NIR tomography at a probe size of 25mm in diameter can be achieved by use of spread-spectral-encoding from a broad-band light source. (*Completed by year 2*)
- (2) To demonstrate that trans-rectal NIR tomography can image the prostate at the proximity of the rectum with significant tumor-tissue contrast. (*Completed by year 2*)
- (3) To demonstrate that multi-spectral trans-rectal NIR tomography can be implemented with the single trans-rectal imaging probe. (*Completed in year 3*)
- (4) To demonstrate that trans-rectal multi-spectral NIR tomography can quantify the hemoglobin concentration and oxygenation saturation in phantom, and further in prostate tumor model if the time of research allows. (*Hemoglobin part completed in year 3, oxygen-saturation part on-going*)

2. Development of spectral trans-rectal optical tomography for coupling to trans-rectal ultrasound

The transrectal US-coupled applicator for this study was the same as that utilized in our previous studies [1]. The trans-rectal NIR/US applicator development is based on a commercially available biplane prostate probe (ALOKA UST 672-5/7.5), as illustrated in Fig. 1(a). The NIR source and detector channels are placed laterally symmetric to the sagittal US transducer allowing optical tomography at the mid-sagittal plane to align precisely with the sagittal US. The configuration of the spectral optical tomography imager is provided in Fig. 1(b). The outputs of a 785nm and a 830nm laser diode are combined using a bifurcated fiber, and sequentially delivered to the 7 NIR source channels via a linear-translation fiber switch. The 7 NIR detector channels are coupled to a spectrograph of 300mm focal-length and 300 lines/mm grating, which separated the 7-channel dual-band light onto an intensified CCD camera with 12mm×12mm chip size and 16-bit resolution. The data acquisition from all 7 source channels is completed in 3 seconds. The

absorption coefficients at 785nm ($\mu_a^{\lambda_1}$) and 830nm ($\mu_a^{\lambda_2}$) are reconstructed separately, then concentrations of the oxygenated and deoxygenated hemoglobin are calculated by

$$[HbO] = \left[\mu_a^{\lambda_1} \cdot e^{\lambda_2}_{Hb} - \mu_a^{\lambda_2} \cdot e^{\lambda_1}_{Hb} \right] / \left[e^{\lambda_1}_{HbO} \cdot e^{\lambda_2}_{Hb} - e^{\lambda_2}_{HbO} \cdot e^{\lambda_1}_{Hb} \right], \quad (1)$$

and

$$[Hb] = \left[\mu_a^{\lambda_1} \cdot e^{\lambda_2}_{HbO} - \mu_a^{\lambda_2} \cdot e^{\lambda_1}_{HbO} \right] / \left[e^{\lambda_1}_{Hb} \cdot e^{\lambda_2}_{HbO} - e^{\lambda_2}_{Hb} \cdot e^{\lambda_1}_{HbO} \right], \quad (2)$$

respectively, where e^{λ} denotes the molar extinction coefficient as shown in Fig. 1(c). Summation of these two concentration values leads to [HbT].

The [HbT] measurement was calibrated using different concentrations of fresh bovine blood [2], whose optical absorption spectra in 780-840nm are considerably close to that of human blood [3]. The bovine blood was held in a cylindrical container fabricated out of a tissue-mimicking material, which was placed in bulk Intralipid solution with optical properties similar to typical soft tissue. The [HbT] measurements were performed at different locations and distances of the blood-container with respect to the NIR applicator. On average, a linear relationship was established between the measured and set values of [HbT], above a residual as is shown in Fig. 1(d).

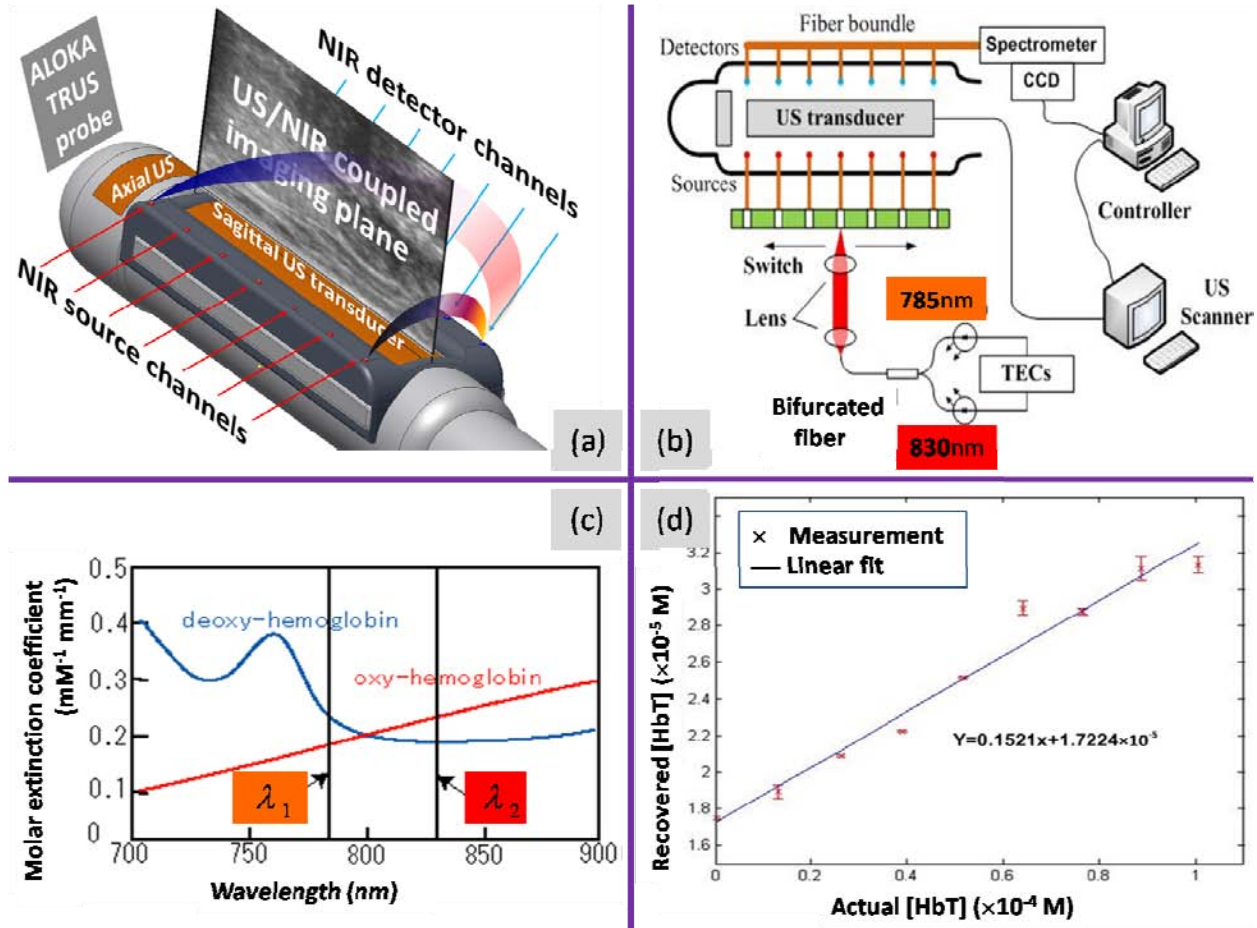


Figure 1. (a) A 3-D rendering of TRUS-coupled NIR imaging. (b) Schematic diagram of the spectral optical tomography system. (c) Dual-bands used for spectral optical tomography. (d). [HbT] calibration using bovine blood.

3. Assessing the lateral involvement and longitudinal changes of transmissible venereal tumor in a canine prostate by trans-rectal ultrasound-coupled spectral optical tomography of total hemoglobin concentration

There is strong pathological evidence to suggest that vascular supply to malignant prostate tissue differs from vascular anatomy of normal prostatic tissue [4]. Doppler sonography, as an adjunct to gray-scale sonography, is thereby used to identify increased blood flow and assist in the identification of suspicious lesions within the prostate. Studies of microvessel density within the prostate demonstrated a clear association of increased microvessel density with the presence of cancer [5]. Doppler imaging is able to detect signal from small vessels such as those feeding vessels to the microvascular bed, but due to its sensitivity dependence upon motion, it may not detect signals from the microcirculation itself [6, 7].

In the near-infrared (NIR) band, light interacts with tissue at the microscopic level, largely by two mechanisms: strong scattering by subcellular organelles and the dominant absorption by chromophores such as hemoglobin molecules. It has been well recognized in breast imaging [8] that an increased level of hemoglobin concentration in the micro-vasculature of breast cancer causes an elevation of NIR absorption and alteration of NIR scattering. For a sonographically-suspicious lesion in breast tissue, including total hemoglobin concentration [HbT] measured by NIR optical tomography is shown to improve the specificity of breast cancer detection [9]. These findings suggest that augmenting TRUS with NIR measurement of [HbT] in the prostate will likely improve accuracy of detecting prostate cancer. Our recent studies have demonstrated that combining trans-rectal NIR absorption measurement of prostatic tissue at 840nm with ultrasonography detected development of a transmissible venereal tumor (TVT) in a canine prostate at least a week earlier than by using TRUS alone [1]. The much denser cellular morphology of TVT was related partially to NIR absorption change seen in that study, but association of [HbT] with that change was not quantified due to the use of a single-band NIR measurement. In this study, the trans-rectal NIR absorption measurement is performed spectrally at 785nm and 830nm which is necessary for extracting the [HbT] of prostatic tissue. This study demonstrates that combining trans-rectal NIR measurement of the prostatic [HbT] and ultrasonography will likely detect lateral involvement and predict longitudinal development of TVT in canine prostate earlier and collectively more accurately than by using TRUS alone.

3.1 Animal Model and Imaging Protocol

This study was approved by the Institutional Animal Care and Use Committee of Oklahoma State University. The canine protocol was also inspected on-site by the U.S. Army Medical Research and Material Command. An adult 20-kg, intact male, foxhound estimated to be six years of age was used. The canine TVT cells were propagated in NOD/SCID mice and recovered/homogenized for injection into the non-immune suppressed dog's prostate gland. Under general anesthesia, ~2 cc of TVT cells (approximately 5×10^6 TVT cells) were aseptically injected transperineally into the right lobe of the prostate using a 6-in. 18-gauge hypodermic needle (Fig. 2(a)), via US visualization using an Aloka UST-9132I convex array multi-frequency (3.75-10 MHz) finger-grip transducer (US image in Fig. 2(b)). The TVT cells were confined within the right prostatic lobe during the injection in two locations, one near the cranial aspect, and the second slightly caudal to the mid-point of the right lobe as the needle was withdrawn (Fig. 2(a)). The dog then underwent serial monitoring, including digitally palpated transrectal examination, transrectal US and trans-rectal optical tomography, at 7, 14, 21, 31, 38, and 45 days post-injection. Doppler US evaluations were performed at and after 38 days post-injection.

The base-line US indicated that the prostate measured 6cm from cranial to caudal. The base-line US also revealed a cluster of prostatic cysts resembling a "face" in the right aspect of the gland. This "face" landmark, the location of which is shown in Fig. 2(c), facilitated multiple images taken in the same relative areas in that location over time throughout the course of the imaging study. Transrectal optical tomography was performed on five quasi-sagittal planes across the prostate, including the middle-sagittal plane, half-way to the right lateral edge, the right lateral edge, half-way to the left lateral edge, and the left lateral edge, of the prostate gland as shown in Fig. 2(d). On each of the five quasi-sagittal planes, the imaging was

performed at three different longitudinal positions of the prostate with respect to the applicator for cross-validation.

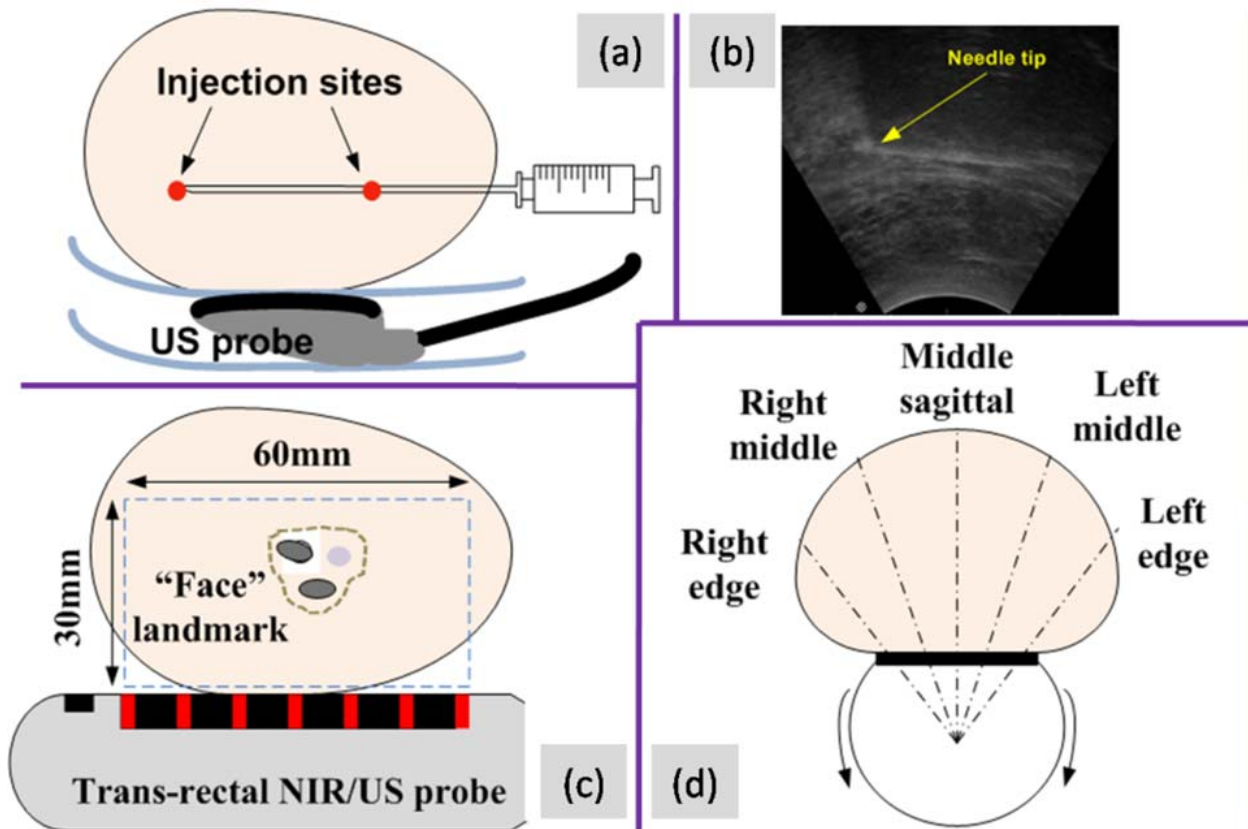


Figure 2. (a) The two sites of TVT injection. (b) Needle visualized. (c) The “face” landmark. (d) The five quasi-sagittal planes followed in optical imaging.

3.2 Pathological Assessment

The dog was humanely euthanized using a barbiturate overdose at 55-days post-inoculation followed by thorough gross inspection and excision of the prostate gland and urinary bladder. The prostate was serially sectioned by freehand technique in transverse planes. These planes were considered orthogonal to the quasi-sagittal planes used for transrectal US-coupled optical tomography. Routine histology with hematoxylin and eosin stain for light microscopy was performed on specimens selectively sampled from the sectioned prostate, each of which contained tissues that were grossly expected to be normal, cystic or neoplastic.

3.3 Results

Among the US/NIR images, only the representative sets corresponding to 7-days and 31-days post-injection are presented in Fig. 3. Each group of images for the 7-days and 31-days were taken at two positions, as indicated by the ~25mm shift of the “face” landmark. On US, the “face” landmark was clearly visible by 7-days but distorted significantly by 31-days. The 7-day image revealed a region with higher [HbT] in NIR images and hypo-echoic, near the cranial injection site in the right lobe. That region-of-interest was not visible in images taken at 14-days and thereafter, most likely due to hemorrhage and inflammation at the injection site.

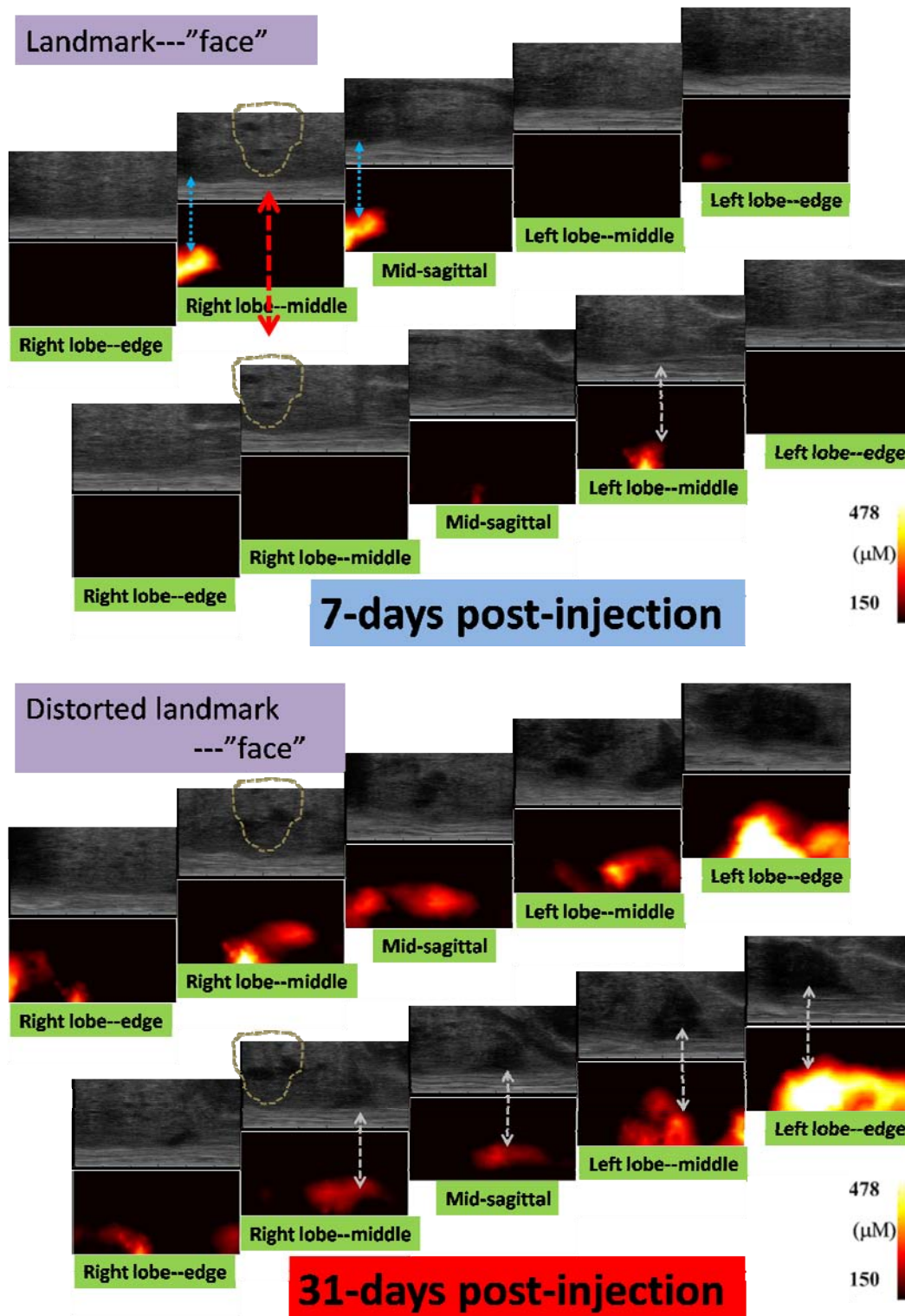


Figure 3. Image dimension----60mm×30mm (canial-caudal×dorsal-ventral). At 7-days post-injection, NIR detected a hyper-[HbT] region in the cranial injection site which later disappeared. In the left lobe the 7-days NIR image indicated a tumor growth. Both NIR and US later revealed more volume involvement in the left-lobe than in the right lobe.

The US images at 31-days post injection revealed a cluster of hypoechoic masses with irregular-boundaries in the caudal aspect of both right and left lobe, and overall greater volume of the hypoechoic masses in the left than in the right lobe. The spatial content of the NIR hyper-[HbT] regions generally agree with that of the US hypo-echoic regions in the caudal-to-middle-left aspect of the gland, but presented a different pattern in the cranial-to-right aspect of the gland. The US presented a large hetero-echoic mass dorsal-cranial to the pelvic bone and extending predominantly to the left lobe but also had right-lobe involvement. Near that location the corresponding NIR image revealed a cluster of hyper-[HbT] region, but the center of which seemed displaced slightly cranially with respect to that of US hypo-echoic mass. Retrospectively, in the 7-days NIR images, a smaller but stronger hyper-[HbT] region was found near that location. Also, when considering the 7-days US images, a substantially smaller hypoechoic region was weakly distinguishable near that location. Finally, in the 7-days images, the location of the hyper-[HbT] region was displaced slightly cranially with respect to that of the marked US hypoechoic mass. This hypoechoic mass, developing much more rapidly than other masses, presented marked enhancement of peripheral blood flow when imaged by Doppler US at 38-days post-injection.

Figure 4 illustrates the changes of [HbT] from baseline to 45-days post-injection in a marked 10mm-diameter region located in the right lobe, that correlated to the US hypo-echoic mass observed caudal to the prostate. The average [HbT] in this region changed from 120 μM to 375 μM , a nearly 300% change over the 45-days of development. The [HbT] values obtained in this study agree with the range indicated by other similar projects [10].

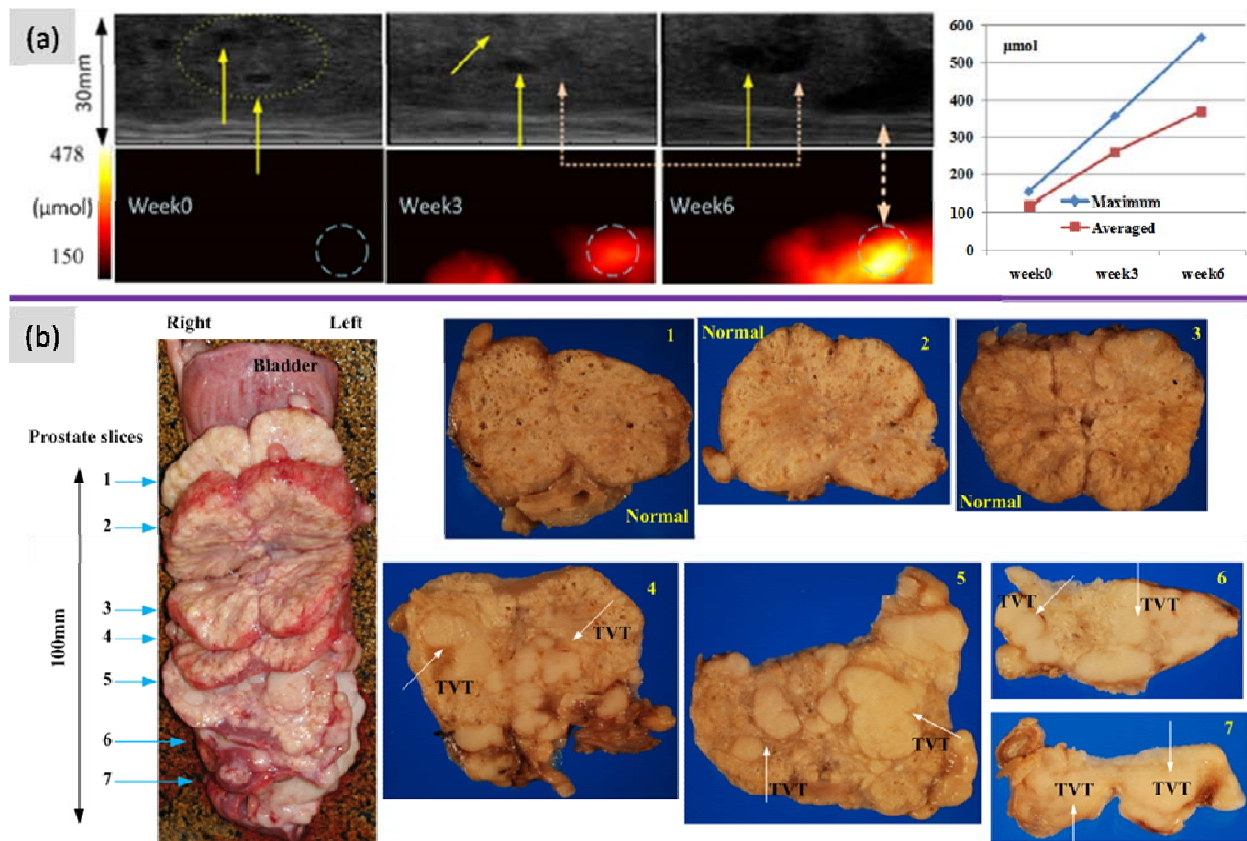


Figure 4. (a) Longitudinal [HbT] changes in the 10mm-diameter region-of-interest. (b) Gross examination of the canine prostate. The 7 slices of the prostate gland were sectioned from cranial to caudal, at an interval of approximately 15mm. TVT-transmissible venereal tumor.

The excised prostate (Fig 4(b)) was approximately 10cm in length \times 5cm in width \times 5cm in depth. The prostate was step-sectioned into approximately 1.5cm slices. The gross examination confirmed multiple coalescing foci of TVT in the caudal aspect of the gland, and significant infiltration of the tumor from the right to the left lobe. The histology confirmed TVT.

3.4 Comments and Conclusions

Angiogenesis is essential for tumor growth and metastasis. Recent longitudinal studies of the prostate cancer developmental phase suggested that neoangiogenesis or tumor-associated neovascularity must increase before rapid growth of tumor [11]. Retrospectively in this study, the lateral development of TVT was indicated earlier on NIR than on grey-scale US. The marked vascularity enhancement of the TVT seen on Doppler is primarily in the periphery of the hypo-echoic TVT foci, but the elevation of [HbT] on NIR was found almost always distributed in the entire TVT infiltrated region. This is an indication that the attenuation of NIR light is directly associated with [HbT]. The NIR imaging may therefore detect the onset of neo-vasculature before the size of the vessels are detectable using other noninvasive imaging techniques such as ultrasound, providing earlier prediction of lateral and longitudinal changes.

In conclusion, this study demonstrated a non-invasive optical measurement of [HbT] changes associated with tumor development in the canine prostate. Using transrectal US-coupled spectral optical tomography the development and lateral involvement of the prostate cancer was detected earlier than using transrectal US alone.

4. Review of Optical Properties of Canine and Human Prostates

Using light to image prostate is underlined by that a benign and cancerous prostate tissues present different optical properties which can be resolved by means of optical interrogation. Revealing the contrast of prostate cancer over normal tissue will be challenging if significant base-line heterogeneities exist in the optical properties of benign tissues. There have been a number of studies on prostate optical properties in which certain consensuses have been made. Although these studies are conducted at different wavelengths, different samples, and different methods, spectrally these studies shall offer information invaluable to understanding the potentials of detecting prostate cancer as well as difficulties facing the optical imaging of prostate. In this section, we give a side-by-side review of the known optical properties of canine and human prostates.

4.1 Review of optical properties of canine prostate

Dogs have been used in a number of prostate studies because of the similarity between canine and human prostate glands. We have summarized the studies previous to ours on optical properties.

Tables 1 and 2 summarize what the authors have found to be existing methods, represented graphically by diagram (Table 1), and published values (Table 2) on optical properties of the canine prostate within the spectral range from 355nm to 1064nm. In Table 2, the attenuation coefficient is denoted by μ_a , the reduced scattering coefficient by μ'_s , and the effective attenuation coefficient by μ_{eff} that is defined as

$$\mu_{eff} = \sqrt{3\mu_a(\mu_a + \mu'_s)} \quad (3)$$

Oraevsky et al. presented *in vitro* μ_a , μ'_s , and μ_{eff} of prostate at 355, 532, and 1064 nm, respectively, using opto-acoustic time-resolved fluence rate measurements on slab samples of normal canine prostate tissues [12]. Another post-mortem study by Chen et al. estimated prostate μ_a , μ'_s , and μ_{eff} at 630 nm, by interstitial measurements on excised normal prostate [13]. *In vitro* μ_a and μ'_s of slab samples of normal canine prostate tissues were evaluated at 633 nm, by employing steady-state fluence rate measurements using the standard double-integrating sphere technique [15]. Other studies relied on steady-

state fluence rate measurements on tissues *in situ*, albeit involving surgical procedures to expose the prostatic tissue to the fiber, to determine μ_{eff} of the normal canine prostate. At wavelengths of 630, 665, 730, 732nm, interstitial measurements on normal canine prostate *in vivo* were conducted before and after PDT [14, 17, 18, 20]. Perhaps the only *in vivo* study using reflection measurement upon exposed prostate, thereby maintaining the intactness of the gland itself, was performed at 732nm on exposed normal canine prostate.¹⁹ Trans-perineal interstitial measurement [16-18], which in principle is more accurate than interstitial measurement on exposed prostate, demonstrated with statistical significance that the μ_{eff} of prostatic urethral regions is higher than that of the prostatic capsular regions [16, 17].

In Table 2, there were some individual values of μ_a and μ'_s , but nevertheless most original values listed were regarding μ_{eff} only, which were readily available from steady-state fluence rate measurements. Because the data were clustered in a wide spectrum, summarizing all these studies to a single category for spectrally-resolved comparative evaluation can only be made by utilizing μ_{eff} since it represents the coupled effect of μ_a and μ'_s . When the standard deviations of μ_a and μ'_s , denoted by $\sigma\mu_a$ and $\sigma\mu'_s$, respectively, are available, the standard deviation of μ_{eff} in Table 2 is calculated based on (1) by

$$\sigma\mu_{eff} = \sqrt{\left(\frac{\partial\mu_{eff}}{\partial\mu_a}\sigma\mu_a\right)^2 + \left(\frac{\partial\mu_{eff}}{\partial\mu'_s}\sigma\mu'_s\right)^2} \quad (4)$$

Table 1. Legend indicating the measurement methods used in Table 2







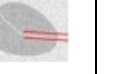

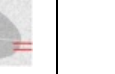


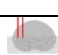
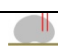
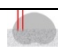









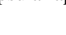
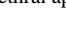
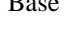





								
Opto-acoustic on slab tissue	Integrating sphere on slab tissue	Interstitial on exposed prostate	Interstitial on excised prostate	Reflective on exposed prostate	Interstitial close to the capsule	Interstitial close to the urethra	Interstitial close to the base	Interstitial close to the apex

Table 2. Optical properties of normal canine prostate tissue as reported in various published studies. N is the number of samples. This table follows the template for human prostate in Ref. 10.

Study	Year	Sample	N	Method	λ (nm)	μ_a (mm ⁻¹)	μ'_s (mm ⁻¹)	μ_{eff} (mm ⁻¹)
Oraevsky et al. [12]	1997	In vitro	2		355	0.852	5.22	3.94
Oraevsky et al. [12]	1997	In vitro	2		532	0.233	2.45	1.37
Chen et al. [13]	1997	In vivo	17		630	0.04±0.02	2.6±2.1	0.5±0.1
Chen et al. [13]	1997	Ex vivo	10		630	0.030±0.007	2.6±0.8	0.48±0.09
Lee et al. [14]	1997	In vivo	7		630			0.47±0.05

Nau et al. [15]	1999	In vitro (fresh)	10		633	0.073±0.007	0.225±0.005	0.256±0.015*
Nau et al. [15]	1999	In vitro (frozen)	13		633	0.076±0.003	1.00±0.11	0.495±0.027*
Lilge et al. [16]^	2004	In vivo	7	 Capsule	660	0.0030±0.0021	0.92±0.65	0.184±0.040^
Lilge et al. [16]^	2004	In vivo	7	 Urethra	660	0.0014±0.0013	3.23±2.76	<u>0.206±0.035^</u>
Jankun et al. [17]	2004	In vivo	13	 Capsule	665			0.171±0.071
Jankun et al. [17]	2004	In vivo	13	 Urethra	665			<u>0.192±0.027</u>
Jankun et al. [17]	2004	In vivo	13	 Capsular base	665			0.259±0.193
Jankun et al. [17]	2004	In vivo	13	 Urethral base	665			<u>0.275±0.131</u>
Jankun et al. [17]^^	2004	In vivo	13	 Capsular apex	665			0.176±0.031^ ^
Jankun et al. [17]	2004	In vivo	13	 Urethral apex	665			<u>0.190±0.065</u>
Jankun et al. [18]	2005	In vivo	5	 Base	665			0.247±0.06
Jankun et al. [18]	2005	In vivo	5	 Apex	665			0.203±0.026
Solonenko et al. [19]	2002	In vivo	4	 Base	730		1.27±0.06	
Zhu et al. [20]	2003	In vivo	12	 Base	732	0.003--0.058	0.1---2.0	0.03---0.49
Nau et al. [15]	1999	In vitro (fresh)	7		1064	0.027±0.003	1.76±0.13	0.381±0.026*
Nau et al. [15]	1999	In vitro (frozen)	10		1064	0.071±0.006	0.79±0.05	0.428±0.023*
Oraevsky et al. [12]	1997	In vitro	2		1064	0.009	0.63	0.13

* Calculation of the effective attenuation coefficient based on equations (1) and (2)

^ The values in the abstract of [16] are contrary to those in the text of [16]. The results in the text were used here.






^^ The results given in [17] were “0.176±0.314mm⁻¹”, which had the standard deviation larger than the mean value. The authors made a “reasonable” estimation of “0.176±0.0314mm⁻¹” for this set of literature data.

4.2 Review of optical properties of human prostate

The published values on optical properties of human prostate, all acquired invasively as illustrated in Table 3, are summarized in Table 4 [21], which enriched the template given in [10] with latest studies. The studies summarized in Table 4 include: (1) *Ex vivo* steady-state measurements of μ_{eff} and $\mu'_t = \mu_a + \mu'_s$ at 633 nm in three whole, nonmalignant human prostates [22]; (2) Three post-mortem studies estimating prostate optical properties (μ_a , scattering coefficient μ_s , scattering anisotropy g , and μ'_s) at 640nm (BPH) [23] and 1064 nm (normal prostate) [24, 25], by measuring through thin prostate slices; (3) μ_{eff} of prostate *in vivo* diagnosed with BPH or PCa estimated at 633nm by steady-state interstitial measurements [26, 27] that indicated similar μ_{eff} between benign and malignant prostate tissues; (4) At wavelengths of 630, 665, 732, 762nm, trans-perineal interstitial steady-state measurements on prostate *in vivo* with untreated BPH, untreated PCa, recurrent PCa conducted before and after PDT [27-31] to determine μ_{eff} or both μ_a and μ'_s ; (5) μ_a , μ'_s , and μ_{eff} of untreated PCa *in vivo* at 660, 786, 830 and 916 nm, respectively, using time-resolved fluence rate measurements [10, 32]; (6) a few studies on hemoglobin and oxygen saturation [10, 30, 31] indicating relatively small variations of oxygen saturation but large variations on total hemoglobin concentration within the same gland or different subjects. Recently interstitially measured 2-D or 3-D distribution of μ_a , μ'_s in human prostate are reported [33, 34] for PDT dosimetry.

Studies [29, 31] have indicated that the optical properties of canine prostate and human prostate may be substantially different, specifically the absorption. It is noted that the studies of canine prostate optical properties have been performed all on normal gland, but that of human include both normal, benign hyperplastic, and malignant prostate tissues. It is also noted that these studies are conducted at different wavelengths, different methods, on *ex vivo* or *in vivo* samples. Direct wavelength-specific and tissue-specific comparisons of the canine and human prostate optical properties are thereby difficult, but nonetheless the spectra of the optical properties of canine and human prostate may reveal useful information. To facilitate spectral comparison, for those original measurements of human prostate shown in Table 4 that have only the absorption and reduced scattering coefficients available, the effective attenuation coefficient is calculated following the method in Table 2. Figure 5 (b) illustrates the spectra of μ_a , μ'_s , and μ_{eff} of human prostates that are averaged for existing data at a specific wavelength. The distributions of the optical properties of both canine and human prostates are substantially large as seen in Table 2 and Table 4, and are not plotted in Fig. 5.

Table 3. Legend indicating the measurement methods used in Table 2.











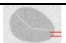





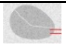







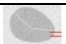















				
Integrating sphere on slab tissue	Interstitial on excised prostate	Interstitial trans-perineally on prostate	Steady-state fluence rate measurement	Time-resolved fluence rate measurement

The spectra shown in Fig. 5 are the invasively characterized optical properties of normal canine prostates and mostly malignant human prostates. The similarity or dissimilarity between canine and human prostate optical properties is difficult to draw as the optical properties of malignant canine prostate tissue were previously unavailable; however previous studies that are summarized in Tables 2 and 4 and seen in Fig. 5 have important implications to optical interrogation of the prostate in the following aspects:

- (1). The reduced scattering coefficient of prostate is approximately an order higher than the absorption coefficient of prostate. As this has been confirmed by time-resolved measurements, the prostate can be treated as a scattering-dominant tissue, thereby diffuse optical methods can be applied to modeling the photon propagation as in PDT and image reconstruction in trans-rectal imaging of the prostate.

Table 4. Current “invasive” knowledge of the optical properties of human prostate
(expanded upon the template in [10]).

PCa---prostate cancer; BPH--benign prostatic hyperplasia; UT—untreated; RC—recurrent.

Study	Year	Sample	Path	N	Method	Photon	λ (nm)	μ_a (mm ⁻¹)	μ_s (mm ⁻¹)	μ_{eff} (mm ⁻¹)
Lee [28]	1999	<i>In vivo</i>	PCa	7			630			0.35±0.07 (0.22-0.44)
Pantelides [22]	1990	<i>Ex vivo</i>	Normal	3			633	0.07±0.02	0.86±0.05	0.43±0.05
Whitehurst [26]	1994	<i>In vivo</i>	BPH PCa	11			633			0.35±0.02 0.36±0.02
Lee [27]	1995	<i>In vivo</i>	BPH PCa	11			633			0.39±0.05 (0.24-0.42)
Wei [23]	2008	<i>In vitro</i>	BPH	?			640	0.44~0.96	1.12~1.66	2.09±0.54
Svensson [10]	2007	<i>In vivo</i>	PCa	9			660	0.05±0.01	0.87±0.19	0.36±0.08
Svensson [32]	2008	<i>In vivo</i>	PCa	1			660	~0.032	~0.5-1.4	0.23-0.37
Lee [27]	1995	<i>In vivo</i>	BPH UT PCa	11			665			0.32±0.05 (0.24-0.42)
Zhu [29]	2005	<i>In vivo</i>	RC PCa	13			732	0.037±0.024 (0.007—0.162)	1.40±1.10 (0.11—4.4)	0.29±0.07 (0.091—0.67)
Zhu [30]	2005	<i>In vivo</i>	RC PCa	2			732	0.011—0.16	0.12—4.0	0.019—0.63
Li [33]	2008	<i>In vivo</i>	RC PCa	1			732	2-D map 0.01—0.1	2-D map 0.5—4.5	0.65±0.37
Wang [34]	2009	<i>In vivo</i>	RC PCa	1			732	3-D map 0.01—0.07	3-D map 0.1—5.5	0.19-0.41
Weersink [31]	2005	<i>In vivo</i>	RC PCa	22			762	0.039±0.018	0.34±0.16	0.20±0.06
Svensson [10]	2007	<i>In vivo</i>	PCa	9			786	0.04±0.01	0.71±0.16	0.29±0.07
Svensson [32]	2008	<i>In vivo</i>	PCa	1			786	0.025	0.35-1.2	0.17-0.30
Svensson [32]	2008	<i>In vivo</i>	PCa	1			830	0.034	0.25-1.0	0.17-0.32
Svensson [10]	2007	<i>In vivo</i>	PCa	9			916	0.06±0.01	0.77±0.18	0.38±0.08
Svensson [32]	2008	<i>In vivo</i>	PCa	1			916	0.042	0.24-0.9	0.19-0.34
Essebpres [24]	1992	<i>Ex vivo</i>	Normal	?			1064	0.15±0.02	0.64	0.60
Roggan [25]	1995	<i>Ex vivo</i>	Normal	?			1064	0.03	0.4	0.2

(2). There are noticeable inter-subject and intra-organ heterogeneities in optical properties of prostate. The intra-organ heterogeneity poses a substantial challenge to differentiating malignant tissue from normal tissue, since the optical contrast of the malignant tissue over the normal tissue must be greater than the background heterogeneity for the malignant lesion to be resolved. The intra-organ heterogeneity may also partially contribute to the previous finding that the effective attenuation coefficients of benign and malignant human prostate tissues were similar. It is noted that none of the previous measurements of prostate optical heterogeneities have been examined on intact prostate *in vivo*. Our approach of trans-rectal near-infrared diffuse optical tomography, which aims at imaging the intact prostate in its real-time *in vivo* condition, shall demonstrate if and which type of intrinsic optical property contrasts are available for differentiating the malignant prostatic tissue from benign tissue.

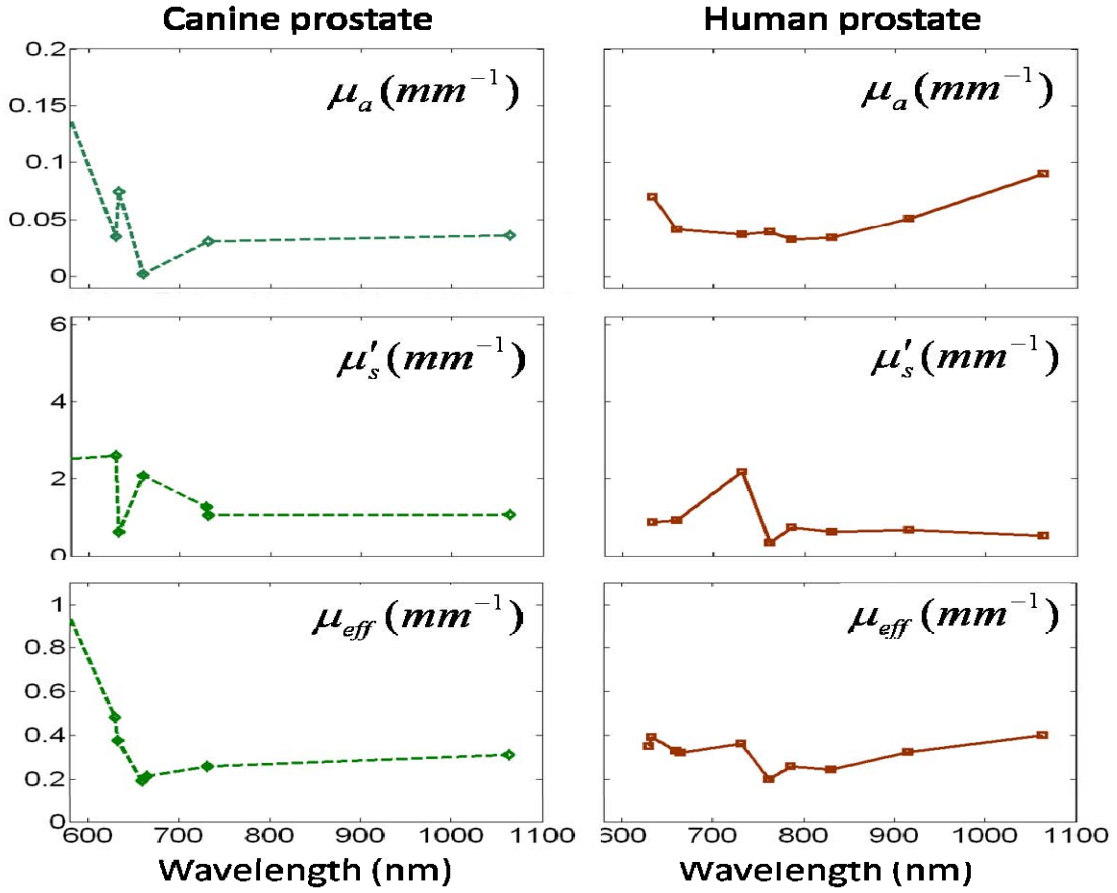


Figure 5. The optical properties, including absorption, reduced scattering, and effective attenuation coefficients, averaged for existing studies at available spectral band for canine (a) and human (b). The canine data is of normal tissue only, but the human data is of benign and malignant tissues.

5. Photon diffusion in a homogenous medium bounded externally or internally by an infinitely long circular cylindrical applicator---model advancement for prostate imaging

In this work the photon diffusion is analyzed in both external and internal imaging geometries, wherein the medium being interrogated is bounded either externally or internally by an infinitely long circular cylindrical applicator. These two geometries resemble imaging the breast using a ring-shape applicator and imaging the prostate using an endo-rectal probe, respectively. Photon diffusion models applicable to breast-imaging using a ring-shape applicator has been described, but that applicable to prostate-imaging using endo-rectal probe was not reported before. This work develops a unifying theory of photon diffusion that applies to both external and internal imaging when the applicator is an infinitely long circular cylinder---an idealized representation.

These studies are conducted initially for steady-state photon diffusion only, which is nonetheless adequate in terms of assessing the effect of the cylindrical interface on photon fluence rate when compared with semi-infinite boundary. The Green's function of the photon diffusion equation in an infinite medium geometry is first expanded in cylindrical-coordinates to a closed form expressed by the modified Bessel functions. Then the extrapolated boundary condition is employed, to apply the image-source method, to the geometries of “concave” cylindrical applicator and “convex” cylindrical applicator, respectively. The analytic solutions are then simplified, valid for large cylinder diameters, to a format that includes the physical source and its image source with respect to the associated semi-infinite geometry, and a radius-dependent term to account for the shape and dimension of the cylinder. The simplified format reveals that, as the radius of the cylinder increases, the analytic solution of the photon diffusion for it approaches the well-known semi-infinite result. The analytic solutions and their simplified formats are then evaluated numerically for two specific geometries, one having the source and the detector on the surface positioned only along the azimuthal direction and the other along the longitudinal direction, respectively. Placing the source-detector either azimuthally or longitudinally demonstrates explicitly the effect of the applicator curvature, either concave or convex, and the radius of the applicator curvature on the decay of photon fluence rate as a function of the source-detector distance, in comparison to that in the semi-infinite geometry. As the radius of the cylindrical applicator increases, the numerically evaluated photon diffusion for it asymptotically approaches that for a semi-infinite geometry, as expected.

5.1 Summary of the solutions of steady-state photon diffusion in cylindrical-coordinates

Considering a source at \vec{r}' of (ρ', ϕ', z') and a detector at \vec{r} of (ρ, ϕ, z) in cylindrical-coordinates, the steady-state photon fluence rate in an infinite homogenous medium is:

$$\Psi = \frac{S}{2\pi^2 D} \int_0^\infty dk \cos[k(z - z')] \cdot \sum_{m=0}^\infty \varepsilon_m I_m(k_{eff} \rho_<) K_m(k_{eff} \rho_>) \cos[m(\phi - \phi')] \quad (5)$$

where S is the source, Ψ is the photon fluence rate at position \vec{r} , $D = [3(\mu_a + \mu'_s)]^{-1}$ is the diffusion coefficient, μ_a is the absorption coefficient, μ'_s is the reduced scattering coefficient, $I_m(k_{eff} \rho)$ and $K_m(k_{eff} \rho)$ are the first and second kinds of modified Bessel functions, respectively, and $\rho_<$ and $\rho_>$ indicate the smaller and larger radial coordinates of the source and the detector.

The steady-state photon fluence rate in a concave geometry imposed by an infinitely long circular cylindrical applicator for interrogating the medium internal to the applicator (e.g. breast imaging) is:

$$\Psi = \frac{S}{2\pi^2 D} \int_0^\infty dk \left\{ \cos[k(z-z')] \cdot \sum_{m=0}^\infty \varepsilon_m I_m[k_{eff}(R_0 - R_a)] K_m(k_{eff} R_0) \cdot \left\langle 1 - \frac{I_m(k_{eff} R_0)}{K_m(k_{eff} R_0)} \frac{K_m[k_{eff}(R_0 + R_b)]}{I_m[k_{eff}(R_0 + R_b)]} \right\rangle \cos[m(\varphi - \varphi')] \right\} \quad (6conC)$$

The steady-state photon fluence rate in a convex geometry imposed by an infinitely long circular cylindrical applicator for interrogating the medium external to the applicator (e.g. prostate imaging) is:

$$\Psi = \frac{S}{2\pi^2 D} \int_0^\infty dk \left\{ \cos[k(z-z')] \cdot \sum_{m=0}^\infty \varepsilon_m I_m[k_{eff} R_0] K_m[k_{eff}(R_0 + R_a)] \cdot \left\langle 1 - \frac{K_m(k_{eff} R_0)}{I_m(k_{eff} R_0)} \frac{I_m[k_{eff}(R_0 - R_b)]}{K_m[k_{eff}(R_0 - R_b)]} \right\rangle \cos[m(\varphi - \varphi')] \right\} \quad (6conV)$$

If the concave or convex geometry has large radial dimension, the photon fluence rate expressed by (6conC) and (6conV) can be approximated to

$$\Psi = \frac{S}{4\pi D} \frac{e^{-k_0 l_r}}{l_r} - \frac{S}{4\pi D} \frac{e^{-k_0 l_i}}{l_i} \sqrt{\frac{R_0 + R_a + 2R_b}{R_0 - R_a}} \quad (7conC)$$

$$\Psi = \frac{S}{4\pi D} \frac{e^{-k_0 l_r}}{l_r} - \frac{S}{4\pi D} \frac{e^{-k_0 l_i}}{l_i} \sqrt{\frac{R_0 - R_a - 2R_b}{R_0 + R_a}} \quad (7conV)$$

where l_r is defined as the distance from the detector to the “real” isotropic source, and l_i as the distance from the detector to the image source of the “real” isotropic source associated with the semi-infinite geometry that is tangential to the concave or convex geometry on the physical source point.

5.1 Steady-state photon diffusion in the “concave” and “convex” geometries-----numerical evaluation of the cylindrical-coordinates solutions

We also numerically evaluated the general solutions (6) for the geometries having smaller cylinder radius and their approximations in (7) for the geometries having very large cylinder radius. These evaluations, for simplicity, are limited to two cases: (1) the source and detector locate at the same azimuth plane; (2) the source and detector locate longitudinally with the same azimuthal angle. The results indicate how the circular boundary affects the photon fluence rate with respect to a semi-infinite boundary, and justify qualitatively these analytic solutions and their approximations.

The geometries shown in Fig. 6 are chosen to study the effect of concave or convex boundary shape on photon diffusion for the source and detector located at the same azimuth plane. The “chord” distance between the source and the detector d is considered in a range from $0.5cm$ (assuring diffusion treatment) to $2R_0$, for optical properties set at $\mu_a = 0.01cm^{-1}$, $\mu'_s = 10cm^{-1}$, $A = 1$ and $S = 1$.

The geometries shown in Fig. 7 are chosen to study the effect of concave or convex shape on photon diffusion for the source and detector located longitudinally with the same azimuth angle. The optical properties are set the same as those used for Fig. 6.

Applying the solution in (5) leads to physically explicit interpretation in the two equations of (6) for a medium involving an external or internal cylindrical boundary. The

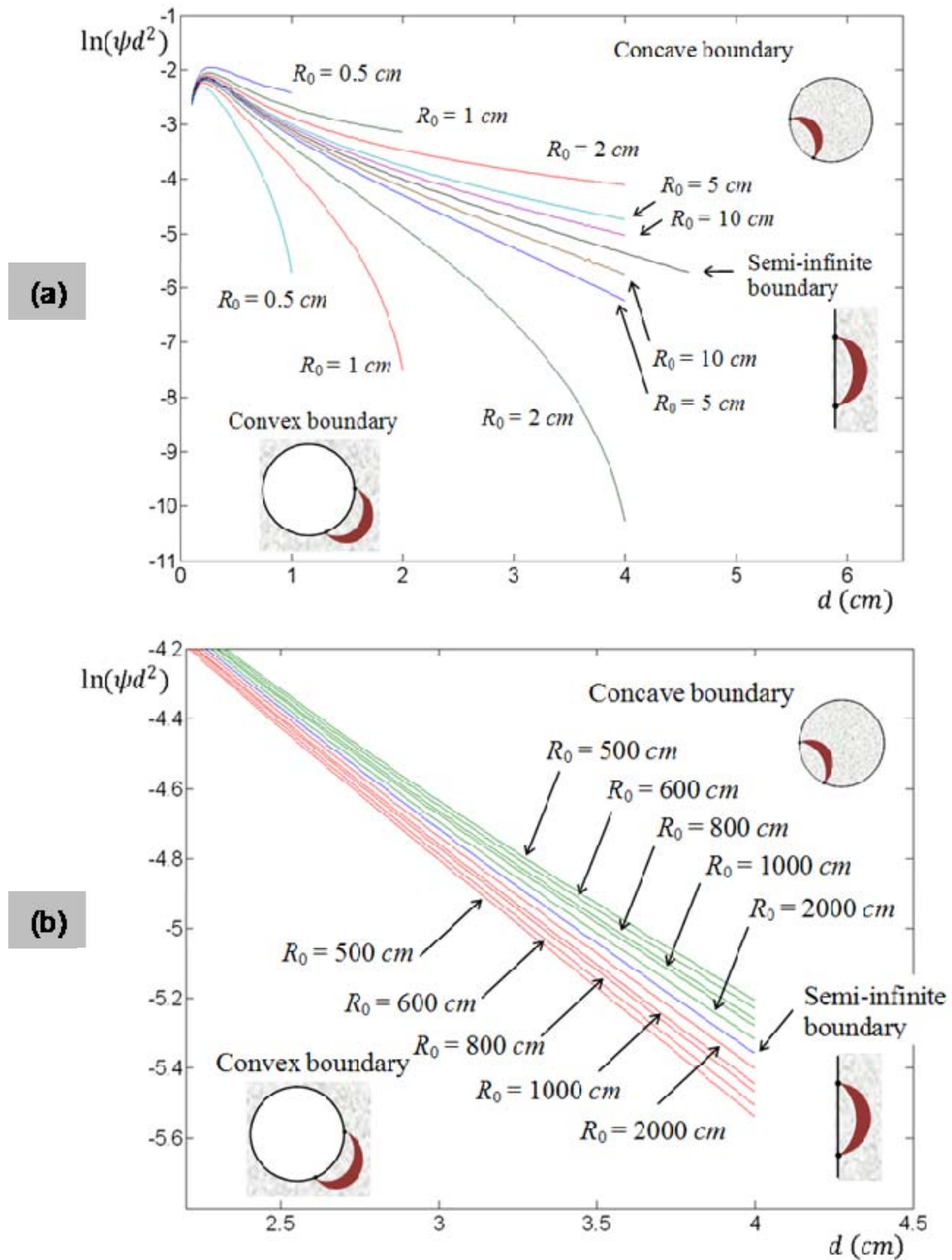


Figure 6. (a) Comparison of the solutions for concave and convex geometries with respect to the semi-infinite geometry, for source & detector located at the same azimuthal plane. (b) Comparison of the solutions for concave and convex geometries having large cylinder radius with respect to the semi-infinite geometry, for source & detector located at the same azimuthal plane.

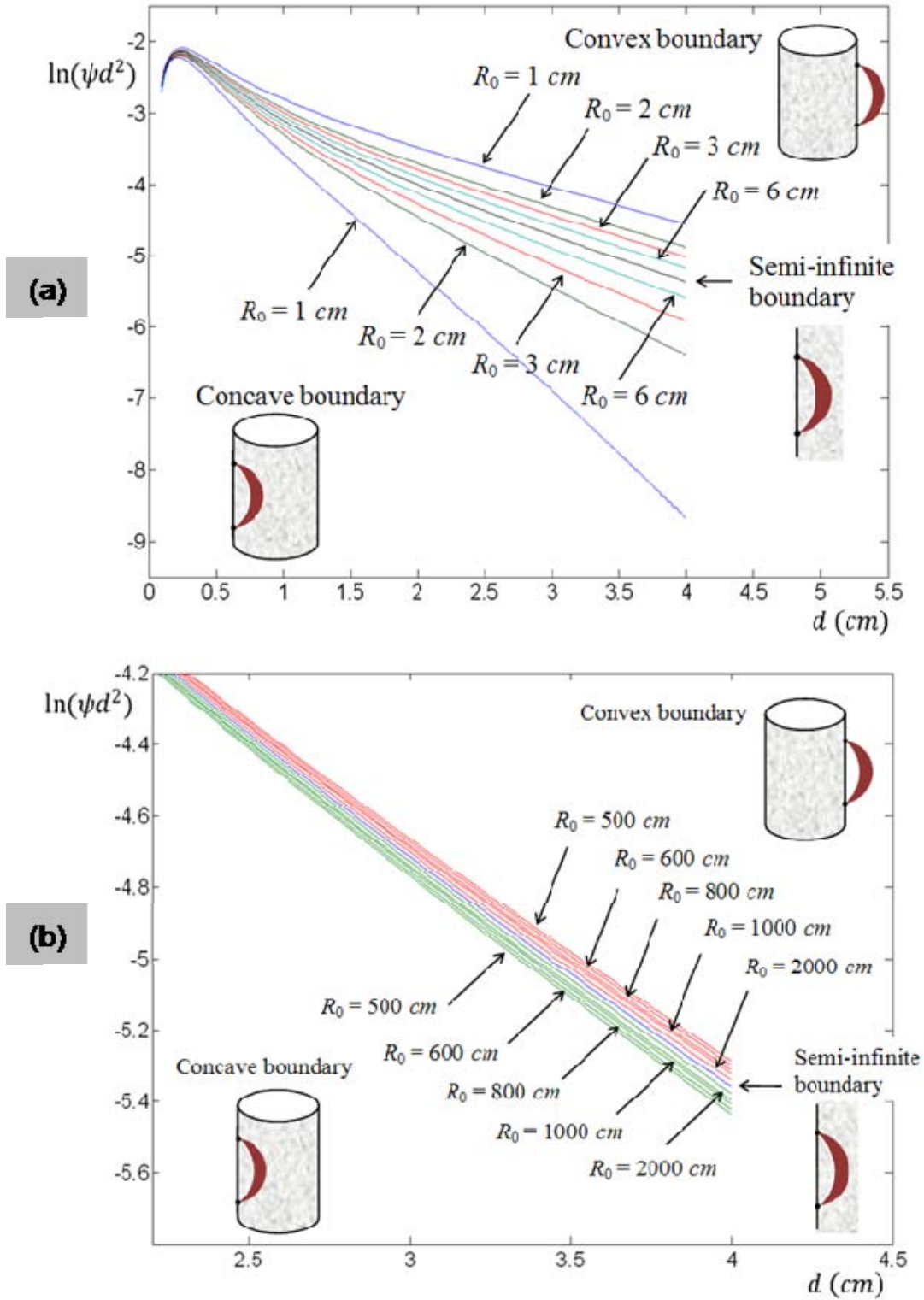


Figure 7. (a) Comparison of the solutions for concave and convex geometries with respect to the semi-infinite geometry, for source & detector located longitudinally with the same azimuthal angle. (b) Comparison of the solutions for concave and convex geometries having large cylinder diameter with respect to the semi-infinite geometry, for source & detector located longitudinally with the same azimuthal angle.

equations in (6) are composed of two parts in the brackets: the first part is associated with the “real” isotropic source, and the second part is the contribution of the “image” source term that is represented by the “real” source term scaled by a factor. The scaling factor is related to the radius of the cylinder and the reflective index mismatch of the cylinder-medium interface that determines where the extrapolated boundary shall be placed. The equations in (7), which are derived for large radius concave and convex boundaries, are given in a format similar to that for semi-infinite geometry but with a shape-curvature-associated term that approaches unity as the radius of the cylinder approaches infinity.

The numerical evaluations demonstrate the qualitative correctness of the analytic solutions in (6) for the two circular cylindrical geometries. It is clearly shown that the solutions given in (6) asymptotically approach the semi-infinite medium solution as the applicator radius reaches infinity. For the specific case of having the source and detector located azimuthally on the same axial plane, the photon fluence rate is greater than the semi-infinite geometry for the concave boundary and smaller for the convex boundary given the same source-detector distance. This can be interpreted by the fact that, for the same source-detector distance, more near-field photons from the source could scatter and reach the detector in the concave geometry than in the semi-infinite geometry, but in the convex geometry it does the opposite. For the specific case of having the source and detector located longitudinally on the same azimuthal angle, the photon fluence rate is smaller than the semi-infinite geometry for the concave boundary and greater for the convex boundary given the same source-detector distance. This again can be interpreted by the fact that, for the same source-detector distance, less near-field photons from the source could scatter and reach the detector in the concave geometry than in the semi-infinite geometry, but in the convex geometry it does the opposite.

KEY RESEARCH ACCOMPLISHMENTS

The following research accomplishments have been made during the 3rd year of this project:

1. A spectral trans-rectal NIR tomography system at dual-wavelength of 785nm and 830nm for coupling to TRUS probe is developed.
2. *In vivo* non-invasive light imaging of [HbT] changes associated with tumor development in the canine prostate is demonstrated. Using transrectal US-coupled spectral optical tomography the development and lateral involvement of the prostate cancer was detected earlier than using TRUS alone.
3. The optical properties of canine and human prostates reported in literature, which were all acquired by invasive or in vitro measurements, are comprehensively reviewed. There are noticeable intra-organ optical heterogeneities, which poses a substantial challenge to differentiating malignant tissue from normal tissue in real-time imaging condition. Our approach of trans-rectal near-infrared diffuse optical tomography, however, demonstrated that the prostate cancer can be differentiated from benign prostatic tissue by the intrinsic optical property contrasts.
4. A novel analytic treatment for photon diffusion in a homogenous medium bounded externally or internally by an infinitely long circular cylindrical applicator is presented. The geometry of a diffusive medium bounded externally by a cylindrical applicator resembles that of imaging externally-accessible biological tissue such as breast using a ring-type array. The geometry of a diffusive medium bounded internally by a cylindrical applicator resembles that of imaging internally-accessible biological tissue such as prostate using trans-rectal probe.

REPORTABLE OUTCOMES

The progress in the 3rd year of this project has results in following publications or manuscripts:

Journal Papers

1. Piao D, Jiang Z, Bartels KE, Holyoak GR, Ritchey JW, Xu G, Bunting CF, Slobodov G, “In vivo trans-rectal ultrasound-coupled near-infrared optical tomography of intact normal canine prostate,” *Journal of Innovative Optical Health Sciences*, Vol. 2, No. 3, pp. 215-225 (2009).
2. Jiang Z, Holyoak GR, Bartels KE, Ritchey JW, Xu G, Bunting CF, Slobodov G, Piao D, “In vivo trans-rectal ultrasound coupled near-infrared optical tomography of a transmissible venereal tumor model in the canine pelvic canal,” *Journal of Biomedical Optics Letters*, Vol. 14, No. 3, pp. 030506, (2009).
3. Zhang A, Piao D, Bunting CF, Pogue BW, “Photon diffusion in a homogeneous medium bounded externally or internally by an infinitely long circular cylindrical applicator ---- Part I: steady-state theory,” *Journal of Optical Society of America, A*, Vol. 27, No. 3, pp. 648-662 (2010).
4. Piao D, Bartels KE, Jiang Z, Holyoak GR, Ritchey JW, Xu G, Bunting CF, Slobodov G, “Alternative trans-rectal prostate imaging: A diffuse optical tomography method,” *IEEE Journal of Selected Topics in Quantum Electronics*, “Biophotonics 2” Special Issue, appear in July/Aug, 2010. (Invited paper).

Proceeding Papers and Conference Presentations

1. Piao D, Jiang Z, Bartels KE, Holyoak GR, Ritchey JW, Xu G, Bunting CF, Slobodov G, “In vivo optical absorption, reduced scattering, and effective attenuation tomography of intact normal and cancerous canine pelvic canal including the prostate,” *Saratov Fall Meetings (SFM) 09*, Saratov, Russia, 21–24 September 2009. (Internet invited lecture).
2. Zhang A, Piao D, Yao G, Pogue BW, “Photon diffusion associated with a cylindrical applicator boundary for axial trans-luminal optical tomography: experimental examination of the steady-state theory,” *OSA Biomedical Topical Meetings*, Miami, Apr. 11-14, 2010, accepted.
3. Jiang Y, Mukherjee S, Stine JE, Bunting CF, Piao D, “FPGA-assisted strategy toward efficient reconstruction (FAStER) in diffuse optical tomography,” *OSA Biomedical Topical Meetings*, Miami, Apr. 11-14, 2010, accepted.
4. Jiang Z, Bartels KE, Holyoak GR, Ritchey JW, Krasinski JS, Bunting CF, Slobodov G, Piao D, “Trans-rectal ultrasound-coupled spectral optical tomography at 785nm and 830nm detects elevation of total hemoglobin concentration in canine prostate associated with the development of transmissible venereal tumors,” *OSA Biomedical Topical Meetings*, Miami, Apr. 11-14, 2010, accepted.
5. Xu G, Piao D, Bunting CF, Dehghani H, “The pain and gain of DC-based diffuse optical tomography reconstruction---New insights into an old-look problem,” *OSA Biomedical Topical Meetings*, Miami, Apr. 11-14, 2010, accepted.

CONCLUSIONS

The research is to explore the technology of trans-rectal near-infrared (NIR) optical tomography that may benefit accurate, selective prostate biopsy. The research in the 3rd year has made important advancements. The advancements include the implementation of spectral trans-rectal NIR tomography for quantitation of hemoglobin concentration in prostate, the assessment of lateral involvement and longitudinal development of canine prostate TVT, the review of optical properties of canine and human prostates, and the establishment of a unified theory to account for the cylinder-applicator used in either external or internal imaging geometry. The future work will investigate if contrast of oxygen saturation can be imaged from canine TVT by transrectal optical tomography. Overall, the transrectal optical tomography has potential of improving the clinical diagnosis and biopsy of prostate cancer.

REFERENCES

5. Jiang Z, Holyoak GR, Bartels KE, Ritchey JW, Xu G, Bunting CF, Slobodov G, Piao D, "In vivo trans-rectal ultrasound coupled near-infrared optical tomography of a transmissible venereal tumor model in the canine pelvic canal," *Journal of Biomedical Optics Letters*, Vol. 14, No. 3, pp. 030506, May/June, 2009.
6. McCay CM, The hemoglobin and total phosphorus in the blood of cows and bulls, *J. Dairy Sci.* 1931; 14: 373-378.
7. Hayes MD, Vanzant ES, Stombaugh TS, Gates RS, Comparison of bovine blood absorption coefficients to human curves, *Livestock Environment VIII Proceedings*. 2008; 981-985.
8. Newman JS, Bree RL, Rubin JM, Prostate cancer: diagnosis with color Doppler sonography with histologic correlation of each biopsy site, *Radiology* 1995; 195: 86-90.
9. Bigler SA, Deering RE, Brawer MK, Comparison of microscopic vascularity in benign and malignant prostate tissue, *Hum Pathol.* 1993; 24: 220-6.
10. Cosgrove D, Angiogenesis imaging—ultrasound, *Br J Radiol.* 2003; 76: S43-49.
11. Halpern JE, Color and power Doppler evaluation of prostate cancer, in Halpern RJ, Cochlin DL, Goldberg BB (Ed), *Imaging of the Prostate*, Martin Dunitz, London, 2002, pp 39-50.
12. Tromberg BJ, Pogue BW, Paulsen KD, Yodh AG, Boas DA, Cerussi AE, Assessing the future of diffuse optical imaging technologies for breast cancer management, *Med Phys.* 2008; 35: 2443-51.
13. Zhu Q, Cronin EB, Currier AA, Vine HS, Huang M, Chen N, Xu C. Benign versus malignant breast masses: optical differentiation with US-guided optical imaging reconstruction, *Radiology* 2005; 237: 57-66.
14. Svensson T, Andersson-Engels S, Einarsson M, Svanberg K, In vivo optical characterization of human prostate tissue using near-infrared time-resolved spectroscopy, *J Biomed Opt.* 2007; 12: 014022-1-014022-10.
15. Xuan JW, Bygrave M, Jiang H, Valiyeva F, Dunmore-Buyze J, Holdsworth DW, Izawa JI, Bauman G, Moussa M, Winter SF, Greenberg NM, Chin JL, Drangova M, Fenster A, Lacefield JC, Functional neoangiogenesis imaging of genetically engineered mouse prostate cancer using three-dimensional power Doppler ultrasound, *Cancer Res.* 2007; 67: 2830-9.
16. Oraevsky AA, Jacques SL, Tittel FK., "Measurement of tissue optical properties by time-resolved detection of laser-induced transient stress." *Appl. Opt.*, **36**:402-15, 1997.
17. Chen Q, Wilson BC, Shetty SD, Patterson MS, Cerny JC, Hetzel FW., "Changes in in vivo optical properties and light distributions in normal canine prostate during photodynamic therapy." *Radiat. Res.*, **147**:86-91, 1997.
18. Lee LK, Whitehurst C, Chen Q, Pantelides ML, Hetzel FW, Moore JV., "Interstitial photodynamic therapy in the canine prostate." *Br. J. Urol.*, **80**:898-902, 1997.
19. Nau WH, Roselli RJ, Milam DF. "Measurement of thermal effects on the optical properties of prostate tissue at wavelengths of 1,064 and 633 nm." *Lasers Surg. Med.*, **24**:38-47, 1999.
20. Lilge L, Pomerleau-Dalcourt N, Douplik A, Selman SH, Keck RW, Szkudlarek M, Pestka M, Jankun J. "Transperineal in vivo fluence-rate dosimetry in the canine prostate during SnET2-mediated PDT." *Phys. Med. Biol.*, **49**:3209-25, 2004.
21. Jankun J, Lilge L, Douplik A, Keck RW, Pestka M, Szkudlarek M, Stevens PJ, Lee RJ, Selman SH. "Optical characteristics of the canine prostate at 665 nm sensitized with tin etiopurpurin dichloride: need for real-time monitoring of photodynamic therapy." *J. Urol.*, **172**:739-43, 2004.

22. Jankun J, Keck RW, Skrzypczak-Jankun E, Lilge L, Selman SH., "Diverse optical characteristic of the prostate and light delivery system: implications for computer modelling of prostatic photodynamic therapy." *B. J. U. Int.*, **95**:1237-44, 2005.
23. Solonenko M, Cheung R, Busch TM, Kachur A, Griffin GM, Vulcan T, Zhu TC, Wang HW, Hahn SM, Yodh AG. "In vivo reflectance measurement of optical properties, blood oxygenation and motexafin lutetium uptake in canine large bowels, kidneys and prostates." *Phys. Med. Biol.*, **47**:857-73, 2002.
24. Zhu TC, Hahn SM, Kapatkin AS, Dimofte A, Rodriguez CE, Vulcan TG, Glatstein E, Hsi RA, "In vivo optical properties of normal canine prostate at 732 nm using motexafin lutetium-mediated photodynamic therapy." *Photochem. Photobiol.*, **77**:81-8, 2003.
25. Piao D, Bartels KE, Jiang Z, Holyoak GR, Ritchey JW, Xu G, Bunting CF, Slobodov G, "Alternative trans-rectal prostate imaging: A diffuse optical tomography method," *IEEE Journal of Selected Topics in Quantum Electronics*, "Biophotonics 2" Special Issue, appear in July/Aug, 2010, (invited paper).
26. Pantelides ML, Whitehurst C, Moore JV, King TA, and Blacklock NJ, "Photodynamic therapy for localized prostatic cancer—light penetration in the human prostate-gland," *J. Urol. (Baltimore)* **143**(2), 398–401, 1990.
27. Wei HJ, Xing D, He BH, Wu RH, Gu HM, Wu GY, Chen XM, "Absorption and scattering characteristics of human benign prostatic hyperplasia tissue with Ti: sapphire laser irradiation in vitro," *Guang Pu Xue Yu Guang Pu Fen Xi.*; **28**(1):10-3, 2008. Chinese.
28. Essenpreis M, "Thermally induced changes in optical properties of biological tissues," Ph.D. Thesis, University College London, 1992.
29. Roggan A, Do'rschel K, Minet O, Wolff D, Mu' ller G, "The optical properties of biological tissue in the near infrared wavelength range—review and measurements," In: Mu' ller G, Roggan A, editors. *Laser-induced interstitial thermotherapy*. Washington: SPIE Optical Engineering Press; 1995. p 10–44.
30. Whitehurst C, Pantelides ML, Moore JV, Brooman PJC, and Blacklock NJ, "In vivo laser-light distribution in human prostatic carcinoma," *J. Urol. (Baltimore)* **151**(5), 1411–1415, 1994.
31. Lee LK, Whitehurst C, Pantelides ML, and Moore JV, "In situ comparison of 665 nm and 633 nm wavelength light penetration in the human prostate gland," *Photochem. Photobiol.* **62**(5), 882–886, 1995.
32. Lee LK, Whitehurst C, Pantelides ML, and Moore JV, "An interstitial light assembly for photodynamic therapy in prostatic carcinoma," *BJU Int.* **84**(7), 821–826, 1999.
33. Zhu TC, Dimofte A, Finlay JC, Stripp D, Busch T, Miles J, Whittington R, Malkowicz SB, Tochner Z, Glatstein E, Hahn SM., "Optical properties of human prostate at 732 nm measured in mediated photodynamic therapy," *Photochem Photobiol.*; **81**(1):96-105, 2005
34. Zhu TC, Finlay JC, and Hahn SM, "Determination of the distribution of light, optical properties, drug concentration, and tissue oxygenation in vivo in human prostate during motexafin lutetiummediated photodynamic therapy," *J. Photochem. Photobiol., B* **79**(3):231-41, 2005.
35. Weersink RA, Bogaards A, Gertner M, Davidson SRH, Zhang K, Natchev G, Trachtenberg J, and Wilson BC, "Techniques for delivery and monitoring of TOOKAD _WST09_-mediated photodynamic therapy of the prostate: clinical experience and practicalities," *J. Photochem. Photobiol., B* **79**(3), 211–222, 2005.

36. Svensson T, Alerstam E, Einarsdóttir M, Svanberg K, and Andersson-Engels S, "Towards accurate in vivo spectroscopy of the human prostate," *J. Biophotonics* **1**, 200-203, 2008.
37. Li J, Zhu TC, "Determination of in vivo light fluence distribution in a heterogeneous prostate during photodynamic therapy," *Phys Med Biol.* 2008 Apr 21;53(8):2103-14, 2008.
38. Wang KK, Zhu TC, "Reconstruction of in-vivo optical *properties* for human prostate using interstitial diffuse optical tomography," *Opt Express*, 17(14):11665-72, 2009.

APPENDICES

1. Reprints of journal papers, conference proceeding papers and abstracts.

IN VIVO TRANS-RECTAL ULTRASOUND-COUPLED NEAR-INFRARED OPTICAL TOMOGRAPHY OF INTACT NORMAL CANINE PROSTATE

DAQING PIAO^{*,†}, ZHEN JIANG[†], KENNETH E. BARTELS[‡],
G. REED HOLYOAK[‡], JERRY W. RITCHEY[§], GUAN XU[†],
CHARLES F. BUNTING[†] and GENNADY SLOBODOV[¶]

[†]*School of Electrical and Computer Engineering
Oklahoma State University, Stillwater, OK 74078 USA
daqing.piao@okstate.edu

[‡]*Department of Veterinary Clinical Sciences
Oklahoma State University, Stillwater, OK 74078 USA*

[§]*Department of Veterinary Pathobiology
Oklahoma State University, Stillwater, OK 74078 USA*

[¶]*Department of Urology, University of Oklahoma Health
Sciences Center, Oklahoma City, OK 73104 USA*

This is the first tomography-presentation of the optical properties of a normal canine prostate, *in vivo*, in its native intact environment in the pelvic canal. The imaging was performed by trans-rectal near-infrared (NIR) optical tomography in steady-state measurement at 840 nm on three sagittal planes across the right lobe, middle-line, and left lobe, respectively, of the prostate gland. The NIR imaging planes were position-correlated with concurrently applied trans-rectal ultrasound, albeit there was no spatial *prior* employed in the NIR tomography reconstruction. The reconstructed peak absorption coefficients of the prostate on the three planes were 0.014, 0.012, and 0.014 mm⁻¹. The peak reduced scattering coefficients were 5.28, 5.56, and 6.53 mm⁻¹. The peak effective attenuation coefficients were 0.45, 0.43, and 0.50 mm⁻¹. The absorption and effective attenuation coefficients were within the ranges predictable at 840 nm by literature values which clustered sparsely from 355 nm to 1064 nm, none of which were performed on a canine prostate with similar conditions. The effective attenuation coefficients of the gland were shown to be generally higher in the internal aspects than in the peripheral aspects, which is consistent with the previous findings that the urethral regions were statistically more attenuating than the capsular regions.

Keywords: Prostate; canine; optical property; optical tomography; trans-rectal ultrasound.

1. Introduction

The knowledge of tissue optical properties relevant to light diffusion or attenuation is important to both the dosimetry of photodynamic therapy (PDT)^{1–4} and the analysis based on near-infrared (NIR) diffuse optical imaging.^{5–10} The prostate of

the dog is usually considered as a model closest to that of the human being, therefore a number of studies have been conducted^{11–20} on canine subjects to estimate the optical properties of prostate, *in vitro* or *in vivo*, over a wide range of spectrum (to be reviewed in more detail in Sec. 2 of this

study). A general consensus that has been made from these studies is that significant intra-organ and inter-subject variations of the prostate optical properties do occur. The optical properties being investigated include the absorption coefficient, the reduced or transport scattering coefficient, and the effective attenuation coefficient that is a combination of the above two properties. The reported intra-organ and inter-subject prostate optical heterogeneity imposes the need of individualized and localized measurement for PDT applications,¹⁸ as well as challenges to trans-rectal NIR tomography that aims to resolve the optical contrast, either endogenous^{21,22} or exogenous,²³ of prostate cancerous lesions over normal or benign prostate tissues.

It is also important in PDT to know the optical properties of peri-prostatic tissues, such as rectal or peri-rectal regions since the existence of any optical property gradient of the prostate over its peripheral tissue will influence the local peri-prostatic light distribution. For trans-rectal NIR tomography of the prostate, the NIR light is attenuated first by a condom (required for endo-rectal application), then by the rectal wall and the peri-rectal tissue before finally reaching the prostate. The degree of NIR light propagation into the prostate is dependent upon the optical property gradients between the prostatic capsule and peri-prostatic tissue. The *in vivo* or *in vitro* optical contrast of the prostate with respect to peri-rectal or peri-prostatic tissue is therefore fundamental to PDT and prostate NIR tomography, yet to our knowledge it has rarely been evaluated on a single subject. Overall there is very limited information regarding the NIR attenuating features of peri-rectal tissue.¹¹ Therefore, it is difficult to draw a comparison of the optical properties reported in different studies between the prostate and the peri-rectal tissue. Except the current reported *in vivo* investigation, all of the studies on normal prostate (canine and human) have been taken interstitially on exposed prostate or through trans-perineal imaging. The interstitial measurements, although very reliable and consistent, are likely to alter to some extent the optical properties natural to the tissue being measured.

In this work we present tomographic measurements of optical properties of a normal canine prostate, *in vivo*, in its native intact environment in the pelvic canal. The imaging was performed by trans-rectal NIR optical tomography in steady-state measurement at 840 nm, on

three sagittal planes across the right lobe, middle-line, and left lobe, respectively, of the prostate gland. The NIR imaging planes were position-correlated with concurrently applied trans-rectal ultrasound, albeit there was no spatial *prior* employed in the NIR tomography reconstruction. The prostate gland appears as a positive-contrast region in NIR images, particularly in the absorption and effective-attenuation images. The position and profile of the positive-contrast prostate-indicating region correlate well with those of the prostate in the concurrent trans-rectal ultrasound image. The peak absorption coefficients of the prostate-region on the three planes were found to be 0.014, 0.012, and 0.014 mm⁻¹. The peak reduced scattering coefficients were 5.28, 5.56, and 6.53 mm⁻¹. The peak effective attenuation coefficients were 0.45, 0.43, and 0.50 mm⁻¹. The absorption and effective attenuation coefficients were within the ranges that are predictable at 840 nm based on literature values which clustered sparsely from 355 nm to 1064 nm, none of which were performed on a prostate in similar conditions. It is also noted that effective attenuation coefficients of the gland are higher in the internal aspect than in the peripheral aspect, which is consistent with the previous findings of statistically more attenuating urethral regions than the capsular regions.



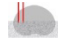





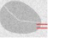
2. Review of the Optical Property Measurements on Canine Prostate

Tables 1 and 2 summarize what the authors have found to be existing methods, represented graphically by diagram (Table 1), and published values (Table 2) on optical properties of the canine prostate within the spectral range from 355 nm to 1064 nm. In Table 2, the attenuation coefficient is denoted by μ_a , the reduced scattering coefficient by μ'_s , and the effective attenuation coefficient by μ_{eff} that is defined as

$$\mu_{\text{eff}} = \sqrt{3\mu_a(\mu_a + \mu'_s)}. \quad (1)$$

Oraevsky *et al.* presented *in vitro* μ_a , μ'_s , and μ_{eff} of prostate at 355, 532, and 1064 nm, respectively, using opto-acoustic time-resolved fluence rate measurements on slab samples of normal canine prostate tissues.¹² Another post-mortem study by Chen *et al.* estimated prostate μ_a , μ'_s , and μ_{eff} at 630 nm, by interstitial measurements on excised

Table 1. Legend indicating the measurement methods used in Table 2.

								
Opto-acoustic on slab tissue	Integrating sphere on slab tissue	Interstitial on exposed prostate	Interstitial on excised prostate	Reflective on exposed prostate	Interstitial close to the capsule	Interstitial close to the urethra	Interstitial close to the base	Interstitial close to the apex

normal prostate.¹³ *In vitro* μ_a and μ'_s of slab samples of normal canine prostate tissues were evaluated at 633 nm, by employing steady-state fluence rate measurements using the standard double-integrating sphere technique.¹⁵ Other studies relied on steady-state fluence rate measurements on tissues *in situ*, albeit involving surgical procedures to expose the prostatic tissue to the fiber, to determine μ_{eff} of the normal canine prostate. At wavelengths of 630, 665, 730, 732 nm, interstitial measurements on normal canine prostate *in vivo* were conducted before and after PDT.^{14,17,18,20} Perhaps the only *in vivo* study using reflection measurement upon exposed prostate, thereby maintaining the intactness of the gland itself, was performed at 732 nm on exposed normal canine prostate.¹⁹ Trans-perineal interstitial measurement,^{16–18} which in principle is more accurate than interstitial measurement on exposed prostate, demonstrated with statistical significance that the μ_{eff} of prostatic urethral regions is higher than that of the prostatic capsular regions.^{16,17}

In Table 2, there are some individual values of μ_a and μ'_s , but nevertheless most original values listed are regarding μ_{eff} only, which are readily available from steady-state fluence rate measurements. Because the data are clustered in a wide spectrum, summarizing all these studies to a single category for spectrally-resolved comparative evaluation can only be made by utilizing μ_{eff} since it represents the coupled effect of μ_a and μ'_s . When the standard deviations of μ_a and μ'_s , denoted by $\sigma\mu_a$ and $\sigma\mu'_s$, respectively, are available, the standard deviation of μ_{eff} in Table 2 is calculated based on Eq. (1) by

$$\sigma\mu_{\text{eff}} = \sqrt{\left(\frac{\partial\mu_{\text{eff}}}{\partial\mu_a}\sigma\mu_a\right)^2 + \left(\frac{\partial\mu_{\text{eff}}}{\partial\mu'_s}\sigma\mu'_s\right)^2}. \quad (2)$$

3. Methods and Materials























3.1. Trans-rectal US-coupled NIR tomography

The details of the trans-rectal US-coupled NIR tomography system can be found elsewhere.^{21,22}

Figure 1 illustrates the configuration of the trans-rectal NIR/US probe and the prostate imaging geometry. Since NIR imaging depth is typically $1/2$ of the array dimension, the NIR optodes are distributed longitudinally in parallel to the sagittal US to allow interrogating deep prostatic tissues. The NIR arrays are also put symmetrically on the lateral sides of the sagittal US transducer, enabling accurate correlation of the middle-sagittal NIR imaging plane with the sagittal US imaging.

The completed trans-rectal NIR/US probe and imager are shown in Fig. 2. The US probe was a bi-plane sector and linear array trans-rectal probe fitted to an ALOKA SSD-900V unit. The NIR applicator was integrated over the 7.5 MHz sagittal-imaging transducer. The NIR probe consisted of one source and one detector array separated 20 mm laterally and placed symmetrically to the sagittal US transducer. The NIR source and detector array, each having seven channels, were 60 mm in longitudinal dimension, which was identical to the longitudinal length of the sagittal US transducer. Each NIR optode channel had a micro prism-lens pair for coupling the light to and from the probe surface. The NIR light from a super-luminescent diode of 100 mW at 840 nm was focused sequentially onto seven source fibers of the NIR applicator by a home-made translating fiber multiplexer. The NIR remissions collected by the seven detection fibers were acquired by a 16-bit intensified CCD camera through a spectrometer (not necessary for acquiring the data but used for system integrity). Acquisition of NIR signals from seven source channels took less than five seconds after the prostate was localized by the sagittal US using an Aloka SSD-900V portable US scanner, which provides 50 mm longitudinal field of view when performing sagittal imaging with the 60 mm long 7.5 MHz US transducer. The absorption and reduced scattering coefficients of the prostate were reconstructed from steady-state measurements²² using a model-based non-linear optimization method.^{22,25,26} The effective attenuation coefficient is then calculated based on Eq. (1).

Table 2. Optical properties of normal canine prostate tissue as reported in various published studies. N is the number of samples. This table follows the template for human prostate in Ref. 24.

Study [Ref.]	Year	Sample	N	Method	λ (nm)	μ_a (mm ⁻¹)	μ'_s (mm ⁻¹)	μ_{eff} (mm ⁻¹)
Oraevsky <i>et al.</i> [12]	1997	<i>In vitro</i>	2		355	0.852	5.22	3.94
Oraevsky <i>et al.</i> [12]	1997	<i>In vitro</i>	2		532	0.233	2.45	1.37
Chen <i>et al.</i> [13]	1997	<i>In vivo</i>	17		630	0.04 ± 0.02	2.6 ± 2.1	0.5 ± 0.1
Chen <i>et al.</i> [13]	1997	<i>Ex vivo</i>	10		630	0.030 ± 0.007	2.6 ± 0.8	0.48 ± 0.09
Lee <i>et al.</i> [14]	1997	<i>In vivo</i>	7		630			0.47 ± 0.05
Nau <i>et al.</i> [15]	1999	<i>In vitro</i> (fresh)	10		633	0.073 ± 0.007	0.225 ± 0.005	$0.256 \pm 0.015^*$
Nau <i>et al.</i> [15]	1999	<i>In vitro</i> (frozen)	13		633	0.076 ± 0.003	1.00 ± 0.11	$0.495 \pm 0.027^*$
Lilge <i>et al.</i> [16] [^]	2004	<i>In vivo</i>	7	 Capsule	660	0.0030 ± 0.0021	0.92 ± 0.65	$0.184 \pm 0.040^{\wedge}$
Lilge <i>et al.</i> [16] [^]	2004	<i>In vivo</i>	7	 Urethra	660	0.0014 ± 0.0013	3.23 ± 2.76	$0.206 \pm 0.035^{\wedge}$
Jankun <i>et al.</i> [17]	2004	<i>In vivo</i>	13	 Capsule	665			0.171 ± 0.071
Jankun <i>et al.</i> [17]	2004	<i>In vivo</i>	13	 Urethra	665			0.192 ± 0.027
Jankun <i>et al.</i> [17]	2004	<i>In vivo</i>	13	 Capsular base	665			0.259 ± 0.193
Jankun <i>et al.</i> [17]	2004	<i>In vivo</i>	13	 Urethral base	665			0.275 ± 0.131
Jankun <i>et al.</i> [17] [~]	2004	<i>In vivo</i>	13	 Capsular apex	665			$0.176 \pm 0.031^{\wedge\wedge}$
Jankun <i>et al.</i> [17]	2004	<i>In vivo</i>	13	 Urethral apex	665			0.190 ± 0.065
Jankun <i>et al.</i> [18]	2005	<i>In vivo</i>	5	 Base	665			0.247 ± 0.06
Jankun <i>et al.</i> [18]	2005	<i>In vivo</i>	5	 Apex	665			0.203 ± 0.026
Solonenko <i>et al.</i> [19]	2002	<i>In vivo</i>	4		730		1.27 ± 0.06	
Zhu <i>et al.</i> [20]	2003	<i>In vivo</i>	12		732	0.003–0.058	0.1–2.0	0.03–0.49
Nau <i>et al.</i> [15]	1999	<i>In vitro</i> (fresh)	7		1064	0.027 ± 0.003	1.76 ± 0.13	$0.381 \pm 0.026^*$
Nau <i>et al.</i> [15]	1999	<i>In vitro</i> (frozen)	10		1064	0.071 ± 0.006	0.79 ± 0.05	$0.428 \pm 0.023^*$
Oraevsky <i>et al.</i> [12]	1997	<i>In vitro</i>	2		1064	0.009	0.63	0.13

Note: *Calculation of the effective attenuation coefficient based on Eqs. (1) and (2).

[^]The values in the abstract of Ref. 16 are contrary to those in the text of Ref. 16. The results in the text were used here.

^{^^}The results given in Ref. 17 were “ $0.176 \pm 0.314 \text{ mm}^{-1}$,” which had the standard deviation larger than the mean value. The authors made a “reasonable” estimation of “ $0.176 \pm 0.0314 \text{ mm}^{-1}$ ” for this set of literature data.

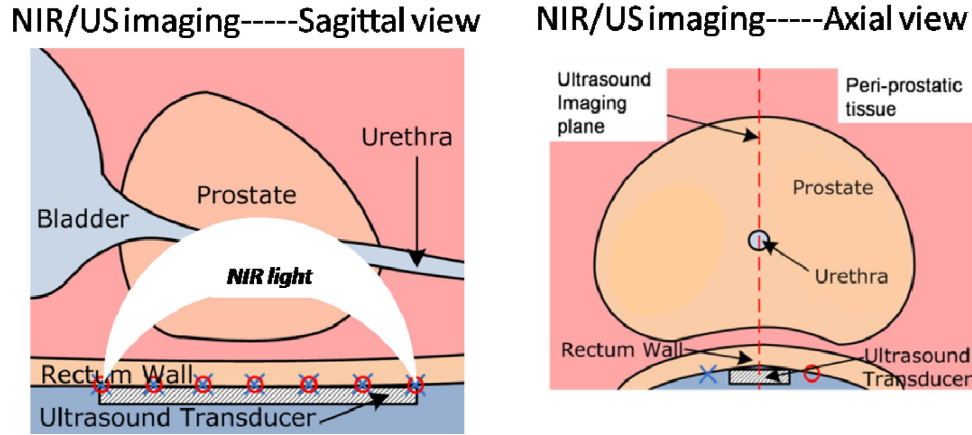


Fig. 1. Illustration of trans-rectal NIR/US of the prostate. Trans-rectal US is placed in the middle of the trans-rectal NIR applicator (optodes distributed longitudinally) to perform combined and correlated NIR/US imaging of the prostate at the sagittal plane.

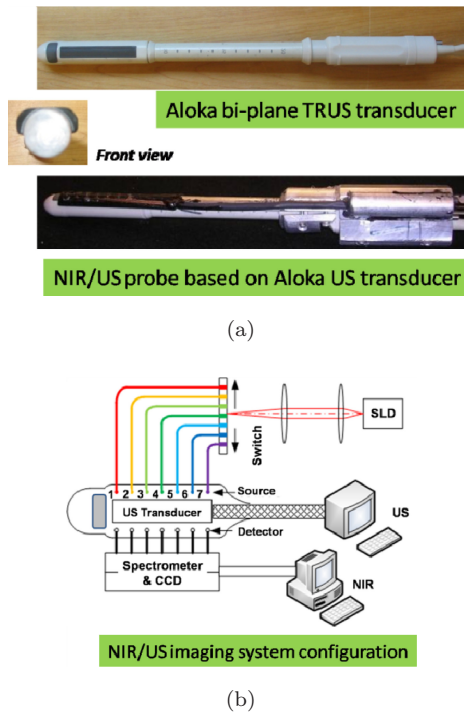


Fig. 2. (a) Photograph of the trans-rectal Aloka US transducer and the completed NIR/US probe. (b) Schematic diagram of the trans-rectal NIR/US imaging system that consists of a custom-built NIR imager and a commercial ALOKA SSD-900V portable US scanner.

3.2. Sensitivity features of the trans-rectal NIR imaging

Since the purpose of this study was to examine the inherent NIR contrast that the prostate may demonstrate over the peri-prostatic tissue, the NIR image was reconstructed without any spatial *prior* information. The accuracy or the robustness of the

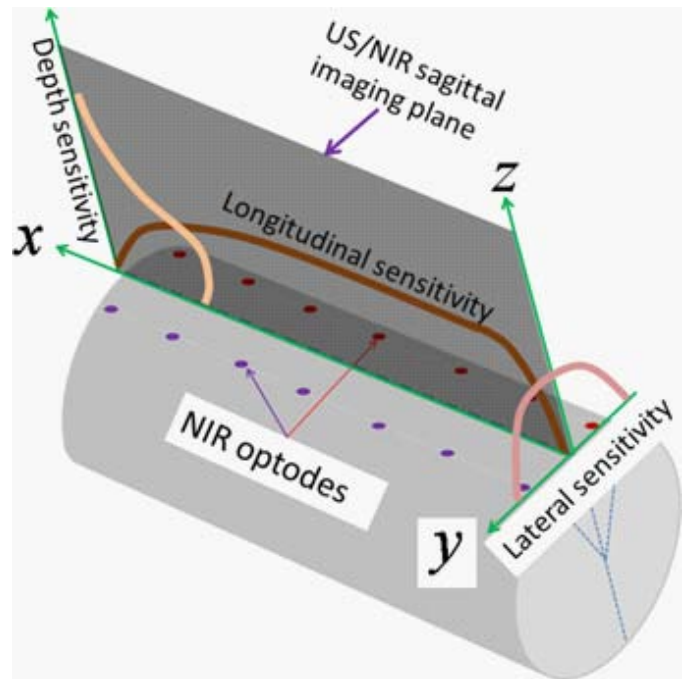


Fig. 3. Sensitivity profiles of the NIR imaging probe along the lateral, longitudinal and depth directions.

NIR reconstruction is thereby dependent upon the sensitivity of NIR array to the heterogeneity of the optical properties within the volume being interrogated. Figure 3 illustrate the sensitivity profiles, with respect to the absorption, of the NIR applicator based on the previous study.²¹ The longitudinal sensitivity is relatively uniform over the entire NIR array dimension, but it tapers off at the distal and proximal edges of the NIR array. The lateral sensitivity peaks at the middle-sagittal plane that coincides with the sagittal TRUS plane, while the

depth sensitivity generally degrades along with the increase of the depth. The sensitivity to the scattering or total attenuation would have similar patterns. Based on these sensitivity features, one could expect that a target may be reconstructed with better contrast if it is located within the regions of higher NIR sensitivity. It is also anticipated that for multiple targets located longitudinally on the same sagittal plane, the contrast-comparison would be reliable.

3.3. Animal model

This study was approved by the Institutional Animal Care and Use Committee of Oklahoma State University. The protocol was also approved and underwent an on-site inspection by the US Army Medical Research and Materiel Command. A 20-kg sexually intact, adult mixed-breed dog, approximately four years of age, was anesthetized using an intravenous injection of propofol (8 mg/kg) followed by intubation and halothane/oxygen inhalation for anesthetic maintenance. The animal was placed in left lateral recumbency for bowel preparation and physical examination (rectal palpation) of the prostate. TRUS visualization was performed using the combined trans-rectal NIR/US probe with condom-and-gel coverage. Both the physical examination and ultrasound revealed a normal prostate for this dog. The prostate was examined weekly using similar procedures, with consistent evaluation results being classified as “normal,” until the dog was euthanized nine weeks after the initial exam with an overdose of pentobarbital sodium. A complete necropsy was performed and the prostate and peri-prostatic structures were submitted for histologic examination.

4. Results

Figure 4 displays one set of sagittal trans-rectal NIR tomography images and the correlated TRUS performed at the right lobe, middle-line, and the left lobe of the normal canine prostate gland. The dimensions of the NIR and correlated TRUS images are 50 mm (cranial-to-caudal) \times 30 mm (dorsal-to-ventral). Each of the images represents one of three highly consistent measurements taken at each location.

The NIR absorption coefficient images are displayed at a color-scale of [0.007 0.014] mm^{-1} . The NIR transport scattering coefficient images are displayed at a color-scale of [3.000 6.000] mm^{-1} . The

NIR effective attenuation coefficient images are displayed at a color-scale of [0.250 0.500] mm^{-1} . The color-scales in all images represent a background threshold at $1/2$ of the maximum value of the color-scale. At this scale, the locations of the NIR regions indicating the prostate had excellent position correlation with prostatic images obtained using TRUS. The urinary bladder is shown as an anechoic structure on TRUS, which is similar to images using NIR. Most of the peri-rectal tissues are also not identified using NIR except at the periphery of the urinary bladder. The prostate is consistently demonstrated in NIR images as having positive-contrast with respect to the peri-prostatic tissues, with an average of more than two-folds of contrast in absorption, reduced scattering, and effective attenuation. In addition, the prostate is more optically heterogeneous in the middle-line and more optically attenuating toward the internal aspects of the prostate than in the peripheral aspects of the gland.

At this scale setting, it is noted that areas of prostatic regions on NIR images resemble the actual cross-sections being interrogated on the gland. The cranial-caudal length dimensions of the prostate at the right lobe and left lobe NIR images are smaller than that at the middle-line NIR images. The dorsal-ventral thickness dimensions of the prostate in the right and left lobe NIR images are shown greater than that at the middle-line NIR images. Overall, the prostate is longitudinally elongated in the middle line than in the right and left lobes. This profile of the canine prostate interpreted from NIR regions implies a walnut-shape with lobular anatomy.

Figure 4 illustrates peak absorption coefficients of this prostate specimen on the three planes to be 0.014, 0.012, and 0.014 mm^{-1} ; the peak reduced scattering coefficients to be 5.28, 5.56, and 6.53 mm^{-1} ; and the peak effective attenuation coefficients to be 0.45, 0.43, and 0.50 mm^{-1} . The validity of these numbers has been examined in the context of values summarized in Table 2 and by the spectra plots in Fig. 5. The majority of the previous measurements in Table 2 were performed in the spectral range of 630 nm to 732 nm, with some extension to the ultraviolet end of 355 nm and the infrared end of 1064 nm. The data points of this study, performed at 840 nm, represent the values of absorption, reduced scattering, and effective attenuation averaged over the peak values of right lobe, middle line, and left lobe. It is noted that the absorption coefficients of this study are

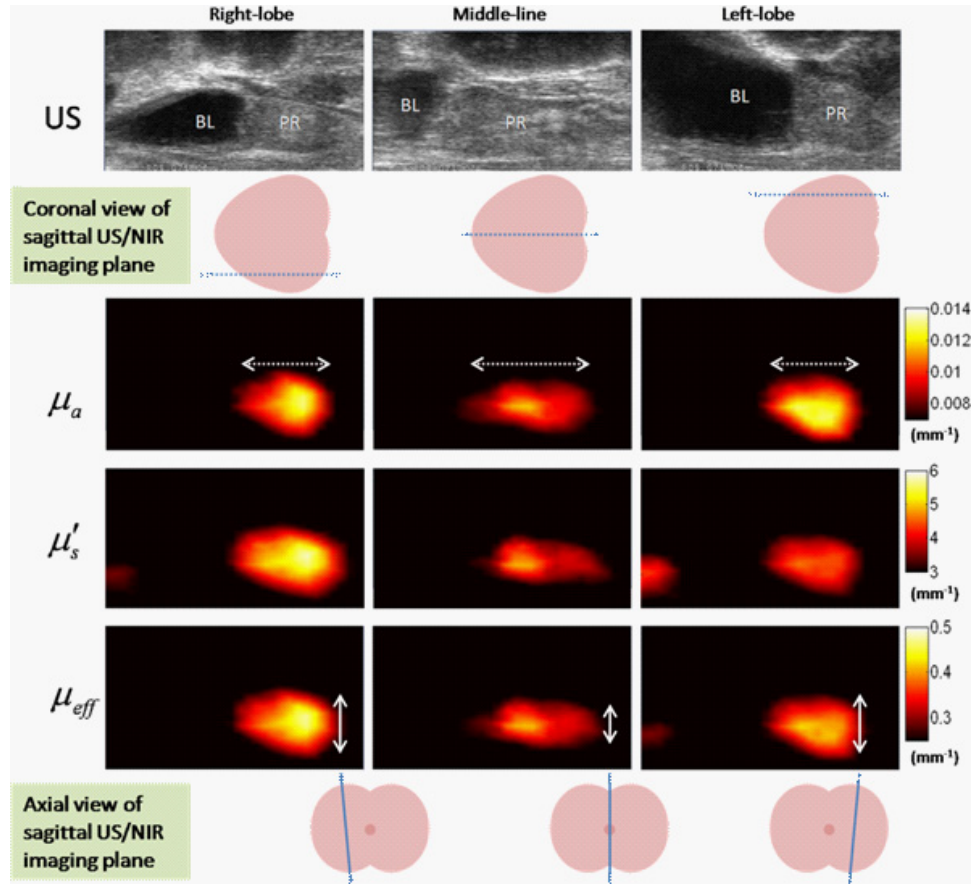


Fig. 4. Trans-rectal NIR/US of normal canine prostate *in vivo*: The US and NIR images were taken at the right lobe (left column), middle-line (middle column), and the left lobe (right column). The 1st row, US; the 2nd row, coronal view of the locations of sagittal NIR/US planes; the 3rd row, absorption coefficient; the 4th row, transport scattering coefficient; the 5th row, effective attenuation coefficient; the 6th row, axial view of the locations of sagittal NIR/US planes. The dimensions of all images are 50 mm × 30 mm (cranial-caudal × dorsal-ventral). BL-urinary bladder, PR-prostate.

narrowly distributed in a range predicted by the reported values closest to 840 nm. The reduced scattering values of this study are much higher (2–3 folds) than what may be estimated from the previously reported values, yet the effective attenuation coefficients of this study are narrowly distributed within the range predictable by reported values.

5. Gross and Histological Examination of the Prostate Gland

The prostate gland exhibited diffuse, symmetrical (and mild) enlargement (4.5 cm × 4.5 cm × 2.5 cm). On cross-section, the tissue was grossly normal with the exception of a discrete, 0.5 cm in diameter focus of grey/tan tissue [arrowhead, Fig. 6(b)] located in the region of the right prostatic lobe. Histologically, this focus corresponded to moderate interstitial

fibrosis with infiltration by primarily lymphocytic inflammatory cells [arrow, Fig. 6(d)]. The remainder of the prostatic tissue exhibited diffuse slight enlargement of the prostatic epithelium with occasional papillary projections and cystic dilation of prostatic glands consistent with early benign prostatic hyperplasia/hypertrophy. Otherwise, the tissue was histologically unremarkable [Fig. 6(c)]. The histological results confirmed that the NIR optical contrasts presented in this work are of a normal canine prostate.

6. Discussions

This study revealed the *in vivo* optical properties of an intact normal canine prostate in its normal anatomic position in the pelvic canal. The absorption, reduced scattering and effective attenuation coefficients of the canine prostate at approximately 840 nm have not been reported previously. However,

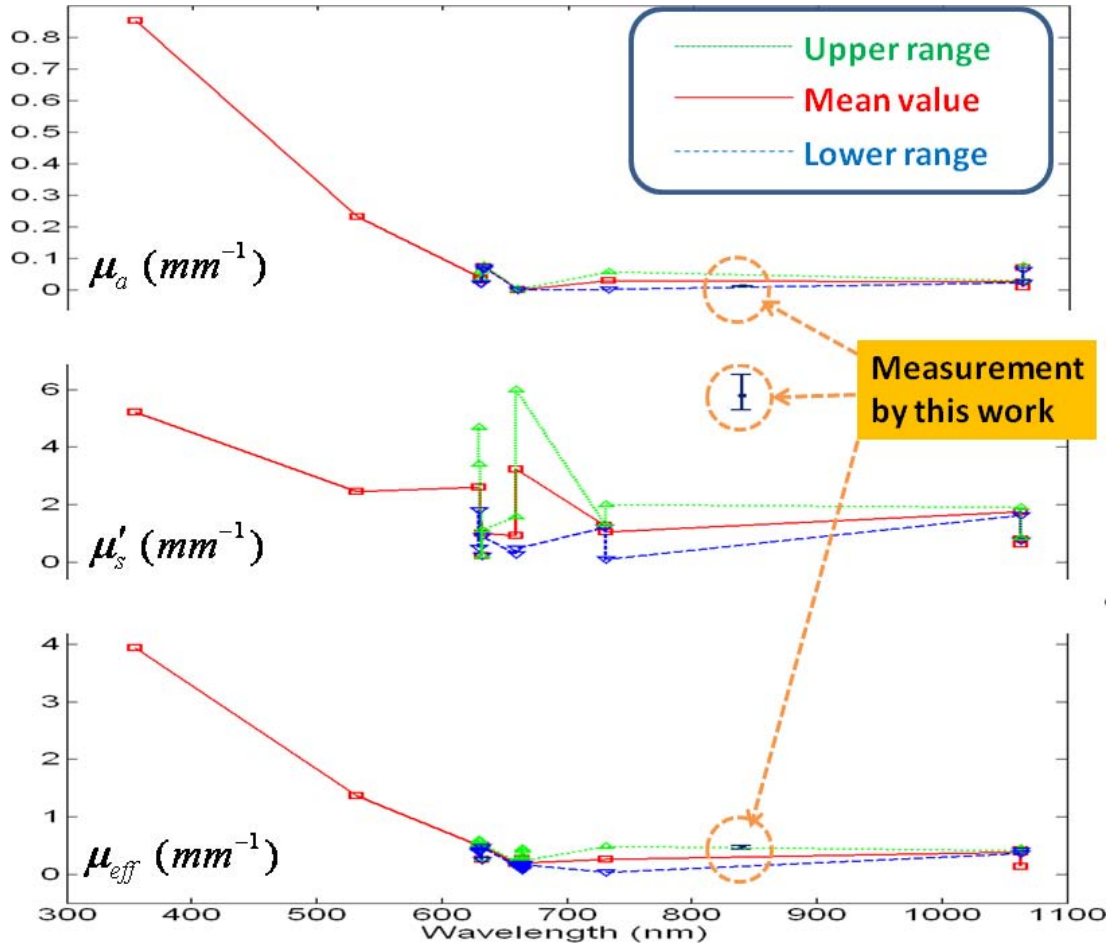


Fig. 5. Spectra of the optical properties of canine prostate based on the values given in Table 2. The measurements by this work at 840 nm were the average of the peak values of the right lobe, middle line, and left lobe.

an examination of the spectra in Fig. 5 allowed estimation of these values to be around that value. Given that the prostate is a gland with relatively rich vasculature, it is not difficult to correlate the absorption spectrum of the prostate to that of the total hemoglobin content, which has a low NIR absorption at and above the near-infrared band, as well as a relatively leveled absorption at wavelengths greater than the isosbestic point of 805 nm. The reduced scattering spectrum is rather “noisy” in the NIR band, yet globally it seems to follow the empirical power-law model of $\mu'_s = A\lambda^{-b}$, where A and b are model parameters for scattering amplitude and scattering power, respectively,²⁷ when there is a broad range of scattering particle sizes. The effective attenuation spectrum is close to that of the absorption, a result that may be anticipated from Eq. (1). Among the three optical properties being measured or calculated, both the absorption and effective attenuation coefficients are well within what can be predicted from the current literature.

The predicted average reduced scattering values at 840 nm from the literature may be much smaller than the measured values in this study but there is a fairly large error of distribution within the cited values of the spectra. It is thereby impractical to predict the reduced scattering coefficient at 840 nm within a narrow range based on the literature spectra. On the other hand, this study utilized non-*prior* guided pure optical-based reconstruction for trans-rectal optical tomography. Our previous study indicated that when an accurate spatial *prior* to trans-rectal NIR tomography reconstruction is not employed, the absorption coefficients may be under-estimated, and the reduced scattering coefficients may be over-estimated.²¹ The image reconstruction of trans-rectal NIR tomography in this study requires a 3D mesh being used due to the geometry of the NIR applicator. Extracting an accurate 3D prostate profile based on sagittal TRUS images, however, remains a challenging task. If the optical properties were reconstructed with an accu-

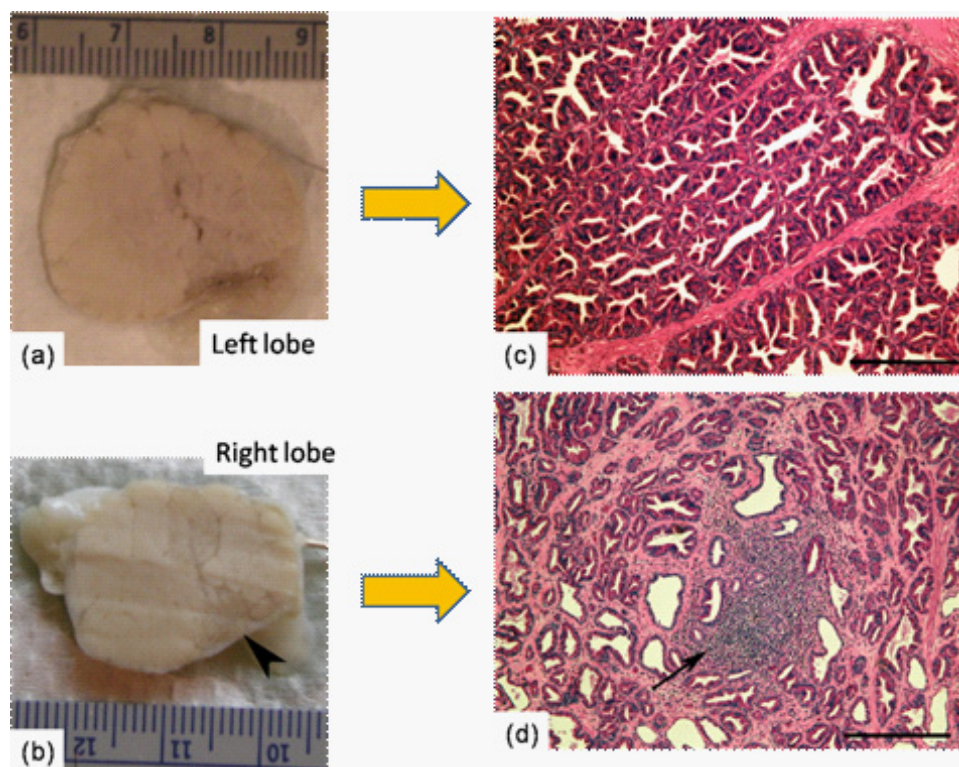


Fig. 6. Canine prostate gland. The prostate gland was slightly enlarged ($4.5\text{ cm} \times 4.5\text{ cm} \times 2.5\text{ cm}$) and on cross-section was predominantly unremarkable (a). The right lobe of the prostate contained a 0.5-cm in diameter focus of grey/tan tissue [arrowhead in (b)]. Histologically, most of the prostate gland exhibited inconspicuous lesions of early prostatic hyperplasia/hypertrophy consisting of increased prostatic epithelial cell size (c), scattered papillary projections and cystic dilation of prostatic acini. The gross lesion in the right prostatic lobe consisted of a focus of interstitial fibrosis and lymphocytic prostatitis [arrow in (d)]. Hematoxylin and Eosin stain, Bar = $360\text{ }\mu\text{m}$.

rate spatial *prior*, the reduced scattering coefficients could have better correlation with the literature predictions.

This study also revealed the optical property contrasts that a normal canine prostate has over other structures within the canine pelvic canal. The prostate is shown as having positive-contrast over its peripheral tissue in absorption, reduced scattering, and effective attenuation of the NIR light. There are a number of factors that could make the prostate hyper-attenuating on trans-rectal NIR tomography. First, the unique thin-layers of prostatic capsule may be refractive-index mismatched with respect to the peri-prostatic tissue, thereby causing specular reflection on the prostatic capsule that contributes to the elevated light attenuation of the prostate. Second, the prostate is known to have relatively rich vasculature that may impose stronger NIR absorption within the prostate. Third, the intra-prostatic parenchyma is known to be optically heterogeneous,^{12–20} a condition favorable to high scattering attenuation. The origin of the

intra-prostatic optical heterogeneity is not well understood, but is likely due to multiple factors. These factors may include (1) the radially-distributed blood vessels giving non-uniform blood vessel count throughout the prostate, (2) the unique intra-prostatic anatomy that is complicated by the existence of urethra and ejaculation ducts, and (3) the different cellular structures in the different zonal areas of the prostate. Among these factors, the first and second may also cause the higher effective attenuation in the urethral region than in the capsular region that is clearly demonstrated in Refs. 15 and 16.

7. Conclusions

In conclusion, the optical properties of a normal canine prostate, *in vivo*, in its native intact environment in pelvic canal have been acquired for the first time by trans-rectal NIR optical tomography at 840 nm, under TRUS position-correlation but with

no spatial *prior* employed in the reconstruction. The absorption and effective attenuation coefficients are within the ranges predictable at 840 nm by literature values which clustered sparsely from 355 nm to 1064 nm. The effective attenuation coefficients are found higher in the internal aspects of the prostate than in the peripheral aspects, which agrees with the previous findings that the urethral regions were statistically more attenuating than the capsular regions.

Acknowledgment

This work has been supported by the Prostate Cancer Research Program of the US Army Medical Research Acquisition Activity (USAMRAA), 820 Chandler Street, Fort Detrick, MD, 21702-5014, through a Grant #W81XWH-07-1-0247.

References

1. Q. Chen, Z. Huang, D. Luck, J. Beckers, P. H. Brun, B. C. Wilson, A. Scherz, Y. Salomon, F. W. Hetzel, "Preclinical studies in normal canine prostate of a novel palladium-bacteriopheophorbide (WST09) photosensitizer for photodynamic therapy of prostate cancers," *Photochem. Photobiol.* **76**, 438–445 (2002).
2. K. K. Wang, L. Lutzke, L. Borkenhagen, W. Westra, M. W. Song, G. Prasad, N. S. Buttar, "Photodynamic therapy for Barrett's esophagus: Does light still have a role?" *Endoscopy* **40**, 1021–1025 (2008).
3. J. B. Wang, L. X. Liu, "Use of photodynamic therapy in malignant lesions of stomach, bile duct, pancreas, colon and rectum," *Hepatogastroenterology* **54**, 718–724 (2007).
4. M. A. D'Hallewin, D. Kochetkov, Y. Viry-Babel, A. Leroux, E. Werkmeister, D. Dumas, S. Gräfe, V. Zorin, F. Guillemin, L. Bezdetnaya, "Photodynamic therapy with intratumoral administration of lipid-based mTHPC in a model of breast cancer recurrence," *Lasers Surg. Med.* **40**, 543–549 (2008).
5. B. J. Tromberg, J. Coquoz, O. Fishkin, J. B. Pham, T. Anderson, E. R. Butler, J. Cahn, M. Gross, J. D. Venugopalan, D. Pham, "Non-invasive measurements of breast tissue optical properties using frequency-domain photon migration," *Phil. Trans. R. Soc. Lond. B* **352**, 661–668 (1997).
6. B. W. Pogue, S. P. Poplack, T. O. McBride, W. A. Wells, K. S. Osterman, U. L. Osterberg, K. D. Paulsen, "Quantitative hemoglobin tomography with diffuse near-infrared spectroscopy: Pilot results in the breast," *Radiology* **218**, 261–266 (2001).
7. V. Ntziachristos, B. Chance, "Probing physiology and molecular function using optical imaging: Applications to breast cancer," *Breast Cancer Res.* **3**, 41–46 (2001).
8. R. Choe, A. Corlu, K. Lee, T. Durduran, S. D. Konecky, M. Grosicka-Koptyra, S. R. Arridge, B. J. Czerniecki, D. L. Fraker, A. DeMichele, B. Chance, M. A. Rosen, A. G. Yodh, "Diffuse optical tomography of breast cancer during neoadjuvant chemotherapy: A case study with comparison to MRI," *Med. Phys.* **32**, 1128–1139 (2005).
9. M. A. Franceschini, K. T. Moesta, S. Fantini, G. Gaida, E. Gratton, H. Jess, W. W. Mantulin, M. Seeber, P. M. Schlag, M. Kaschke, "Frequency-domain techniques enhance optical mammography: Initial clinical results," *Proc. Nat. Acad. Sci. USA* **94**, 6468–6473 (1997).
10. Q. Zhu, E. B. Cronin, A. A. Currier, H. S. Vine, M. Huang, N. Chen, C. Xu, "Benign versus malignant breast masses: Optical differentiation with US-guided optical imaging reconstruction," *Radiology* **237**, 57–66 (2005).
11. H. M. Ross, J. A. Smelstoys, G. J. Davis, A. S. Kapatkin, F. Del Piero, E. Reineke, H. Wang, T. C. Zhu, T. M. Busch, A. G. Yodh, S. M. Hahn, "Photodynamic therapy with motexafin lutetium for rectal cancer: A preclinical model in the dog," *J. Surg. Res.* **135**, 323–330 (2006).
12. A. A. Oraevsky, S. L. Jacques, F. K. Tittel, "Measurement of tissue optical properties by time-resolved detection of laser-induced transient stress," *Appl. Opt.* **36**, 402–415 (1997).
13. Q. Chen, B. C. Wilson, S. D. Shetty, M. S. Patterson, J. C. Cerny, F. W. Hetzel, "Changes in *in vivo* optical properties and light distributions in normal canine prostate during photodynamic therapy," *Radiat. Res.* **147**, 86–91 (1997).
14. L. K. Lee, C. Whitehurst, Q. Chen, M. L. Pantelides, F. W. Hetzel, J. V. Moore, "Interstitial photodynamic therapy in the canine prostate," *Br. J. Urol.* **80**, 898–902 (1997).
15. W. H. Nau, R. J. Roselli, D. F. Milam, "Measurement of thermal effects on the optical properties of prostate tissue at wavelengths of 1,064 and 633 nm," *Lasers Surg. Med.* **24**, 38–47 (1999).
16. L. Lilge, N. Pomerleau-Dalcourt, A. Douplik, S. H. Selman, R. W. Keck, M. Szkudlarek, M. Pestka, J. Jankun, "Transperineal *in vivo* fluence-rate dosimetry in the canine prostate during SnET2-mediated PDT," *Phys. Med. Biol.* **49**, 3209–3225 (2004).
17. J. Jankun, L. Lilge, A. Douplik, R. W. Keck, M. Pestka, M. Szkudlarek, P. J. Stevens, R. J. Lee, S. H. Selman, "Optical characteristics of the canine prostate at 665 nm sensitized with tin etiopurpurin dichloride: Need for real-time monitoring of photodynamic therapy," *J. Urol.* **172**, 739–743 (2004).

18. J. Jankun, R. W. Keck, E. Skrzypczak-Jankun, L. Lilge, S. H. Selman, "Diverse optical characteristic of the prostate and light delivery system: Implications for computer modelling of prostatic photodynamic therapy," *B. J. U. Int.* **95**, 1237–1244 (2005).
19. M. Solonenko, R. Cheung, T. M. Busch, A. Kachur, G. M. Griffin, T. Vulcan, T. C. Zhu, H. W. Wang, S. M. Hahn, A. G. Yodh, "In vivo reflectance measurement of optical properties, blood oxygenation and motexafin lutetium uptake in canine large bowels, kidneys and prostates," *Phys. Med. Biol.* **47**, 857–873 (2002).
20. T. C. Zhu, S. M. Hahn, A. S. Kapatkin, A. Dimofte, C. E. Rodriguez, T. G. Vulcan, E. Glatstein, R. A. Hsi, "In vivo optical properties of normal canine prostate at 732 nm using motexafin lutetium-mediated photodynamic therapy," *Photochem. Photobiol.* **77**, 81–88 (2003).
21. G. Xu, D. Piao, C. H. Musgrove, C. F. Bunting, H. Dehghani, "Trans-rectal ultrasound-coupled near-infrared optical tomography of the prostate Part I: Simulation," *Opt. Exp.* **16**, 17484–17504 (2008).
22. Z. Jiang, D. Piao, G. Xu, J. W. Ritchey, G. R. Holyoak, K. E. Bartels, C. F. Bunting, G. Slobodov, J. S. Krasinski, "Trans-rectal ultrasound-coupled near-infrared optical tomography of the prostate Part II: Experimental demonstration," *Opt. Exp.* **16**, 17505–17520 (2008).
23. J. Boutet, L. Guyon, M. Debourdeau, J. M. Dinten, D. Vray, P. Rizo, "Advances in bi-modal optical and ultrasound detection of prostate cancer diagnosis," *Proc. SPIE* **7171**, 71710E (2009).
24. T. Svensson, S. Andersson-Engels, M. Einarsson, K. Svanberg, "In vivo optical characterization of human prostate tissue using near-infrared time-resolved spectroscopy," *J. Biomed. Opt.* **12**, 014022 (2007).
25. N. Iftimia, H. Jiang, "Quantitative optical image reconstruction of turbid media by use of direct-current measurements," *Appl. Opt.* **39**, 5256–5261 (2000).
26. H. Xu, *MRI-Coupled Broadband Near-Infrared Tomography for Small Animal Brain Studies*, Ph.D. Dissertation, Dartmouth College, Hanover, NH, p. 36 (2005).
27. F. Bevilacqua, A. J. Berger, A. E. Cerussi, D. Jakubowski, B. J. Tromberg, "Broadband absorption spectroscopy in turbid media by combined frequency-domain and steady-state methods," *Appl. Opt.* **39**, 6498–6510 (2000).

***In vivo* trans-rectal ultrasound-coupled optical tomography of a transmissible venereal tumor model in the canine pelvic canal**

Zhen Jiang,^a G. Reed Holyoak,^b Kenneth E. Bartels,^b Jerry W. Ritchey,^c Guan Xu,^a Charles F. Bunting,^a Gennady Slobodov,^d and Daqing Piao^{a,*}

^aOklahoma State University, School of Electrical and Computer Engineering, Stillwater, Oklahoma 74078

^bOklahoma State University, Department of Veterinary Clinical Sciences, Stillwater, Oklahoma 74078

^cOklahoma State University, Department of Veterinary Pathobiology, Stillwater, Oklahoma 74078

^dUniversity of Oklahoma Health Sciences Center, Department of Urology, Oklahoma City, Oklahoma 73104

Abstract. *In vivo* trans-rectal near-infrared (NIR) optical tomography was performed concurrently with, albeit reconstructed without spatial *a priori* of, trans-rectal ultrasound (US) on transmissible venereal tumor (TVT) developed as a model in the canine pelvic canal. Studies were taken longitudinally at prior to, 14 days after, and 35 days after the TVT injection. As the tumor grew, the nodules became increasingly hyperabsorptive and moderately hyper-scattering on NIR. The regions of strong NIR contrast, especially on absorption images, correlated well with those of US hypoechoic masses indicative of tumors. Combining the information of trans-rectal NIR and US detected the tumor more accurately than did the US alone at 14 days postinjection. © 2009 Society of Photo-Optical Instrumentation Engineers. [DOI: 10.1117/1.3149852]

Keywords: prostate cancer; trans-rectal optical tomography; transmissible venereal tumor; trans-rectal ultrasound.

Paper 09010LR received Jan. 14, 2009; revised manuscript received Mar. 9, 2009; accepted for publication Apr. 17, 2009; published online Jun. 8, 2009.

1 Introduction

Near-infrared (NIR) optical tomography is becoming increasingly important for functional imaging of biological tissues¹ because the endogenous or exogenous NIR contrast could benchmark tissue physiology and functionality. NIR optical tomography has contributed to diagnosis and prognosis of cancer,² understanding of cerebral response,³ characterization of rheumatologic dysfunction,⁴ and small animal imaging.⁵ In all these applications, the tissues have been interrogated non-invasively via external NIR applicators.

NIR optical tomography based on trans-rectal “noninvasive” probing has been investigated recently by the authors, attempting to augment trans-rectal ultrasound (TRUS)⁶ of

prostate with the unique optical specificity. This approach was motivated by the hypothesis that optical properties of prostate cancer *in vivo* may be different from those of normal intact prostate tissues and was challenged by the difficulty of assessing the prostate in its *in vivo* real-time environment. This work demonstrates *in vivo* trans-rectal NIR optical tomography, conducted concurrently with TRUS, on a dog bearing transmissible venereal tumors (TVTs)⁷ in its pelvic canal. This study not only validates the utility of *in vivo* trans-rectal NIR tomography of the prostate but also reveals, for the first time, the NIR contrasts that TVT has over the normal tissues within the canine pelvic canal.

2 Methods and Materials

The studies were conducted under a protocol approved by the Institutional Animal Care and Use Committee of Oklahoma State University. The protocol was also approved and underwent an on-site inspection by the U.S. Army Medical Research and Materiel Command. For this study, the prostate of a 12-kg sexually intact adult purpose-bred Beagle dog estimated to be approximately four years of age was used. The TVT cell line was obtained cryopreserved from MD Anderson Cancer Center (Houston, Texas). Following two cycles of inoculation into the subcutis of non-obese-diabetic/severe-combined-immunodeficiency (NOD/SCID) mice, neoplastic cells were recovered and homogenized for injection into the canine prostate gland. Approximately 3 cc of TVT cells were aseptically injected transperineally into the right lobe of the prostate using a 6-in. 16-gauge hypodermic needle under TRUS visualization. During retraction of the injection needle, it was assumed that TVT cells could leak from the prostate injection site and be “seeded” along the needle insertion tract. During the first 14 days postinjection, there was no evidence of tumor growth on TRUS and rectal examination. The TRUS examination at 35 days postinjection showed hypoechoic masses in the prostatic parenchyma, periprostatically around the right lobe of the prostate, and perirectally along the track of needle injection. The dog underwent weekly monitoring for two more weeks and was then humanely euthanized for necropsy and histological examinations at 56 days postinjection.

The trans-rectal NIR/US system was described elsewhere.⁶ The NIR probe has been integrated with a 60-mm-long sagittal TRUS transducer. The 60-mm length of the NIR source/detector arrays limits the imaging depth to ~30 mm. The steady-state NIR measurements reconstruct the absorption and reduced scattering images without *a priori* structural information.⁶

3 Results

Figure 1 presents the trans-rectal NIR and US images acquired at the middle of the right lobe, the middle line of the prostate, and the middle of the left lobe, which were obtained before the TVT injection, 14 days postinjection, and 35 days postinjection. The absorption [Fig. 1(a)] and reduced scattering [Fig. 1(b)] images correlate to the same set of US images. The image dimensions are 60 × 30 mm² (cranial-caudal × dorsal-ventral). On the day-35 US images of the right lobe

*Address all correspondence to: Daqing Piao, Tel: 405-744-5250; E-mail: daqing.piao@okstate.edu

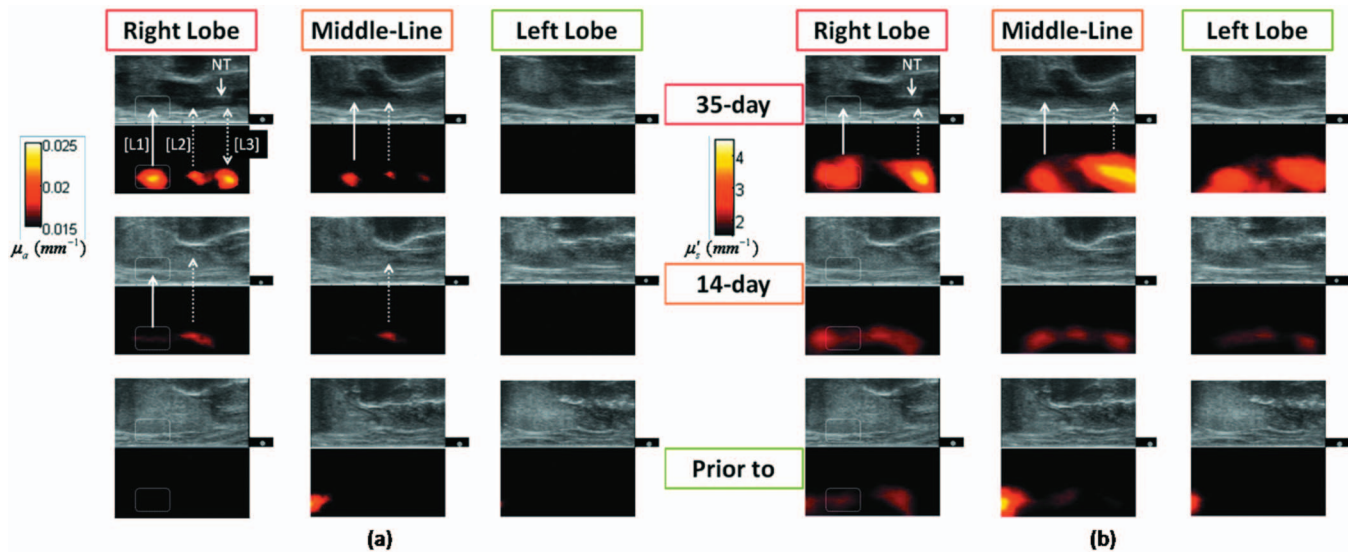


Fig. 1 *In vivo* trans-rectal NIR/US of TVT development in canine pelvic canal. The images were taken before the TVT injection, 14 days after the TVT injection when the US and rectal examination showed no evidence of tumor growth, and 35 days after the TVT injection when the tumor growth was evident on both US and rectal examination. (a) US and NIR absorption images. (b) US and NIR reduced scattering images. The dimensions of the images are $60 \times 30 \text{ mm}^2$ (cranial-caudal \times dorsal-ventral). The rectangular mark enclosing L1 is used in Fig. 2(a), where the peak NIR contrasts within the region are plotted. NT: needle track.

and middle line, the hypoechoic region “L1” indicated an intraprostatic mass; the large hypoechoic region “L2” indicated a mass ventral and caudal to the prostate that could have a connection with L1; the needle track (NT) on the right lobe denoted the needle trajectory for introducing the TVT cells with longitudinal hypoechoic regions, including L3, seen along the NT. On the day-35 NIR image of the right lobe, the hyperabsorptive regions corresponded longitudinally to L1, L2, and L3. The day-35 NIR image of the middle line displayed less and smaller hyperabsorptive masses, indicative of L1, L2, and L3. Trans-rectal NIR/US images performed at the left lobe were shown with no abnormal features on US and no hyperabsorptive regions on NIR. At the day-14 NIR absorption images, hyperabsorptive regions were found intraprostatically in the right lobe only (L1) and dorsal to the pelvic bone in the right lobe (L2), with potential extension to the middle line. The longitudinal locations of these hyperabsorptive regions correlated well with those of the hypoechoic and hyper-

absorptive regions found in day-35. Because the NIR array surface is 3 mm ventral to the TRUS surface, the nodules were shown to be slightly dorsal on the NIR versus on the US images. The change of the hyperabsorptive regions from day-14 to day-35 implied tumor growing in the right lobe and extending toward the middle line. The growth of the tumor was indicated earlier by the NIR absorption images than by the TRUS, and combining the information of NIR and TRUS led to earlier and more accurate findings of tumor growth than did TRUS alone.

The hyperabsorptive masses in Fig. 1(a) were shown in Fig. 1(b) with different patterns of the contrast. In Fig. 1(b), the L3 had much higher contrast than did the other masses corresponding to L1 and L2. The growth of tumors L1 and L2 at day-14 in Fig. 1(b) are not as evident as in Fig. 1(a).

The progressions of the peak NIR contrasts within the rectangular region corresponding to L1 as outlined in Fig. 1, with

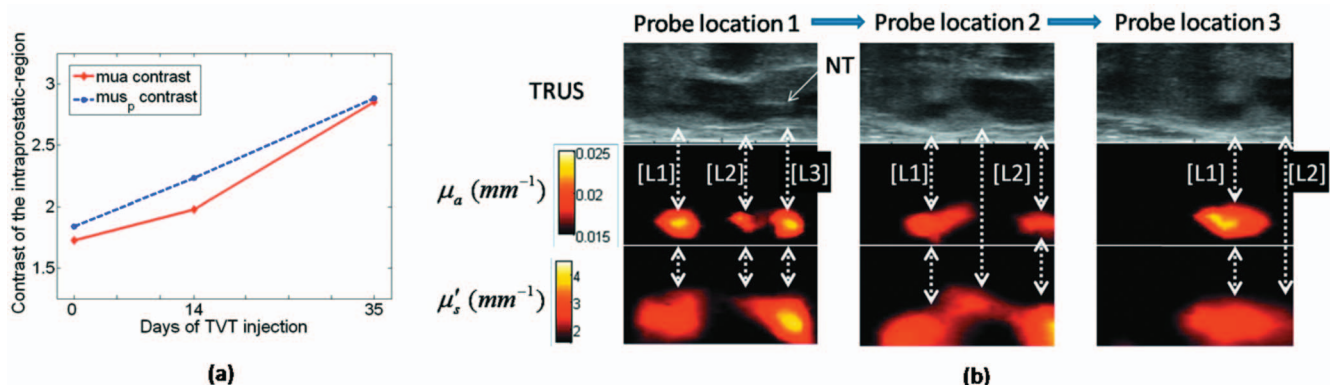


Fig. 2 (a) The progression of peak NIR contrasts within the rectangular region specified in Fig. 1. (b) Sagittal trans-rectal NIR/US imaging in three longitudinal locations. The locations of the left-column images correspond to those of the right lobe taken at day-35 in Fig. 1.

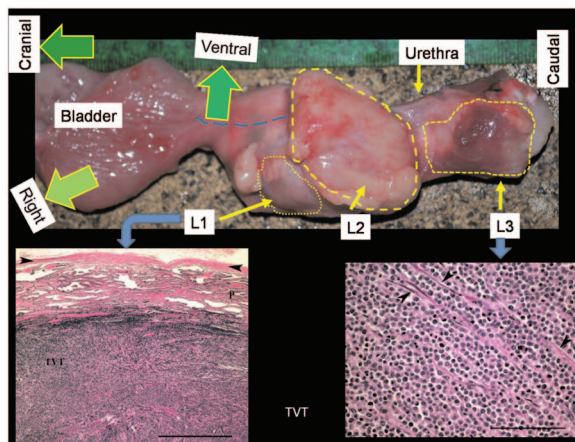


Fig. 3 (Top) Image of prostate gland taken after removal of the urinary bladder and intrapelvic urethra immediately following euthanasia. The prostate gland is markedly expanded and misshapen secondary to intraprostatic (L1) and periprostatic (L2) neoplastic masses. Neoplastic masses were also distributed along the distal intrapelvic urethra (L3) and in the perirectal subcutaneous tissues (not shown). Histologically, expansile masses of TVT (cells bottom left panel) displace and compress prostatic tissue (P). Prostatic capsule (arrowheads), bar = 1.8 mm. The TVT infiltrate (bottom right panel) consists of sheets of neoplastic round cells dissecting through preexisting fibrovascular stroma (arrowheads), bar = 230 μ m.

respect to the background values for normal perirectal parenchyma, are given in Fig. 2(a). The clear trend of contrast increase is believed as the demonstration of imaging the tumor growth because NIR tomography is a nonlinear process in which the enlargement of the target may be reconstructed as having elevated contrast in addition to volume changes when reconstructed without the spatial *prior* information of the target.

Figure 2(b) displays the NIR/US images obtained by placing the probe at three locations along the middle plane of the right lobe. At location 1, L1, L2, and L3 (refer to Fig. 1) were all within the US field of view, whereas at location 2 the L3 was moved out of the US view. At location 3, only L1 was shown on US. The overall NIR hypercontrast masses correlated well with the US hypoechoic regions.

The gross and histological findings (56 days postinjection) in Fig. 3 confirmed intra- and periprostatic neoplastic infiltrates with masses also located along the urethra and perirectal tissue; the latter related to dissemination along the needle track during TVT inoculation. All masses consist of diffuse sheets of a monomorphic population of neoplastic round cells dissecting through preexisting fibrovascular stroma. The neoplastic cells have large hyperchromatic nuclei, single conspicuous nucleoli, and moderate amounts of featureless cytoplasm. The cytological features are consistent with canine TVT.

4 Discussions and Conclusion

The intraprostatic TVT tumors were initiated in a non-immunosuppressed canine model in which the TVT nodules

developed at multiple sites intraprostatically and periprostatically. Although not all TVT tumors were confined to the prostate, successful imaging of multiple TVT nodules implies the utility of detecting multiple intraprostatic tumors.

The feature of TVT as strongly hyperabsorptive on NIR tomography is likely due to the hyperchromatic nuclei unique to TVT. The relatively higher scattering of the TVT may be due to the hyperdensity and larger nuclei of the neoplastic cells. As the neoplastic cells are arranged into microlobules by the preexisting fibrovascular stroma, the TVT may also present certain polarization sensitivity. Overall, the NIR features of TVT may be comparable to those revealed by tissue angiogenesis. As studies of microvessel-density within the human prostate demonstrated a clear correlation of increased microvessel density with the presence of cancer,⁸ it can be expected that human prostate cancer may have notable contrast on trans-rectal NIR tomography.

In conclusion, this work reports *in vivo* imaging of TVT tumors in the canine pelvic canal by trans-rectal NIR tomography coupled with TRUS. The TVT tumor nodules were presented as hyperabsorptive and hyperscattering with respect to the normal prostatic and other pelvic tissues. Correlation of the TVT locations is found between trans-rectal NIR and TRUS images. These demonstrations encourage testing of trans-rectal NIR tomography with additional animal studies and eventually to the human prostate.

Acknowledgments

The authors acknowledge support from U.S. Army Medical Research and Material Command through Grant No. W81XWH-07-1-0247.

References

1. E. M. Hillman, "Optical brain imaging *in vivo*: techniques and applications from animal to man," *J. Biomed. Opt.* **12**, 051402 (2007).
2. B. J. Tromberg, B. W. Pogue, K. D. Paulsen, A. G. Yodanis, D. A. Boas, and A. E. Cerussi, "Assessing the future of diffuse optical imaging technologies for breast cancer management," *Med. Phys.* **35**(6), 2443–2451 (2008).
3. B. W. Zeff, B. R. White, H. Dehghani, B. L. Schlaggar, and J. P. Culver, "Retinotopic mapping of adult human visual cortex with high-density diffuse optical tomography," *Proc. Natl. Acad. Sci. U.S.A.* **104**, 12169–12174 (2007).
4. A. K. Scheel, M. Backhaus, A. D. Klose, B. Moa-Anderson, U. J. Netz, K. G. Hermann, J. Beuthan, G. A. Müller, G. R. Burmester, and A. H. Hielscher, "First clinical evaluation of sagittal laser optical tomography for detection of synovitis in arthritic finger joints," *Ann. Rheum. Dis.* **64**, 239–245 (2005).
5. M. B. Unlu, Y. Lin, O. Birgul, O. Nalciglu, and G. Gulsen, "Simultaneous *in vivo* dynamic magnetic resonance-diffuse optical tomography for small animal imaging," *J. Biomed. Opt.* **13**, 060501 (2008).
6. Z. Jiang, D. Piao, G. Xu, J. W. Ritchey, G. R. Holyoak, K. E. Bartels, C. F. Bunting, G. Slobodov, and J. S. Krasinski, "Trans-rectal ultrasound-coupled near-infrared optical tomography of the prostate, Part II: experimental demonstration," *Opt. Express* **16**, 17505–17520 (2008).
7. B. Rivera, K. Ahrar, M. M. Kangasniemi, J. D. Hazle, and R. E. Price, "Canine transmissible venereal tumor: a large-animal transplantable tumor model," *Comparative Med.* **55**(4), 335–343 (2005).
8. S. A. Bigler, R. E. Deering, and M. K. Brawer, "Comparison of microscopic vascularity in benign and malignant prostate tissue," *Hum. Pathol.* **24**, 220–226 (1993).

Photon diffusion in a homogeneous medium bounded externally or internally by an infinitely long circular cylindrical applicator.

I. Steady-state theory

Anqi Zhang,¹ Daqing Piao,^{1,*} Charles F. Bunting,¹ and Brian W. Pogue²

¹*School of Electrical and Computer Engineering, Oklahoma State University, Stillwater, Oklahoma 74078, USA*

²*Thayer School of Engineering, Dartmouth College, Hanover, New Hampshire, 03755, USA*

*Corresponding author: daqing.piao@okstate.edu

Received October 5, 2009; revised January 13, 2010; accepted January 14, 2010;
posted January 15, 2010 (Doc. ID 118134); published February 26, 2010

This work presents an analytic treatment for photon diffusion in a homogeneous medium bounded externally or internally by an infinitely long circular cylindrical applicator. Focusing initially on the steady-state condition, the photon diffusion in these two geometries is solved in cylindrical coordinates by using modified Bessel functions and by applying the extrapolated boundary condition. For large cylinder diameter, the analytic solutions may be simplified to a format employing the physical source and its image source with respect to a semi-infinite geometry and a radius-dependent term to account for the shape and dimension of the cylinder. The analytic solutions and their approximations are evaluated numerically to demonstrate qualitatively the effect of the applicator curvature—either concave or convex—and the radius on the photon fluence rate as a function of the source–detector distance, in comparison with that in the semi-infinite geometry. This work is subjected to quantitative examination in a coming second part and possible extension to time-resolved analysis. © 2010 Optical Society of America

OCIS codes: 170.3660, 170.5280, 170.6960.

1. INTRODUCTION

Using near-infrared (NIR) light to image large or deep tissue volumes non-invasively has largely been based on transport modeling with the diffusion approximation to the radiative transport equation [1]. Non-invasive diffuse optical imaging is always involved with some kind of applicator–tissue interface or air–tissue interface, because the light has to be delivered and detected at the surface of the tissue. For any specific applicator or imaging geometry, the analytic model predicting the photon fluence rate to be measured at the applicator–tissue interface dictates the accuracy of calibrating the system using a known homogeneous medium and recovering unknown optical properties of a heterogeneous medium. The analytic solutions to photon diffusion in an infinite homogeneous medium are the least complicated approach, and are solved straightforwardly in spherical coordinates. For a homogeneous medium bounded by an infinite plane edge, which conventionally is referred to as the semi-infinite geometry, the analytic solution to photon diffusion is also well-studied [2] and has been applied widely to analyze raw data measured from surface tissue applicators and for image reconstruction.

When NIR light diffusion is utilized for imaging of the breast, neonatal brain, joints, rodents, etc., the geometry of the applicator often has a planar or concave (with respect to the direction of source illumination) boundary. When a medium is enclosed by a ring-shaped applicator, the photon diffusion within the medium has been modeled as in an infinite medium for a ring applicator of con-

siderable size [3]. For this type of ring applicator, the photon intensity measured at a site on the applicator interface and 180° to the source may resemble that measured in an infinite medium; however, the photon intensity measured at a site on the applicator interface but closer to the source should resemble more that measured in a semi-infinite medium. This inconsistency implies the inaccuracy of modeling the photon diffusion for a ring applicator based on either infinite or semi-infinite geometry. Accurate treatment of the circular concave boundary, as for a ring applicator, requires analysis in cylindrical coordinates. The model of photon diffusion in a medium bounded externally by a circular cylindrical applicator has been investigated previously in several elegant studies. Arridge *et al.* [4] used a boundary condition of zero fluence at the applicator interface to derive the time-domain and frequency-domain solutions for finite and infinite cylinders using Bessel functions and modified Bessel functions. The more accurate extrapolated boundary condition [5,6] was applied to similar concave applicator geometry by Pogue and Patterson [7] for a finite cylinder and Sassaroli *et al.* [8] for an infinite cylinder to express the time-domain solutions by use of Bessel functions. These studies provided important insight into photon diffusion in a medium bounded by a concave applicator, which mostly applies to diffuse optical imaging of the breast. Sassaroli *et al.* [8] also studied the effect of a concave boundary with diameters of 30–50 mm, in comparison with the semi-infinite plan boundary in the perspective of an inverse problem. The time-domain results for a

concave applicator have been applied to the frequency domain by Fourier transformation as in [7], and can be extended to the steady state by temporal integration.

Recently work by our group [9,10] as well as others [11,12] has investigated different aspects of applying diffuse optical tomography to imaging internal organs such as the prostate using an endo-rectal probe. This type of imaging geometry requires a convex-shaped applicator. The analytic model of photon diffusion in compliance with such convex geometry, simplified by a diffusive medium bounded internally by a cylindrical applicator, has not been derived previously. Accurate modeling of photon propagation in a specific convex geometry could certainly be rendered by Monte Carlo methods [8]. The finite-element solution of photon diffusion [10,11] in such convex geometry may also prove sufficiently accurate in the diffusion regime. Given the availability of numerical means, finding the analytic model of photon diffusion is still imperative and important, as it ultimately is beneficial to calibrating measurement data and improving reconstruction accuracy. What and how accurately such diffusion-based model could predict at the smaller scale of the convex geometry for applications such as endo-rectal imaging is especially interesting.

In this work the photon diffusion is analyzed in both external and internal imaging geometries, in which the medium being interrogated is bounded either externally or internally by an infinitely long circular cylindrical applicator. These two geometries resemble imaging the breast using a ring-shaped applicator and imaging the prostate using an endo-rectal probe, respectively. These studies are conducted initially for steady-state photon diffusion only, which is nonetheless adequate in terms of assessing the effect of the cylindrical interface on photon fluence rate when compared with a semi-infinite boundary. The initial works are to be presented in two papers. In this the first part, the Green's function of the photon diffusion equation in an infinite medium geometry is first expanded in cylindrical coordinates to a closed form expressed by modified Bessel functions. Then the extrapolated boundary condition is employed to apply the image-source method to the geometries of a "concave" cylindrical applicator and a "convex" cylindrical applicator, respectively. The analytic solutions are then simplified to a format, valid for large cylinder diameters, that includes the physical source and its image source with respect to the associated semi-infinite geometry and a radius-dependent term to account for the shape and dimension of the cylinder. The simplified format reveals that, as the radius of the cylinder increases, the analytic solution of the photon diffusion for it approaches the well-known semi-infinite result. The analytic solutions and their simplified formats are then evaluated numerically for two specific geometries, one having the source and the detector on the surface positioned only along the azimuthal direction and the other along the longitudinal direction. Placing the source-detector either azimuthally or longitudinally demonstrates explicitly the effect of the applicator curvature, either concave or convex, and the radius of the applicator curvature on the decay of photon fluence rate as a function of the source-detector distance in comparison with that in the semi-infinite geometry. As the radius of the cy-

lindrical applicator increases, the numerically evaluated photon diffusion for it asymptotically approaches that for a semi-infinite geometry, as expected. The features of steady-state photon diffusion for cylindrical concave and convex applicators analyzed theoretically and evaluated qualitatively in this first part will be examined quantitatively in the second part. The study may also be extended to time-resolved analysis in the future.

2. ANALYTIC APPROACH AND GEOMETRIES EXAMINED

A. Steady-State Photon Diffusion in an Infinite Medium: Solution in Cylindrical Coordinates

The steady-state photon diffusion equation is expressed by [2–6]

$$\nabla^2 \Psi(\vec{r}) - \frac{\mu_a}{D} \Psi(\vec{r}) = -\frac{S(\vec{r})}{D}, \quad (2.1.1)$$

where Ψ is the photon fluence rate at position \vec{r} , μ_a is the absorption coefficient, $D = [3(\mu_a + \mu'_s)]^{-1}$ is the diffusion coefficient with μ'_s being the reduced scattering coefficient, and S is the source. Considering a source at \vec{r}' of (ρ', φ', z') and a detector at \vec{r} of (ρ, φ, z) in cylindrical coordinates, the equation for the Green's function of Eq. (2.1.1) is

$$\nabla^2 G(\vec{r}, \vec{r}') - k_0^2 G(\vec{r}, \vec{r}') = -\delta(\vec{r} - \vec{r}'), \quad (2.1.2)$$

where $k_0 = \sqrt{\mu_a/D}$ is the effective attenuation coefficient. The Dirac delta function in Eq. (2.1.2) is

$$\delta(\vec{r} - \vec{r}') = (1/\rho) \delta(\rho - \rho') \delta(\varphi - \varphi') \delta(z - z'), \quad (2.1.3)$$

where the delta functions for φ and z can be written in terms of inverse Fourier series and inverse Fourier transform, respectively, by

$$\delta(\varphi - \varphi') = \frac{1}{2\pi} \sum_{m=-\infty}^{\infty} e^{im(\varphi - \varphi')} \quad (2.1.4)$$

and

$$\delta(z - z') = \frac{1}{2\pi} \int_0^\infty dk e^{ik(z - z')} = \frac{1}{\pi} \int_0^\infty dk \cos[k(z - z')]. \quad (2.1.5)$$

Substituting Eqs. (2.1.3)–(2.1.5) into Eq. (2.1.2) and expanding ∇^2 in Eq. (2.1.2) in cylindrical coordinates lead to

$$\begin{aligned} & \frac{1}{\rho} \frac{\partial}{\partial \rho} \left(\rho \frac{\partial G(\vec{r}, \vec{r}')}{\partial \rho} \right) + \frac{1}{\rho^2} \frac{\partial^2 G(\vec{r}, \vec{r}')}{\partial \varphi^2} + \frac{\partial^2 G(\vec{r}, \vec{r}')}{\partial z^2} - k_0^2 G(\vec{r}, \vec{r}') \\ &= -\frac{1}{2\pi^2 \rho} \delta(\rho - \rho') \sum_{m=-\infty}^{\infty} \int_0^\infty dk e^{im(\varphi - \varphi')} \cos[k(z - z')]. \end{aligned} \quad (2.1.6)$$

The Green's function can be expanded to a form similar to the right-hand side of Eq. (2.1.6) as

$$G(\vec{r}, \vec{r}') = \frac{1}{2\pi^2} \sum_{m=-\infty}^{\infty} \int_0^{\infty} dk \cdot g_m(k, \rho, \rho') \cdot e^{im(\varphi - \varphi')} \times \cos[k(z - z')], \quad (2.1.7)$$

where $g_m(k, \rho, \rho')$ is the radial Green's function to be solved. Substituting Eq. (2.1.7) into Eq. (2.1.6) leads to

$$\frac{1}{\rho} \frac{\partial}{\partial \rho} \left(\rho \frac{\partial g_m(k, \rho, \rho')}{\partial \rho} \right) - \left(k^2 + k_0^2 + \frac{m^2}{\rho^2} \right) g_m(k, \rho, \rho') = -\frac{1}{\rho} \delta(\rho - \rho'). \quad (2.1.8)$$

We define

$$k_{eff}^2 = k^2 + k_0^2 \quad \text{or} \quad k_{eff} = \sqrt{k^2 + k_0^2}. \quad (2.1.9)$$

Then Eq. (2.1.8) becomes

$$\frac{1}{\rho} \frac{\partial}{\partial \rho} \left(\rho \frac{\partial g_m(k, \rho, \rho')}{\partial \rho} \right) - \left(k_{eff}^2 + \frac{m^2}{\rho^2} \right) g_m(k, \rho, \rho') = -\frac{1}{\rho} \delta(\rho - \rho'). \quad (2.1.10)$$

Solutions to the Helmholtz Eq. (2.1.10) can be derived by following Jackson's approach of solving Poisson's equation [13] and using the asymptotic approximations of modified Bessel functions [14]. The solution details are given in Appendix A. With the solution for $g_m(k, \rho, \rho')$, we have

$$G(\vec{r}, \vec{r}') = \frac{1}{2\pi^2} \int_0^{\infty} dk \cdot \left\{ \sum_{m=0}^{\infty} \epsilon_m I_m(k_{eff} \rho_{<}) K_m(k_{eff} \rho_{>}) \times \cos[m(\varphi - \varphi')] \right\} \cdot \cos[k(z - z')], \quad (2.1.11)$$

where $\rho_{<}$ and $\rho_{>}$ indicate the smaller and larger radial coordinates of the source and the detector, and

$$\epsilon_m = \begin{cases} 2, & m \neq 0 \\ 1, & m = 0 \end{cases}. \quad (2.1.12)$$

Convolving the Green's function with the source term in Eq. (2.1.1) and assuming a point source renders the cylindrical-coordinate solution to the steady-state photon diffusion in an infinite homogeneous medium as

$$\Psi(\vec{r}, \vec{r}') = \frac{S}{2\pi^2 D} \int_0^{\infty} dk \cdot \left\{ \sum_{m=0}^{\infty} \epsilon_m I_m(k_{eff} \rho_{<}) K_m(k_{eff} \rho_{>}) \times \cos[m(\varphi - \varphi')] \right\} \cdot \cos[k(z - z')]. \quad (2.1.13)$$

B. Steady-State Photon Diffusion in an Infinite Homogeneous Medium: Solution in Spherical Coordinates

The solution to Eq. (2.1.1) in spherical coordinates is well-known as

$$\Psi(\vec{r}, \vec{r}') = \frac{S}{4\pi D |\vec{r} - \vec{r}'|} e^{-k_0 |\vec{r} - \vec{r}'|}. \quad (2.2.1)$$

If the distance between a source and a detector is denoted by d , Eq. (2.2.1) is readily converted to

$$\ln(\Psi \cdot d) = -k_0 d + \ln\left(\frac{S}{4\pi D}\right). \quad (2.2.2)$$

Equation (2.2.2) indicates a linear relationship between the natural logarithm of the product of the fluence rate and the source–detector distance with respect to the source–detector distance, a characteristics useful for calibration with a homogeneous medium when an isotropic point source can be assumed. For the same homogeneous medium and source–detector geometry, the solutions given by Eqs. (2.2.1) and (2.1.13) will be identical to each other, which will be numerically validated in Section 4.

C. Steady-State Photon Diffusion in a Semi-infinite Medium: Solutions in Spherical Coordinates

The effect of an applicator boundary on photon diffusion has been rigorously modeled by the index-mismatched Robin-type (or Type III) boundary condition of

$$\Psi - 2AD \nabla \Psi \cdot \vec{n} = 0, \quad (2.3.1)$$

where $A = (1 + R_{eff})/(1 - R_{eff})$ and R_{eff} is the effective reflection coefficient [3] representing the percentage of the outgoing radiance integrated over all directions pointing toward the ambient medium that is converted to incoming radiance integrated over all directions pointing toward the scattering medium [15]. The Type III boundary condition (2.3.1), which is evaluated on the physical boundary, can be surrogated by an almost equally accurate but more convenient approach by use of a Type I boundary condition that is being evaluated on an “imaginary” boundary. The “imaginary” boundary, referred to as the “extrapolated” boundary [5,6], is located $2AD$ from the physical boundary and away from the medium. It is with respect to this extrapolated boundary that the negative “image” [16] of the source is introduced to set zero the fluence rate on this boundary.

We follow the notations introduced by Fantini *et al.* [2] for the semi-infinite geometry having a directional source and an isotropic detector located on a planar boundary, as illustrated in Fig. 1(a). The directional source is modeled as an isotropic source placed one reduced scattering distance into the medium. Then, based on the extrapolated boundary approach, the steady-state photon fluence rate reaching the detector located on the physical boundary is determined by the equivalent “real” isotropic source and its image source with respect to the extrapolated boundary in spherical coordinates as

$$\Psi = \Psi_{real} - \Psi_{imag} = \frac{S}{4\pi D l_{real}} e^{-k_0 l_{real}} - \frac{S}{4\pi D l_{imag}} e^{-k_0 l_{imag}}, \quad (2.3.2)$$

where

$$l_{real} = \sqrt{d^2 + R_a^2}, \quad R_a = 1/\mu'_s; \quad (2.3.3)$$

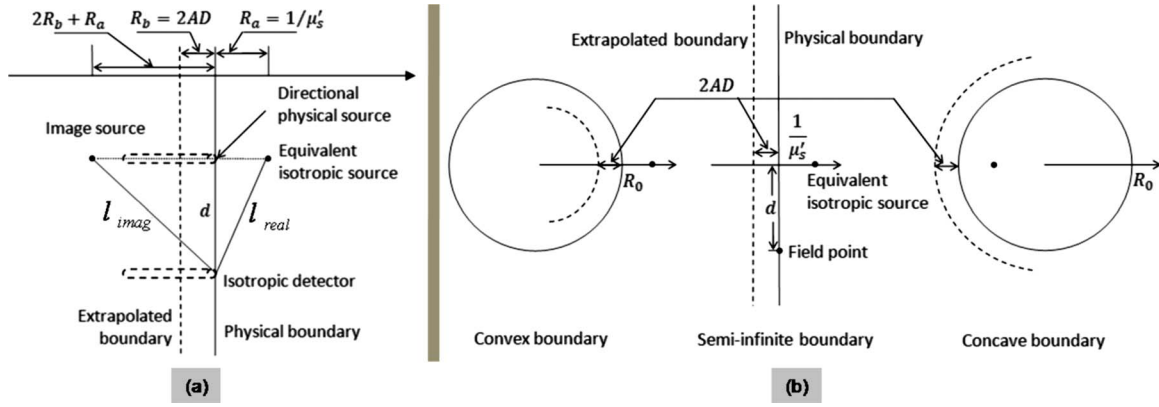


Fig. 1. (Color online) (a) Semi-infinite geometry [2]. The diffuse medium is to the right of the physical boundary, and the light is incident from the left. (b) The two cylindrical geometries in comparison with the semi-infinite geometry. The convex boundary represents that of a cylindrical applicator enclosed by the diffuse medium (e.g., imaging the prostate by a trans-rectal probe), and the concave boundary represents that of a cylindrical applicator enclosing the diffuse medium (e.g., imaging the breast by a ring probe).

$$l_{imag} = \sqrt{d^2 + (2R_b + R_a)^2}, \quad R_b = 2AD. \quad (2.3.4)$$

The d in relations (2.3.3) and (2.3.4) is the distance between the physical directional source and the detector, both located at the physical boundary, as in Eq. (2.2.2). For $d \gg R_a, R_b$, Eq. (2.3.2) converts [17] to

$$\ln(\Psi \cdot d^2) = -k_0 \cdot d + \ln\left(\frac{s}{2\pi D} \cdot k_0 R_b (R_a + R_b)\right), \quad (2.3.5)$$

which is the model-basis for calibrating in a semi-infinite homogeneous medium.

D. Cylindrical Interface Geometries Being Investigated in this Study

In this work, the “concave” geometry is defined as having the diffusive medium *enclosed* by an infinitely long cylindrical applicator, and the “convex” geometry as having the diffusive medium *enclosing* an infinitely long cylindrical applicator. The physical directional source is always modeled as an isotropic source placed one reduced scattering distance into the medium, as shown in Fig. 1(b). Usually, the extrapolated boundary condition is applicable when a diffusive medium bonds with a non-scattering region—a valid representation of either an external-imaging or an internal-imaging optical applicator. Since the distance of the extrapolated boundary from the physical boundary, $R_b = 2AD$ as in the semi-infinite geometry, is derived from the general expression of the boundary condition in Eq. (2.3.1), this distance will be considered as geometry-independent; therefore in the concave or convex geometry the extrapolated boundary will also be located at a radial distance $R_b = 2AD$ from the physical boundary and away from the diffusive medium. Obviously, as the radius reaches infinity both concave and convex geometries approach the semi-infinite geometry. This feature serves as both the qualitative and quantitative measure of the analytic solutions derived for the concave and convex probe geometries.

3. STEADY-STATE PHOTON DIFFUSION ASSOCIATED WITH CONCAVE OR CONVEX INFINITE CYLINDRICAL APPLICATOR

This section derives the cylindrical-coordinate solutions to steady-state photon diffusion in the concave and convex cylinder geometries. The same analytic principles apply to both the concave and convex geometries; however, the detailed analytic derivations of the two geometries are separately listed for completeness and for facilitating qualitative comparison between them.

A. External “Concave” Boundary; Analytic Solution

The concave geometry for a medium bounded externally by an infinitely long circular cylindrical applicator with

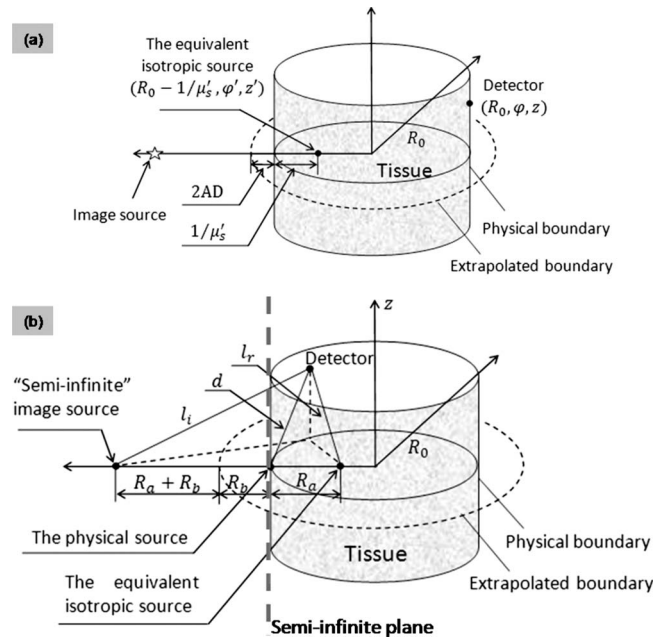


Fig. 2. (a) Details of the concave geometry indicating the equivalent isotropic source and the extrapolated boundary. The image source of the isotropic source with respect to the extrapolated boundary is located along the radial direction of the isotropic source due to symmetry. (b) The concave geometry and the “semi-infinite” image source that is the image source of the isotropic source with respect to a planar boundary tangential to the concave boundary at the location of the physical source.

radius R_0 is illustrated in Fig. 2(a). The physical source is located at (R_0, φ', z') and the detector is located at (R_0, φ, z) , both on the physical boundary.

1. Photon Diffusion under the Extrapolated Boundary Condition

As shown in Fig. 2(a), the equivalent “real” isotropic source must be located at $(R_0 - R_a, \varphi', z')$ based on the symmetry of the geometry, and the extrapolated boundary will be located at a radial distance of $R_b = 2AD$ outside the physical boundary. Based on the symmetry of the geometry, the image source of the “real” isotropic source with respect to the extrapolated boundary must also be located along the radial direction of the “real” isotropic or the physical source. This image source and the “real” isotropic source collectively set zero the photon fluence rate on the extrapolated boundary.

Based on Eq. (2.1.13), the photon fluence rate associated with the “real” isotropic source and evaluated on the extrapolated boundary, for which the source is located at $\rho_{r<} = R_0 - R_a$ and the detector is located at $\rho_{r>} = R_0 + R_b$, is

$$\begin{aligned} \Psi_{real|extr} = & \frac{1}{2\pi^2 D} \int_0^\infty dk \cdot \cos[k(z - z')] \\ & \cdot \left\{ \sum_{m=0}^\infty \epsilon_m S I_m[k_{eff}(R_0 - R_a)] K_m[k_{eff}(R_0 + R_b)] \right. \\ & \left. \times \cos[m(\varphi - \varphi')] \right\}, \end{aligned} \quad (3.1.1)$$

where the notation “ $left|right$ ” indicates evaluating the “left” as a source on the “right” as a boundary. Similarly, the photon fluence rate associated with the image source and evaluated on the extrapolated boundary for which the source is located at an unknown or yet-to-decide $\rho_{i>}$ but the detector is located at $\rho_{i<} = R_0 + R_b$, is

$$\begin{aligned} \Psi_{imag|extr} = & \frac{1}{2\pi^2 D} \int_0^\infty dk \\ & \cdot \left\{ \sum_{m=0}^\infty \epsilon_m S_m^* I_m[k_{eff}(R_0 + R_b)] K_m[k_{eff}\rho_{i>}] \right. \\ & \left. \times \cos[m(\varphi - \varphi')] \right\} \cdot \cos[k(z - z')]. \end{aligned} \quad (3.1.2)$$

In Eq. (3.1.2), the S_m^* terms are also unknown or yet-to-decide, besides $\rho_{i>}$. Based on the essential concept of “image-source” [16,18], the two unknown terms S_m^* and $\rho_{i>}$ associated with the m th order “image” source (the K_m component) can be expressed by a single unknown term of S_m associated with the same-order “real” source (the I_m component); that is,

$$S_m^* K_m(k_{eff}\rho_{i>}) = S_m I_m[k_{eff}\rho_{r<}] = S_m I_m[k_{eff}(R_0 - R_a)]. \quad (3.1.3)$$

Applying Eq. (3.1.3) to the extrapolated boundary condition of $\Psi_{real|extr} - \Psi_{imag|extr} = 0$, we have

$$S_m = S \frac{K_m[k_{eff}(R_0 + R_b)]}{I_m[k_{eff}(R_0 + R_b)]}, \quad m = 0, 1, 2, \dots \quad (3.1.4)$$

Now for the “real” isotropic source but evaluated at the physical boundary, the source is still located at $\rho_{r<} = R_0 - R_a$, but the detector is located at $\rho_{r>} = R_0$. For the “image” source, also evaluated at the physical boundary, the detector is located at $\rho_{i<} = R_0$, and the source terms are known through Eqs. (3.1.3) and (3.1.4). Collectively the photon fluence rate sensed by a detector at the physical boundary becomes

$$\begin{aligned} \Psi = \Psi_{real|phys} - \Psi_{imag|phys} = & \frac{S}{2\pi^2 D} \int_0^\infty dk \left\{ \cos[k(z - z')] \right. \\ & \cdot \sum_{m=0}^\infty \epsilon_m I_m[k_{eff}(R_0 - R_a)] K_m(k_{eff}R_0) \\ & \cdot \left. \left\langle 1 - \frac{I_m(k_{eff}R_0)}{K_m(k_{eff}R_0)} \frac{K_m[k_{eff}(R_0 + R_b)]}{I_m[k_{eff}(R_0 + R_b)]} \right\rangle \cos[m(\varphi - \varphi')] \right\}. \end{aligned} \quad (3.1.5)$$

2. Concave Geometry with a Large Cylinder Diameter: Approaching the Semi-infinite Geometry

As shown in Fig. 2(b), if a plane tangential to the cylinder at the physical source position is considered an imaginary semi-infinite planar boundary, then the “real” isotropic source in this semi-infinite geometry is still located at $(R_0 - R_a, \varphi', z')$, but the image source of the “real” isotropic source with respect to this semi-infinite boundary will be at $(R_0 + R_a + 2R_b, \varphi', z')$.

According to Eq. (2.1.13) the photon fluence rate sensed by a detector on the cylinder boundary due to the image source of the “real” isotropic source associated with the semi-infinite boundary is

$$\begin{aligned} \Psi_{imag|phys}^{semi} = & \frac{S}{2\pi^2 D} \int_0^\infty dk \cos[k(z - z')] \\ & \cdot \sum_{m=0}^\infty \epsilon_m I_m(k_{eff}R_0) K_m[k_{eff}(R_0 + R_a + 2R_b)] \\ & \times \cos[m(\varphi - \varphi')]. \end{aligned} \quad (3.1.6)$$

The photon fluence rate sensed by a detector on the cylinder boundary due to the image source of the “real” isotropic source associated with the cylinder boundary as seen in Eq. (3.1.5) can be rewritten to

$$\begin{aligned} \Psi_{imag|phys} = & \frac{S}{2\pi^2 D} \int_0^\infty dk \cos[k(z - z')] \\ & \cdot \sum_{m=0}^\infty \epsilon_m I_m(k_{eff}R_0) K_m[k_{eff}(R_0 + R_a + 2R_b)] \\ & \cdot \eta_m \cos[m(\varphi - \varphi')], \end{aligned} \quad (3.1.7)$$

where

$$\eta_m = \frac{I_m[k_{eff}(R_0 - R_a)]}{I_m[k_{eff}(R_0 + R_b)]} \frac{K_m[k_{eff}(R_0 + R_b)]}{K_m[k_{eff}(R_0 + R_a + 2R_b)]}. \quad (3.1.8)$$

If the cylinder diameter is sufficiently large, the modified Bessel functions in Eq. (3.1.8) can be simplified by their asymptotic expressions [14]; then Eq. (3.1.8) becomes

$$\eta_m = \sqrt{\frac{R_0 + R_a + 2R_b}{R_0 - R_a}}. \quad (3.1.9)$$

Substituting Eq. (3.1.9) into Eq. (3.1.7) and comparing with Eq. (3.1.6) we have

$$\Psi_{imag|phys} = \Psi_{imag|phys}^{semi} \cdot \sqrt{\frac{R_0 + R_a + 2R_b}{R_0 - R_a}}. \quad (3.1.10)$$

Hence, for the cylinder of sufficiently large diameter, Eq. (3.1.5) approximates to

$$\Psi = \Psi_{real|phys} - \Psi_{imag|phys} = \Psi_{real|phys} - \Psi_{imag|phys}^{semi} \cdot \sqrt{\frac{R_0 + R_a + 2R_b}{R_0 - R_a}}. \quad (3.1.11)$$

As $R_0 \rightarrow \infty$, the $\Psi_{real|phys}$ of Eq. (3.1.11) essentially becomes the Ψ_{real} in Eq. (2.3.2), $\sqrt{(R_0 + R_a + 2R_b)/(R_0 - R_a)} \rightarrow 1$, and the $\Psi_{imag|phys}^{semi}$ of Eq. (3.1.11) becomes the Ψ_{imag} in Eq. (2.3.2) because the detector located at (R_0, φ, z) reaches the imaginary semi-infinite boundary. This agrees with the physical aspect that an infinitely long concave cylindrical boundary becomes a semi-infinite boundary as the radius of the cylinder becomes infinity. By using the spherical-coordinate expression of the photon fluence rate given in Eq. (2.2.1), we can rewrite Eq. (3.1.11) as

$$\Psi = \frac{S}{4\pi D} \frac{e^{-k_0 l_r}}{l_r} - \frac{S}{4\pi D} \frac{e^{-k_0 l_i}}{l_i} \sqrt{\frac{R_0 + R_a + 2R_b}{R_0 - R_a}}. \quad (3.1.12)$$

B. Internal “Convex” Boundary; Analytic Solution

The convex geometry for a medium bounded internally by an infinitely long circular cylindrical applicator with radius R_0 is illustrated in Fig. 3(a). The physical source is located at (R_0, φ', z') and the detector is located at (R_0, φ, z) , both on the physical boundary.

1. Photon Diffusion under the Extrapolated Boundary Condition

As shown in Fig. 3(a), the equivalent “real” isotropic source must be located at $(R_0 + R_a, \varphi', z')$ based on the symmetry of the geometry, and the extrapolated boundary will be located at a radial distance $R_b = 2AD$ inside the physical boundary. Based on the symmetry of the geometry, the image source of the “real” isotropic source with respect to the extrapolated boundary must also be located along the radial direction of the “real” isotropic or the

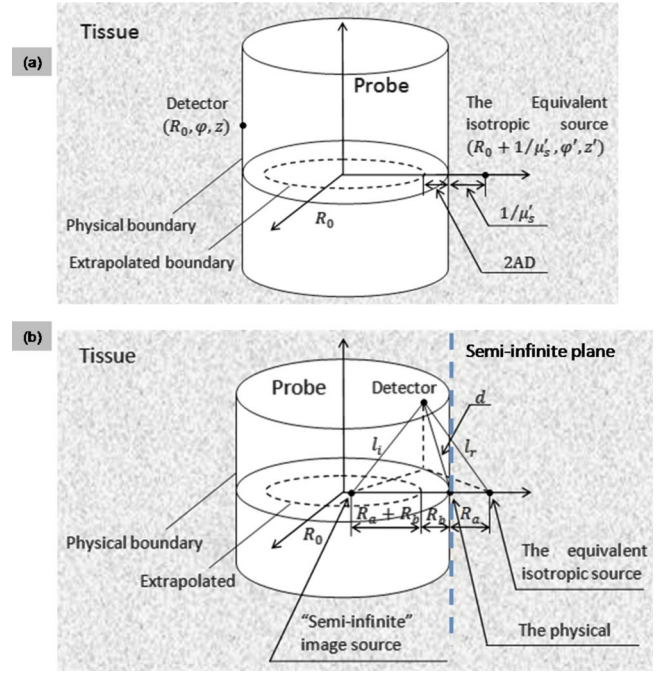


Fig. 3. (Color online) (a) Details of the convex geometry indicating the equivalent isotropic source and the extrapolated boundary. (b) The convex geometry and the “semi-infinite” image source that is the image source of the isotropic source with respect to a planar boundary tangential to the concave boundary at the location of the physical source.

physical source. This image source and the “real” isotropic source collectively set zero the photon fluence rate on the extrapolated boundary.

On the basis of Eq. (2.1.13), the photon fluence rate associated with the “real” isotropic source and evaluated on the extrapolated boundary, for which the source is located at $\rho_{r<} = R_0 - R_b$ and the detector is located at $\rho_{r>} = R_0 + R_a$, is

$$\Psi_{real|extr} = \frac{1}{2\pi^2 D} \int_0^\infty dk \cdot \cos[k(z - z')] \cdot \left\{ \sum_{m=0}^\infty \epsilon_m S I_m[k_{eff}(R_0 - R_b)] K_m[k_{eff}(R_0 + R_a)] \times \cos[m(\varphi - \varphi')] \right\}, \quad (3.2.1)$$

where we use the same notation “ $left|right$ ” as in Eq. (3.1.1). Similarly, the photon fluence rate associated with the image source and evaluated on the extrapolated boundary, for which the source is located at an unknown or yet-to-decide $\rho_{i<}$ but the detector is located at $\rho_{i>} = R_0 - R_b$, is

$$\Psi_{imag|extr} = \frac{1}{2\pi^2 D} \int_0^\infty dk \cdot \left\{ \sum_{m=0}^\infty \epsilon_m S_m^* I_m[k_{eff}\rho_{i<}] K_m[k_{eff}(R_0 - R_b)] \times \cos[m(\varphi - \varphi')] \right\} \cdot \cos[k(z - z')]. \quad (3.2.2)$$

In Eq. (3.2.2), the S_m^* terms are also unknown or yet-to-decide, besides $\rho_{i<}$. Following the approach of [16,18] as in Eq. (3.1.3), we have

$$S_m^* I_m(k_{\text{eff}} \rho_{i<}) = S_m K_m[k_{\text{eff}} \rho_{r>}] = S_m K_m[k_{\text{eff}}(R_0 + R_a)], \quad (3.2.3)$$

which expresses the two unknown terms S_m^* and $\rho_{i<}$ associated with the m th order “image” source (the I_m component) by a single unknown term of S_m associated with the same-order “real” source (the K_m component). Applying Eq. (3.2.3) to the extrapolated boundary condition of $\Psi_{\text{real}|_{\text{extr}}} - \Psi_{\text{imag}|_{\text{extr}}} = 0$ gives

$$S_m = S \frac{I_m[k_{\text{eff}}(R_0 - R_b)]}{K_m[k_{\text{eff}}(R_0 - R_b)]} \quad m = 0, 1, 2, \dots \quad (3.2.4)$$

Now for the “real” isotropic source but evaluated at the physical boundary, the source is still located at $\rho_{r>} = R_0 + R_a$, but the detector is located at $\rho_{r<} = R_0$. For the “image” source also evaluated at the physical boundary, the detector is located at $\rho_{i>} = R_0$, and the source terms are known through Eqs. (3.2.3) and (3.2.4). Collectively the photon fluence rate sensed by a detector at the physical boundary becomes

$$\begin{aligned} \Psi = \Psi_{\text{real}|_{\text{phys}}} - \Psi_{\text{imag}|_{\text{phys}}} &= \frac{S}{2\pi^2 D} \int_0^\infty dk \left\{ \cos[k(z - z')] \right. \\ &\cdot \sum_{m=0}^\infty \epsilon_m I_m(k_{\text{eff}} R_0) K_m[k_{\text{eff}}(R_0 + R_a)] \\ &\cdot \left. \left\langle 1 - \frac{K_m(k_{\text{eff}} R_0)}{I_m(k_{\text{eff}} R_0)} \frac{I_m[k_{\text{eff}}(R_0 - R_b)]}{K_m[k_{\text{eff}}(R_0 - R_b)]} \right\rangle \cos[m(\varphi - \varphi')] \right\}. \end{aligned} \quad (3.2.5)$$

2. Convex Geometry with a Large Cylinder Diameter: Approaching the Semi-infinite Geometry

As shown in Fig. 3(b), if a plane tangential to the cylinder at the physical source position is considered an imaginary semi-infinite planar boundary, then the “real” isotropic source in this semi-infinite geometry is still located at $(R_0 + R_a, \varphi', z')$, but the “image” source of the “real” isotropic source with respect to this semi-infinite boundary will be at $(R_0 - R_a - 2R_b, \varphi', z')$.

According to Eq. (2.1.13) the photon fluence rate sensed by a detector on the cylinder boundary due to the image source of the “real” isotropic source associated with the semi-infinite boundary is

$$\begin{aligned} \Psi_{\text{imag}|_{\text{phys}}}^{\text{semi}} &= \frac{S}{2\pi^2 D} \int_0^\infty dk \cos[k(z - z')] \\ &\cdot \sum_{m=0}^\infty \epsilon_m I_m[k_{\text{eff}}(R_0 - R_a - 2R_b)] K_m(k_{\text{eff}} R_0) \\ &\times \cos[m(\varphi - \varphi')]. \end{aligned} \quad (3.2.6)$$

The photon fluence rate sensed by a detector on the cylinder boundary due to the image source of the “real” isotropic source associated with the cylinder boundary, as seen in Eq. (3.2.5), can be rewritten to

$$\begin{aligned} \Psi_{\text{imag}|_{\text{phys}}} &= \frac{S}{2\pi^2 D} \int_0^\infty dk \cos[k(z - z')] \\ &\cdot \sum_{m=0}^\infty \epsilon_m I_m[k_{\text{eff}}(R_0 - R_a - 2R_b)] K_m(k_{\text{eff}} R_0) \\ &\cdot \eta_m \cos[m(\varphi - \varphi')], \end{aligned} \quad (3.2.7)$$

where

$$\eta_m = \frac{I_m[k_{\text{eff}}(R_0 - R_b)]}{I_m[k_{\text{eff}}(R_0 - R_a - 2R_b)]} \frac{K_m[k_{\text{eff}}(R_0 + R_a)]}{K_m[k_{\text{eff}}(R_0 - R_b)]}. \quad (3.2.8)$$

If the cylinder diameter is sufficiently large, the modified Bessel functions in Eq. (3.2.8) can be simplified by their asymptotic expressions [14]; then Eq. (3.2.8) becomes

$$\eta_m = \sqrt{\frac{R_0 - R_a - 2R_b}{R_0 + R_a}}. \quad (3.2.9)$$

Substituting Eq. (3.2.9) into Eq. (3.2.7) and comparing with Eq. (3.2.6) we have

$$\Psi_{\text{imag}|_{\text{phys}}} = \Psi_{\text{imag}|_{\text{phys}}}^{\text{semi}} \cdot \sqrt{\frac{R_0 - R_a - 2R_b}{R_0 + R_a}}. \quad (3.2.10)$$

Hence, for the cylinder of sufficiently large diameter, Eq. (3.2.5) approximates to

$$\begin{aligned} \Psi = \Psi_{\text{real}|_{\text{phys}}} - \Psi_{\text{imag}|_{\text{phys}}} &= \Psi_{\text{real}|_{\text{phys}}} \\ &- \Psi_{\text{imag}|_{\text{phys}}}^{\text{semi}} \cdot \sqrt{\frac{R_0 - R_a - 2R_b}{R_0 + R_a}}. \end{aligned} \quad (3.2.11)$$

As $R_0 \rightarrow \infty$, the $\Psi_{\text{real}|_{\text{phys}}}$ of Eq. (3.2.11) essentially becomes Ψ_{real} in Eq. (2.3.2), $\sqrt{(R_0 - R_a - 2R_b)/(R_0 + R_a)} \rightarrow 1$, and the $\Psi_{\text{imag}|_{\text{phys}}}^{\text{semi}}$ of Eq. (3.2.11) becomes the Ψ_{imag} in Eq. (2.3.2) because the detector located at (R_0, φ, z) reaches the imaginary semi-infinite boundary. This agrees with the physical aspect that an infinitely long convex cylindrical boundary becomes a semi-infinite boundary as the radius of the cylinder becomes infinity. By using the spherical coordinate expression of the photon fluence rate given in Eq. (2.2.1), we can rewrite Eq. (3.2.11) as

$$\Psi = \frac{S}{4\pi D} \frac{e^{-k_0 l_r}}{l_r} - \frac{S}{4\pi D} \frac{e^{-k_0 l_i}}{l_i} \sqrt{\frac{R_0 - R_a - 2R_b}{R_0 + R_a}}. \quad (3.2.12)$$

C. Summary of the Solutions in Cylindrical Coordinates

In cylindrical coordinates, the steady-state photon fluence rate in an infinite homogeneous medium is

$$\Psi = \frac{S}{2\pi^2 D} \int_0^\infty dk \cos[k(z-z')] \cdot \sum_{m=0}^\infty \epsilon_m I_m(k_{\text{eff}} \rho_{<}) K_m(k_{\text{eff}} \rho_{>}) \cos[m(\varphi - \varphi')]. \quad (3.3.1)$$

The steady-state photon fluence rate in a concave geometry imposed by an infinitely long circular cylindrical applicator for interrogating the medium internal to the applicator (e.g., breast imaging) is

$$\Psi = \frac{S}{2\pi^2 D} \int_0^\infty dk \left\{ \cos[k(z-z')] \cdot \sum_{m=0}^\infty \epsilon_m I_m[k_{\text{eff}}(R_0 - R_a)] K_m(k_{\text{eff}} R_0) \cdot \left\langle 1 - \frac{I_m(k_{\text{eff}} R_0) K_m[k_{\text{eff}}(R_0 + R_b)]}{K_m(k_{\text{eff}} R_0) I_m[k_{\text{eff}}(R_0 + R_b)]} \right\rangle \cos[m(\varphi - \varphi')] \right\}, \quad (3.3.2\text{conC})$$

where “conC” stands for “concave” and “conV” for “convex” (below).

The steady-state photon fluence rate in a convex geometry imposed by an infinitely long circular cylindrical applicator for interrogating the medium external to the applicator (e.g., prostate imaging) is

$$\Psi = \frac{S}{2\pi^2 D} \int_0^\infty dk \left\{ \cos[k(z-z')] \cdot \sum_{m=0}^\infty \epsilon_m I_m[k_{\text{eff}} R_0] K_m[k_{\text{eff}}(R_0 + R_a)] \cdot \left\langle 1 - \frac{K_m(k_{\text{eff}} R_0) I_m[k_{\text{eff}}(R_0 - R_b)]}{I_m(k_{\text{eff}} R_0) K_m[k_{\text{eff}}(R_0 - R_b)]} \right\rangle \cos[m(\varphi - \varphi')] \right\}. \quad (3.3.2\text{conV})$$

If the concave or convex geometry has a large radial dimension, the photon fluence rate expressed by Eqs. (3.3.2conC and 3.3.2conV) can be approximated to

$$\Psi = \frac{S}{4\pi D} \frac{e^{-k_0 l_r}}{l_r} - \frac{S}{4\pi D} \frac{e^{-k_0 l_i}}{l_i} \sqrt{\frac{R_0 + R_a + 2R_b}{R_0 - R_a}}, \quad (3.3.3\text{conC})$$

$$\Psi = \frac{S}{4\pi D} \frac{e^{-k_0 l_r}}{l_r} - \frac{S}{4\pi D} \frac{e^{-k_0 l_i}}{l_i} \sqrt{\frac{R_0 - R_a - 2R_b}{R_0 + R_a}}, \quad (3.3.3\text{conV})$$

where l_r is defined as the distance from the detector to the “real” isotropic source and l_i as the distance from the detector to the image source of the “real” isotropic source associated with the semi-infinite geometry that is tangential to the concave or convex geometry on the physical source point.

4. STEADY-STATE PHOTON DIFFUSION IN THE INFINITE GEOMETRY: NUMERICAL VERIFICATION OF THE CYLINDRICAL-COORDINATE SOLUTION

This section validates the cylindrical-coordinate solution (2.1.13) of the steady-state photon diffusion in a homogeneous infinite medium, since Eq. (2.1.13) sets the foundation for the analytic derivations thereafter. As evaluating entities like Eq. (2.1.13) involves half-sided integration and summation to infinity, the numerical approaches must provide sufficient accuracy within the framework imposed by the precision of the computer and the algorithm arithmetic.

For an infinite medium it is practical to define a source point arbitrarily at (0,0,0) and a field point at $(\rho, 0, 0)$. Then the spherical-coordinate solution (2.2.1) can be re-written as

$$\Psi = (S/4\pi D d) e^{-k_0 d}, \quad (4.1)$$

where d is the source–detector distance. Equation (4.1) can be implemented in terms of the linear relationship between $\ln(\Psi d)$ and d as indicated in Eq. (2.2.2). Similarly the cylindrical-coordinate solution (3.3.1) in the same homogeneous infinite medium becomes

$$\Psi(\rho, \varphi) = \frac{S}{2\pi^2 D} \int_0^\infty dk \sum_{m=0}^\infty \epsilon_m I_m(0) K_m(k_{\text{eff}} \rho_{>}). \quad (4.2)$$

The adaptive Gauss–Kronrod quadrature in MATLAB (Mathworks Inc, Natick, Massachusetts) is used to calculate the integrations in Eq. (4.2) as well as all the integrations appearing later. To effectively implement the integration and the infinite-summation terms in Eq. (4.2), it is necessary to evaluate the range for the integration or the summation to be executed. Based on the asymptotic expression of the modified Bessel functions for large argument [14], we have that for sufficiently large k , hence large k_{eff} ,

$$I(k_{\text{eff}} \rho_{<}) K(k_{\text{eff}} \rho_{>}) = \frac{1}{2k_{\text{eff}} \sqrt{\rho_{<} \rho_{>}}} e^{-k_{\text{eff}}(\rho_{>} - \rho_{<})}, \quad (4.3)$$

which asymptotically and quasi-exponentially reaches zero as k increases. Therefore for a given accuracy Eq. (4.2) can be numerically implemented with an upper limit of k , because it also sets the upper limit of the integration. The contributions of higher k to the integration in Eq. (4.2) are evaluated in Fig. 4(a) for the first m term of $m=0$ using realistic optical and geometry parameters, including $\mu_a = 0.01 \text{ cm}^{-1}$, $\mu'_s = 10 \text{ cm}^{-1}$, $\varphi = 0$, and $d = 0.5\text{--}10 \text{ cm}$. The use of $\ln(\Psi d)$ versus d is necessary for evaluating Eq. (4.2) with respect to Eq. (4.1). The difference of setting the upper limit of k at 50 or 100 is indistinguishable for a source–detector distance greater than 1 mm, at the scale shown. The integration in Eq. (4.2) is therefore executed for $k=50$, as the source–detector distance practically is much greater than 1 mm.

To evaluate the choice of m , we first check the following terms in Eq. (4.2) and denote them Ω :

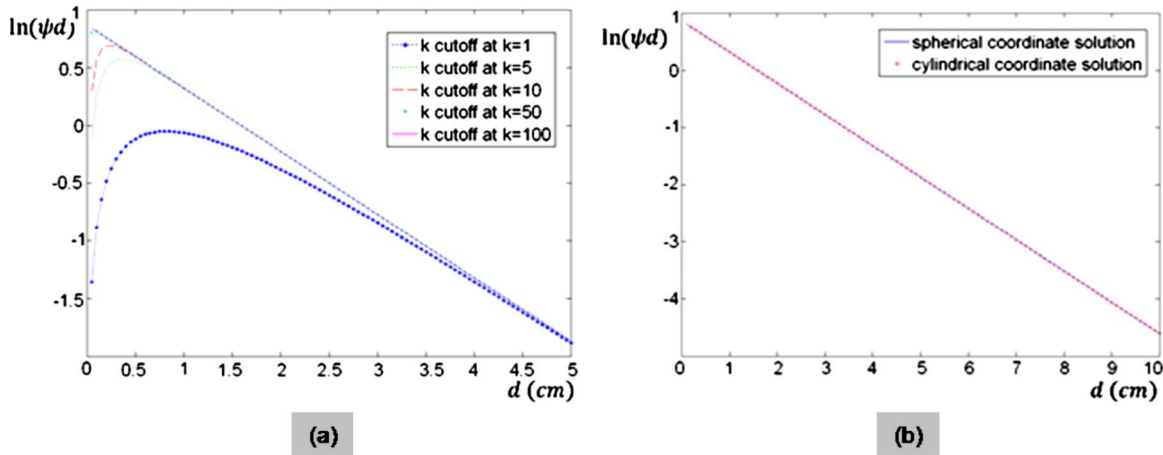


Fig. 4. (Color online) (a) Comparison of the contributions of the k terms when evaluating the cylindrical-coordinate solution to the steady-state photon diffusion in the homogeneous infinite medium. (b) Comparison between the solutions in spherical coordinates and cylindrical coordinates to the steady-state photon diffusion in the homogeneous infinite medium.

$$\Omega = \sum_{m=0}^{\infty} \epsilon_m I_m(0) K_m(k_{\text{eff}} \rho). \quad (4.4)$$

In Eq. (4.4), $I_m(0)$ will be nonzero only when $m=0$. Hence, only the first m term need be summed. Overall, Eq. (4.2) can be evaluated by integrating up to $k=50$ and summing the first m terms.

Figure 4(b) evaluates Eq. (4.2) with respect to Eq. (4.1) for the parameters of $\mu_a=0.01 \text{ cm}^{-1}$, $\mu'_s=10 \text{ cm}^{-1}$, $\varphi=0$, and $\rho=0.5\text{--}10 \text{ cm}$ as in Fig. 4(a), and integrating k up to 100 for $m=0$. Figure 4(b) demonstrates that Eq. (4.2) is identical to Eq. (4.1) within the precision of the MATLAB arithmetic.

5. STEADY-STATE PHOTON DIFFUSION IN THE “CONCAVE” AND “CONVEX” GEOMETRIES: NUMERICAL EVALUATION OF THE CYLINDRICAL-COORDINATE SOLUTIONS

This section numerically evaluates the general solutions in Eq. (3.3.2) for geometries having smaller cylinder radius and their approximations in Eq. (3.3.3) for geometries having very large cylinder radius. These evaluations, for simplicity, are limited to two cases: (1) the source and detector are located at the same azimuth plane; (2) the source and detector are located longitudinally with the same azimuthal angle. The results will indicate how the circular boundary affects the photon fluence rate with respect to a semi-infinite boundary, and justify qualitatively these analytic solutions and their approximations.

A. Specific Geometry: Source and Detector Located at the Same Azimuth Plane

The geometries shown in Fig. 5 are chosen to study the effect of concave or convex boundary shape on photon diffusion for the source and detector located at the same azimuth plane. Then the “chord” distance between the source and the detector is considered in a range from 0.5 cm (assuring diffusion treatment) to $2R_0$ for optical

properties set at $\mu_a=0.01 \text{ cm}^{-1}$, $\mu'_s=10 \text{ cm}^{-1}$, $A=1$, and $S=1$ (these parameters are used throughout the rest of the studies).

1. Numerical Approaches

In this case, both the source and detector are on the same azimuthal plane, that is $z=z'$; therefore Eqs. (3.3.2conC and 3.3.2conV) can be rewritten as

$$\Psi = \frac{S}{2\pi^2 D} \int_0^\infty dk \left\{ \sum_{m=0}^{\infty} \epsilon_m I_m[k_{\text{eff}}(R_0 - R_a)] K_m(k_{\text{eff}} R_0) \cdot \left\langle 1 - \frac{I_m(k_{\text{eff}} R_0)}{K_m(k_{\text{eff}} R_0)} \frac{K_m[k_{\text{eff}}(R_0 + R_b)]}{I_m[k_{\text{eff}}(R_0 + R_b)]} \right\rangle \cos[m(\varphi - \varphi')] \right\}, \quad (5.1.1\text{conC})$$

$$\Psi = \frac{S}{2\pi^2 D} \int_0^\infty dk \left\{ \sum_{m=0}^{\infty} \epsilon_m I_m(k_{\text{eff}} R_0) K_m[k_{\text{eff}}(R_0 + R_a)] \cdot \left\langle 1 - \frac{K_m(k_{\text{eff}} R_0)}{I_m(k_{\text{eff}} R_0)} \frac{I_m[k_{\text{eff}}(R_0 - R_b)]}{K_m[k_{\text{eff}}(R_0 - R_b)]} \right\rangle \cos[m(\varphi - \varphi')] \right\}. \quad (5.1.1\text{conV})$$

For large k , hence large k_{eff} , the integrands of Eqs. (5.1.1conC and 5.1.1conV) become the following [14]:

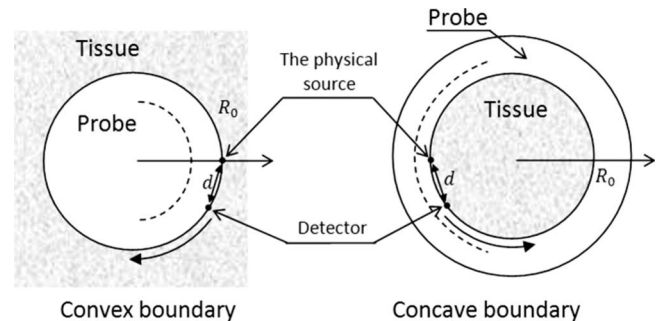


Fig. 5. Concave and convex geometries with the source and the detector located at the same azimuthal plane.

$$\begin{aligned}
& I_m[k_{\text{eff}}(R_0 - R_a)]K_m(k_{\text{eff}}R_0) \\
& \times \left\langle 1 - \frac{I_m(k_{\text{eff}}R_0) K_m[k_{\text{eff}}(R_0 + R_b)]}{K_m(k_{\text{eff}}R_0) I_m[k_{\text{eff}}(R_0 + R_b)]} \right\rangle \\
& = \frac{e^{-k_{\text{eff}}R_a}}{2k_{\text{eff}}\sqrt{R_0(R_0 - R_a)}}(1 - e^{-2k_{\text{eff}}R_b}), \quad (5.1.2\text{conC})
\end{aligned}$$

$$\begin{aligned}
& I_m(k_{\text{eff}}R_0)K_m[k_{\text{eff}}(R_0 + R_a)] \\
& \times \left\langle 1 - \frac{K_m(k_{\text{eff}}R_0) I_m[k_{\text{eff}}(R_0 - R_b)]}{I_m(k_{\text{eff}}R_0) K_m[k_{\text{eff}}(R_0 - R_b)]} \right\rangle \\
& = \frac{e^{-k_{\text{eff}}R_a}}{2k_{\text{eff}}\sqrt{R_0(R_0 + R_a)}}(1 - e^{-2k_{\text{eff}}R_b}). \quad (5.1.2\text{conV})
\end{aligned}$$

It is again noted that as k_{eff} becomes sufficiently large both Eqs. (5.1.2conC and 5.1.2conV) asymptotically and quasi-exponentially approach zero. Therefore in Eqs. (5.1.1conC and 5.1.1conV) the contribution of the integrands associated with k greater than a certain limit can be neglected. However, according to the IEEE standard for floating-point arithmetic [19], there is a limit for the largest number and the smallest number to be stored. In MATLAB the criterion [20] for overflow is 1.7977×10^{308} in decimal, and for underflow is 2.2251×10^{-308} . In Eqs. (5.1.1conC and 5.1.1conV), the modified Bessel functions of the first and second kinds are exponentially growing and decaying functions, for which overflow will readily occur for a large order m and underflow for a large argument k . To evaluate source and detector at the same azimuthal plane a larger order of m is necessary, and to evaluate the source and detector located longitudinally with the same azimuthal angle a large argument k also becomes crucial. In both Eqs. (5.1.1conC and 5.1.1conV), since all the modified Bessel functions of the first and second kinds appear in pairs in the same order when multiplying with each other, a strategy of “pre-enlarge” and “pre-reduce” is implemented to ease the numerical manipulation. The principle is that instead of evaluating each modified Bessel function individually, the modified Bessel function of the first kind can be “pre-reduced” for large order m and the modified Bessel function of the sec-

ond kind can be “pre-enlarged” by the same degree, by which the product of each pair will remain unchanged. The outcome of this pre-enlarge and pre-reduce manipulation is demonstrated in Fig. 6(a) for a convex boundary of $R_0=2$ cm, d changing from 0.1 cm to 4 cm, k cutoff at 70, $\mu_a=0.01$ cm⁻¹, $\mu'_s=10$ cm⁻¹, $A=1$, and $S=1$. The m is summed from 0 to 150 (the dotted curve with ripples), which was the limit to avoid overflow and underflow without applying the pre-enlarge and pre-reduce approach. After pre-enlarge and pre-reduce, the summation can be made for m up to 500. Figure 6(a) indicates that this method of pre-enlarge and pre-reduce enables summing modified Bessel functions up to a large order of m by eliminating the ripples or noise seen when no such manipulation is employed.

Additionally, it is also found for Eqs. (5.1.1conC and 5.1.1conV) that the radius R_0 has a great effect on the evaluation outcome. For instance, when R_0 is as large as 8 cm in Eq. (5.1.1conC), for $k=40$, the integration does not converge sufficiently even for summing m up to 500 [the optical parameters are the same as used for Fig. 6(a)], but for a smaller radius $R_0=1$ cm the same integrand converges quickly at $m=100$. A method of “repeated averaging” is thus employed to improve the convergence. The principle is to first examine if there is an oscillating pattern. If there is, the envelope of the maxima and minima of the oscillation is implemented to form a finite converging alternative series, and the last maxima and minima are averaged to become the value of the integrand. If an oscillating pattern is not formed, the last result is chosen as the value of the integrand. The results of applying such “repeated averaging” when evaluating Eq. (5.1.1conC) are shown in Fig. 6(b), in which m is summed up to 540 for $R_0=8$ cm.

Based on these specific approaches of improving the outcome of numerical evaluations, the upper limits of k and m are evaluated individually for each set of computations conducted. For example, at a parameter setting of m terms up to 150, the effects of a finite k cutoff value when evaluating Eq. (5.1.1) are shown in Fig. 7(a) for the concave boundary and Fig. 7(b) for the convex boundary. The difference between integrating k from 0 to 50 and from 0 to 100 is indistinguishable at the given scale, for both con-

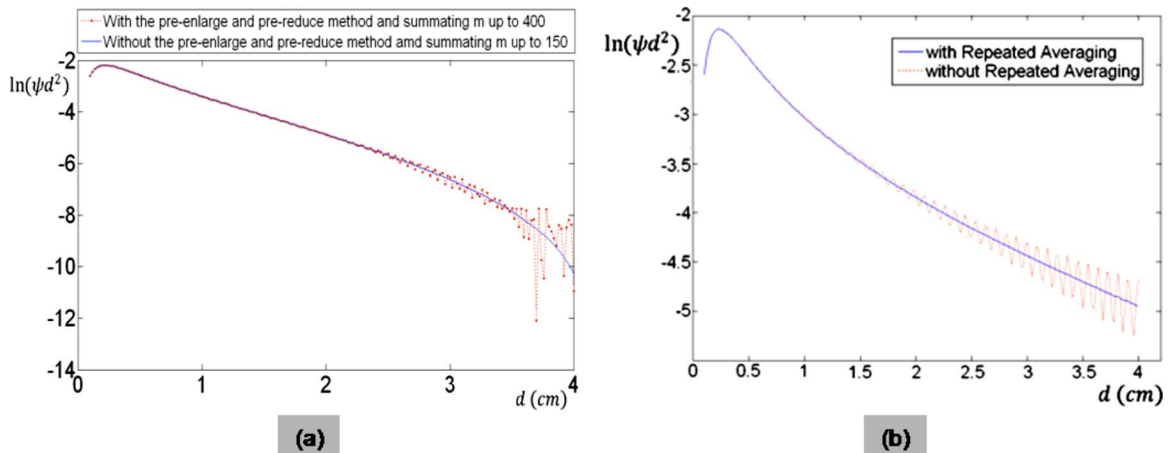


Fig. 6. (Color online) (a) Outcome of applying pre-enlarge and pre-reduce methods for $R_0=2$ cm in convex geometry. (b) Outcome of applying “repeated averaging” for $R_0=8$ cm in concave geometry.

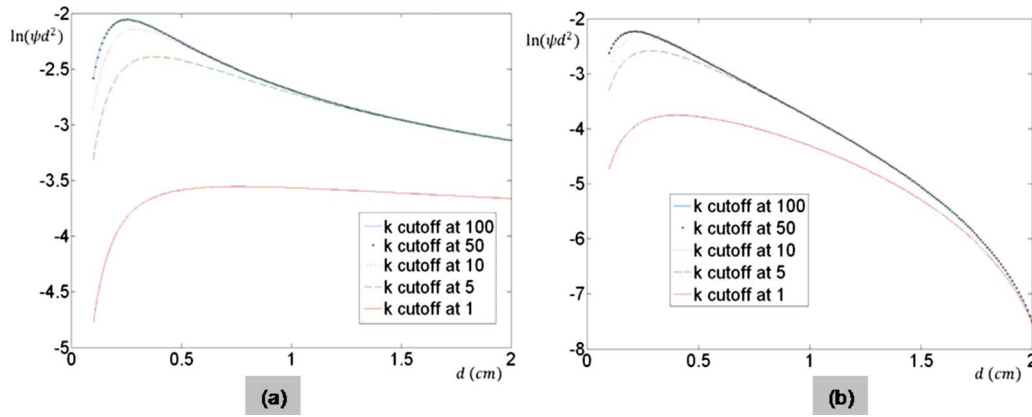


Fig. 7. (Color online) Comparison of the contributions of k terms in the solution for source and detector located in the same azimuthal plane: (a) concave geometry; (b) convex geometry.

cave and convex boundaries. Therefore the cutoff value for k is set at 50 for this set of evaluations.

2. Numerical Evaluation of the General Solutions for a Cylinder Applicator of Radius up to 10 Cm

The general solutions (5.1.1conC and 5.1.1conV) are evaluated numerically with respect to a semi-infinite geometry in Fig. 8(a). The radius R_0 is chosen as 0.5, 1, 2, 5,

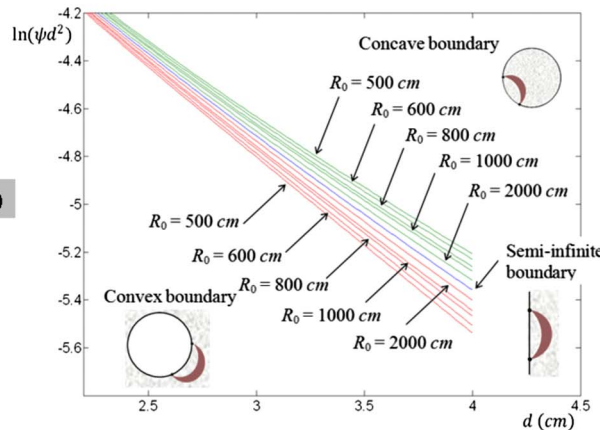
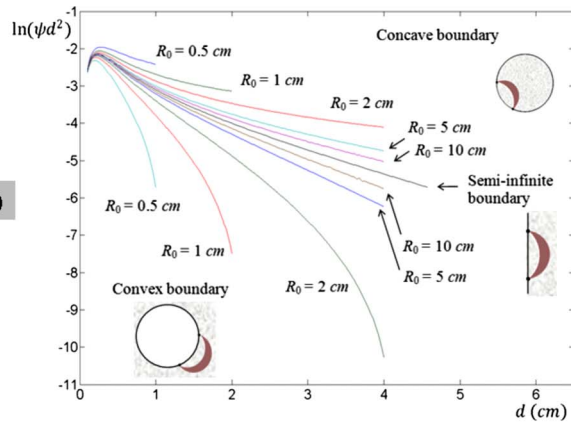


Fig. 8. (Color online) (a) Comparison of the solutions for concave and convex geometries with respect to the semi-infinite geometry, for source and detector located at the same azimuthal plane. (b) Comparison of the solutions for concave and convex geometries having large cylinder radius with respect to the semi-infinite geometry for source and detector located at the same azimuthal plane.

and 10 cm. The figure is plotted for $\ln(\Psi d^2)$ versus d as this is the linear relationship implied by Eq. (2.3.5) of semi-infinite geometry. It is noted again that d is assigned as the chord distance between the physical source and the detector points on the circular boundary. Therefore the maximum d for a radius of 0.5 cm is 1 cm, of 1 cm is 2 cm, etc., and d is set to change from 0.1 to 4 cm for the remaining radii. On the azimuthal plane, the photon fluence rate associated with a given source–detector distance in a concave geometry is greater than that in a planar geometry for the same source–detector distance, and in a convex geometry it is smaller than that in a planar geometry. The overall qualitative feature, as anticipated, is that as the radius of the cylinder geometry increases, the photon fluence rate for the concave and convex boundaries asymptotically approaches that for a semi-infinite boundary.

3. Numerical Evaluation of the Solutions Approximated for a Cylindrical Applicator of Very Large Radius

For the azimuthal geometry with large cylinder diameter, the distance terms in Eqs. (3.3.3conC and 3.3.3conV) can be expressed by

$$l_r = [R_a^2 + d^2 - (R_a d^2 / R_0)]^{1/2}, \quad (5.1.4conC)$$

$$l_i = [(R_a + 2R_b)^2 + d^2 + (R_a + 2R_b)(d^2 / R_0)]^{1/2} \quad (5.1.5conC)$$

for concave boundary, and

$$l_r = [R_a^2 + d^2 + (R_a d^2 / R_0)]^{1/2}, \quad (5.1.4conV)$$

$$l_i = [(R_a + 2R_b)^2 + d^2 - (R_a + 2R_b)(d^2 / R_0)]^{1/2} \quad (5.1.5conV)$$

for convex boundary. The comparison of the two azimuthal geometries with respect to the semi-infinite geometry is given in Fig. 8(b), where the radius R_0 is chosen as 500, 600, 800, 1000, and 2000 cm. The results are shown only for d from 2.2 to 4 cm to illustrate that both the concave and convex boundary asymptotically approach the “linear” feature of the planar boundary for $\ln(\psi d^2)$ and d , but with radius-dependent differences in the slope and

potentially in the intersection, both of which clearly will vanish as the radius becomes infinity.

B. Specific Geometry: Source and Detector Located Longitudinally with the Same Azimuthal Angle

The geometries shown in Fig. 9 are chosen to study the effect of concave or convex shape on photon diffusion for the source and detector located longitudinally with the same azimuthal angle.

1. Numerical Approaches

For $\varphi = \varphi'$, we rewrite Eqs. (3.3.2conC and 3.3.2conV) as

$$\Psi = \frac{S}{2\pi^2 D} \int_0^\infty dk \left\{ \cos[k(z - z')] \cdot \sum_{m=0}^\infty \epsilon_m I_m[k_{\text{eff}}(R_0 - R_a)] K_m(k_{\text{eff}} R_0) \cdot \left\langle 1 - \frac{I_m(k_{\text{eff}} R_0)}{K_m(k_{\text{eff}} R_0)} \frac{K_m[k_{\text{eff}}(R_0 + R_b)]}{I_m[k_{\text{eff}}(R_0 + R_b)]} \right\rangle \right\}, \quad (5.2.1\text{conC})$$

$$\Psi = \frac{S}{2\pi^2 D} \int_0^\infty dk \left\{ \cos[k(z - z')] \cdot \sum_{m=0}^\infty \epsilon_m I_m(k_{\text{eff}} R_0) K_m[k_{\text{eff}}(R_0 + R_a)] \cdot \left\langle 1 - \frac{K_m(k_{\text{eff}} R_0)}{I_m(k_{\text{eff}} R_0)} \frac{I_m[k_{\text{eff}}(R_0 - R_b)]}{K_m[k_{\text{eff}}(R_0 - R_b)]} \right\rangle \right\}. \quad (5.2.1\text{conV})$$

The previous analysis given for numerical evaluation of Eqs. (5.1.2conC and 5.1.2conV) still holds here; therefore the contribution due to large k , hence large k_{eff} , is neglected.

The numerical manipulation methods of pre-enlarge and pre-reduce as well as repeated averaging discussed in Subsection 5.A are also applied here. The settings of k values are shown in Fig. 10(a) for concave boundary and Fig. 10(b) for convex boundary, where the parameters used are $R_0 = 1$ cm with d ranging from 0.5 cm to 2 cm and m summing from 0 to 100. It is observed that the plots for k cutoff at 100 and 200 are indistinguishable at

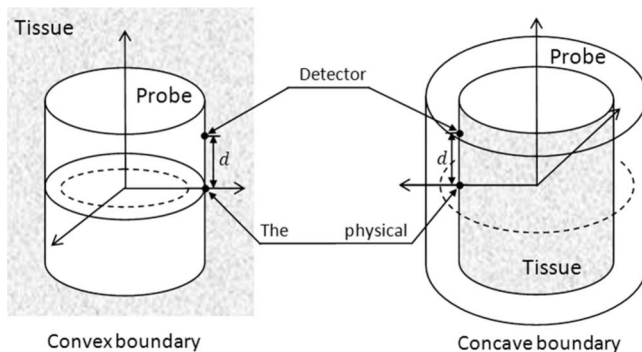


Fig. 9. Concave and convex geometries with source and detector located longitudinally with the same azimuthal angle.

the given scale. For this set of computations the upper limit for k is then set at 100. This upper limit of k is higher than that used for evaluating the azimuthal plane. It is also found that the upper limit for m can be chosen much lower than that used for evaluating the azimuthal plane. Again the upper limits of k and m are evaluated individually for each set of computations.

2. Numerical Evaluation of the General Solutions for a Cylindrical Applicator of Radius up to 6 Cm

The general solutions (5.2.1conC and 5.2.1conV) are evaluated numerically with respect to semi-infinite geometry in Fig. 11(a). The radius R_0 is chosen as 1, 2, 3, and 6 cm. The figure is again plotted for $\ln(\Psi d^2)$ versus d , as it is the linear relationship implied by Eq. (2.3.5) for a semi-infinite geometry, and d is the longitudinal distance between the physical source and the detector points on the circular boundary. The d in this geometry is not limited in range, but a range from 0.1 to 4 cm is chosen for comparison with the azimuthal geometry of Fig. 8. Along the longitudinal direction, the photon fluence rate associated with a given source–detector distance in a concave geometry is smaller than that in a planar geometry for the same source–detector distance, and in a convex geometry it is greater than that in a planar geometry. The overall qualitative feature, as anticipated, is that as the radius of the cylinder geometry increases, the photon fluence rate for the concave and convex boundaries asymptotically approaches that for a semi-infinite geometry.

3. Numerical Evaluation of the Solutions for a Cylinder Applicator of Very Large Radius

For the longitudinal geometry with larger cylinder diameter, the distance terms in Eqs. (3.3.3conC and 3.3.3conV) can be expressed by

$$l_r = (R_a^2 + d^2)^{1/2}, \quad (5.2.2)$$

$$l_i = [(R_a + 2R_b)^2 + d^2]^{1/2} \quad (5.2.3)$$

for both concave and convex geometries. The comparison of the two longitudinal geometries with respect to the semi-infinite geometry is given in Fig. 11(b) with the rest of the parameters the same as in Fig. 8(b). Again, both the concave and convex geometry asymptotically approach the “linear” feature of the planar boundary for $\ln(\Psi d^2)$ and d , but with radius-dependent differences in the slope and potentially in the intersection, both of which clearly will vanish as the radius becomes infinity.

Finally in terms of the computation time, for each single curve in Fig. 8 or Fig. 11 that includes on average 300 data points, it takes approximately 5 min to formulate on a 2.8 GHz CPU with 1.0 GB of memory.

6. DISCUSSION

The solution to photon diffusion in an infinite homogeneous medium derived in cylindrical coordinates likely will involve two Bessel functions. The solution could have different expressions, depending on the type (normal or modified, the first kind, or the second kind) of Bessel functions used and the way these functions are integrated into

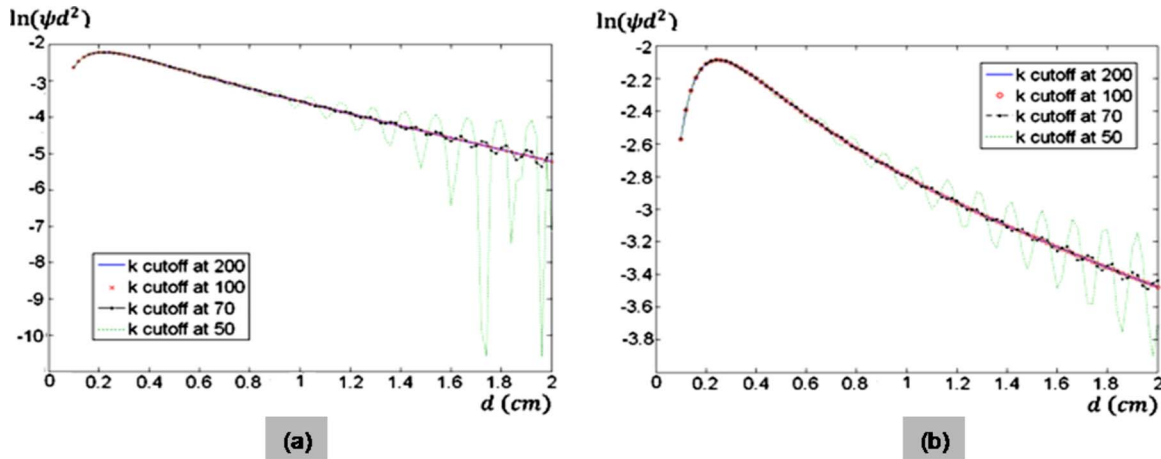


Fig. 10. (Color online) Comparison of the contributions of k terms in the solution for source and detector located longitudinally with the same azimuthal angle: (a) concave boundary; (b) convex boundary.

the solution. In Eq. (3.3.1), we have expressed the solution using the modified Bessel functions. The integration part of Eq. (3.3.1) is identical to that of the solution to the Poisson equation in cylindrical coordinates given in [13], except that the argument contains k_{eff} instead of k as in

[13]. This solution may be advantageous as it demonstrates clearly the different roles of the source and the field points in the solution by differentiating the radial coordinates of the source and field points into the arguments specific to different kinds of the modified Bessel functions, such that both of the modified Bessel functions will become valid in the geometry of interest.

Applying the solution in Eq. (3.3.1) leads to physically explicit interpretation in the two equations of (3.3.2) for a medium involving an external or internal cylindrical boundary. These equations in (3.3.2) are composed of two parts in the curly brackets: the first part is associated with the “real” isotropic source, and the second part is the contribution of the “image” source term that is represented by the “real” source term scaled by a factor. The scaling factor is related to the radius of the cylinder and the reflective index mismatch of the cylinder–medium interface that determines where the extrapolated boundary will be placed. The equations in (3.3.3), which are derived for large-radius concave and convex boundaries, are given in a format similar to that for semi-infinite geometry but with a shape-curvature-associated term that approaches unity as the radius of the cylinder approaches infinity.

The numerical evaluations in Section 5 demonstrate the qualitative correctness of the analytic solutions in Eqs. (3.3.2) for the two circular cylindrical geometries, within the limits of the current computer arithmetic. It is clearly shown that the solutions given in the two Eqs. (3.3.2) asymptotically approach the semi-infinite medium solution as the applicator radius reaches infinity. For the specific case of having the source and detector located azimuthally on the same axial plane, the photon fluence rate is greater than the semi-infinite geometry for the concave boundary and smaller for the convex boundary given the same source–detector distance. This can be explained by noting that, for the same source–detector distance, more near-field photons from the source could scatter and reach the detector in the concave geometry than in the semi-infinite geometry, but in the convex geometry they do the opposite. For the specific case of having the source and detector located longitudinally on the same azimuthal angle, the photon fluence rate is smaller than the semi-infinite geometry for the concave boundary and greater

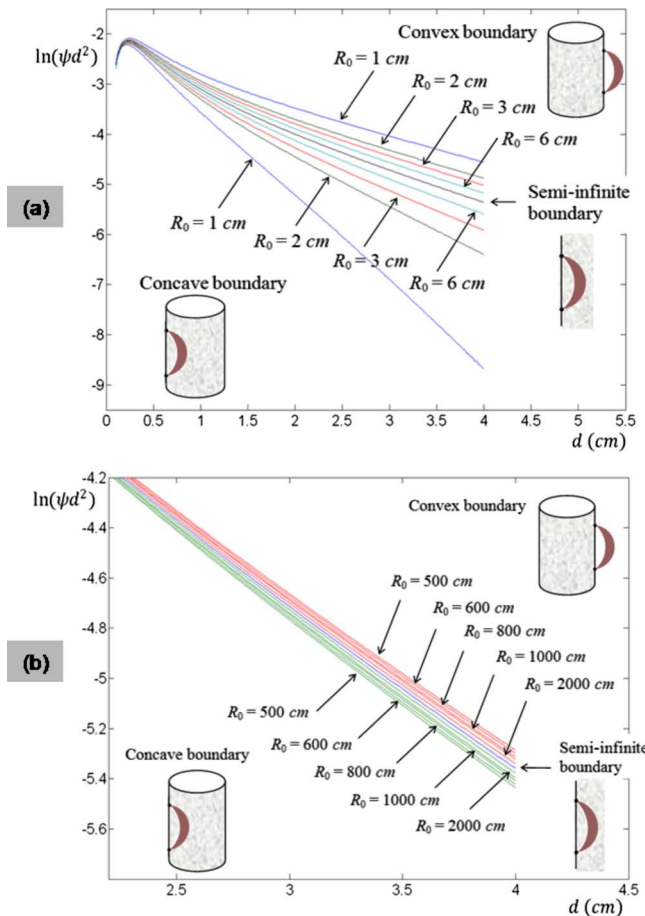


Fig. 11. (Color online) (a) Comparison of the solutions for concave and convex geometries with respect to the semi-infinite geometry for source and detector located longitudinally with the same azimuthal angle. (b) Comparison of the solutions for concave and convex geometries having large cylinder diameter with respect to the semi-infinite geometry for source and detector located longitudinally with the same azimuthal angle.

for the convex boundary given the same source–detector distance. This again can be explained by noting that, for the same source–detector distance, fewer near-field photons from the source could scatter and reach the detector in the concave geometry than in the semi-infinite geometry, but in the convex geometry the opposite is true.

7. CONCLUSIONS

The steady-state photon diffusion in a homogeneous medium bounded externally or internally by an infinitely long circular cylindrical applicator has been analyzed. The geometry of a diffusive medium bounded externally by a cylindrical applicator resembles that of imaging externally accessible biological tissue such as the breast using a ring-type array. The geometry of a diffusive medium bounded internally by a cylindrical applicator resembles that of imaging internally accessible biological tissue such as the prostate using a trans-rectal probe. Solutions to steady-state photon diffusion in these two geometries are derived in cylindrical coordinates by applying the extrapolated boundary condition and are expressed in modified Bessel functions of the first and second kinds. Approximate solutions for large cylinder radius are also derived in the format close to that for semi-infinite geometry by including a shape-radius-associated term. Numerical evaluations are provided for the cases of having the source and the detector positioned only along the azimuthal or longitudinal directions. The results demonstrate that compared with a semi-infinite boundary, the concave boundary has smaller photon fluence decay in the azimuth direction but greater photon fluence decay along the longitudinal direction compared with a semi-infinite geometry having the same source–detector distance. On the other hand, the convex boundary has greater photon fluence decay in the azimuth direction but smaller photon fluence decay along the longitudinal direction. As the radius of the concave or convex circular applicator becomes infinitely large, the results for these specific geometries reach the well-known condition for a semi-infinite medium, as expected. This theory and “qualitative” numerical evaluation constitute the first part of this work, which will be quantitatively examined in the second part and potentially extended to time-resolved analysis in future studies.

APPENDIX A: SOLUTION TO EQ. (2.1.10) FOLLOWING JACKSON’S APPROACH IN [13]

Equation (2.1.10) is rewritten here:

$$\frac{1}{\rho} \frac{\partial}{\partial \rho} \left(\rho \frac{\partial g_m(k, \rho, \rho')}{\partial \rho} \right) - \left(k_{\text{eff}}^2 + \frac{m^2}{\rho^2} \right) g_m(k, \rho, \rho') = -\frac{1}{\rho} \delta(\rho - \rho'). \quad (\text{A.1})$$

For $\rho \neq \rho'$, Eq. (A.1) is the equation for the modified Bessel functions $I_m(k_{\text{eff}}\rho)$ and $K_m(k_{\text{eff}}\rho)$. According to Jackson [13], assume that $\psi_1(k_{\text{eff}}\rho)$ is some linear combination of I_m and K_m satisfying the boundary conditions for $\rho < \rho'$, and $\psi_2(k_{\text{eff}}\rho)$ is a linearly independent combination of I_m and K_m satisfying the boundary conditions for $\rho > \rho'$; then

the symmetry of the Green’s function in ρ and ρ' requires that

$$g_m(k, \rho, \rho') = \psi_1(k_{\text{eff}}\rho_{<})\psi_2(k_{\text{eff}}\rho_{>}), \quad (\text{A.2})$$

where $\rho_{<}$ and $\rho_{>}$ indicate the smaller and larger radial coordinates of the source and the detector.

The normalization of the product $\psi_1(k_{\text{eff}}\rho_{<}) \cdot \psi_2(k_{\text{eff}}\rho_{>})$ requires that $g_m(k, \rho, \rho')$ satisfy the discontinuity in slope implied by the delta function in Eq. (A.1):

$$\left. \frac{dg_m}{d\rho} \right|_+ - \left. \frac{dg_m}{d\rho} \right|_- = -\frac{1}{\rho'}, \quad (\text{A.3})$$

where $|_{\pm}$ means “evaluated at $\rho = \rho' \pm \epsilon$.” Then we have

$$\left. \frac{dg_m}{d\rho} \right|_+ - \left. \frac{dg_m}{d\rho} \right|_- = k_{\text{eff}}(\psi_1\psi_2' - \psi_2\psi_1') = k_{\text{eff}}W[\psi_1, \psi_2], \quad (\text{A.4})$$

where $W[\psi_1, \psi_2]$ is the Wronskian of ψ_1 and ψ_2 . Equation (A.1) is of the Sturm–Liouville type

$$\frac{d}{dx} \left[p(x) \frac{dy}{dx} \right] + g(x)y = 0, \quad (\text{A.5})$$

and it is known that the Wronskian of two linearly independent solutions of such an equation is proportional to $[1/p(x)]$. Hence the possibility of $g_m(k, \rho, \rho')$ satisfying Eq. (A.3) for all values of ρ' is assured, so it requires that the Wronskian has the value

$$W[\psi_1(x), \psi_2(x)] = -\frac{1}{x}, \quad (\text{A.6})$$

which normalizes $\psi_1(k_{\text{eff}}\rho_{<}) \cdot \psi_2(k_{\text{eff}}\rho_{>})$. If there is no boundary surface, $g_m(k, \rho, \rho')$ must be finite at $\rho=0$ and vanish at $\rho \rightarrow \infty$. Consequently we can define

$$\psi_1(k_{\text{eff}}\rho_{<}) = \Omega I_m(k_{\text{eff}}\rho_{<}) \quad \text{and} \quad \psi_2(k_{\text{eff}}\rho_{>}) = K_m(k_{\text{eff}}\rho_{>}), \quad (\text{A.7})$$

where the constant Ω is to be determined from the normalization requirement of Eq. (A.6). Substituting Eq. (A.7) into Eq. (A.6) by changing the argument $k_{\text{eff}}\rho \rightarrow x$ we have

$$\Omega \cdot W[I_m(x), K_m(x)] = -\frac{1}{x}, \quad (\text{A.8})$$

which can be evaluated at any value of x . Based on the asymptotic expressions for the modified Bessel functions [14], we have for either small x or large x

$$W[I_m(x), K_m(x)] = -\frac{1}{x}, \quad (\text{A.9})$$

which leads to $\Omega=1$ in Eq. (A.8); thereby Eq. (A.2) changes to

$$g_m(k, \rho, \rho') = I_m(k_{\text{eff}}\rho_{<})K_m(k_{\text{eff}}\rho_{>}). \quad (\text{A.10})$$

Substituting Eq. (A.10) into Eq. (2.1.7) gives the Green’s function of Eq. (2.1.3) in cylindrical coordinates as

$$G(\vec{r}, \vec{r}') = \frac{1}{2\pi^2} \sum_{m=-\infty}^{\infty} \int_0^{\infty} dk e^{im(\varphi - \varphi')} \times [I_m(k_{\text{eff}}\rho_{<})K_m(k_{\text{eff}}\rho_{>})] \cdot \cos[k(z - z')]. \quad (\text{A.11})$$

Writing in terms of the real function:

$$G(\vec{r}, \vec{r}') = \frac{1}{2\pi^2} \int_0^{\infty} dk \cdot \left\{ \sum_{m=0}^{\infty} \epsilon_m I_m(k_{\text{eff}}\rho_{<})K_m(k_{\text{eff}}\rho_{>}) \times \cos[m(\varphi - \varphi')] \right\} \cdot \cos[k(z - z')], \quad (\text{A.12})$$

$$\text{where } \epsilon_m = \begin{cases} 2, & m \neq 0 \\ 1, & m = 0 \end{cases}. \quad (\text{A.13})$$

ACKNOWLEDGMENTS

This work has been supported in part by a research grant HR06-171 from the Oklahoma Center for the Advancement of Science and Technology (OCAST), a Big-XII faculty fellowship awarded to Daqing Piao, and the Prostate Cancer Research Program of the Department of Defense through grant #W81XWH-07-1-0247. We also thank Prof. Gang Yao in the University of Missouri, Columbia, for insightful comments.

REFERENCES

1. A. Ishimaru, "Diffusion of light in turbid material," *Appl. Opt.* **28**, 2210–2215 (1989).
2. S. Fantini, M. A. Franceschini, and E. Gratton, "Semi-infinite-geometry boundary problem for light migration in highly scattering media: a frequency-domain study in the diffusion approximation," *J. Opt. Soc. Am. B* **11**, 2128–2138 (1994).
3. S. Srinivasan, B. W. Pogue, C. Carpenter, S. Jiang, W. A. Wells, S. P. Poplack, P. A. Kaufman, and K. D. Paulsen, "Developments in quantitative oxygen-saturation imaging of breast tissue in vivo using multispectral near-infrared tomography," *Antioxid. Redox. Signal.* **9**, 1143–1156 (2007) (review).
4. S. R. Arridge, M. Cope, and D. T. Delpy, "The theoretical basis for the determination of optical pathlengths in tissue: temporal and frequency analysis," *Phys. Med. Biol.* **37**, 1531–1560 (1992).
5. R. C. Haskell, L. O. Svaasand, T. Tsay, T. Feng, M. S. McAdams, and B. J. Tromberg, "Boundary conditions for the diffusion equation in radiative transfer," *J. Opt. Soc. Am. A* **11**, 2727–2741 (1994).
6. D. Contini, F. Martelli, and G. Zaccanti, "Photon migration through a turbid slab described by a model based on diffusion approximation. I. Theory," *Appl. Opt.* **36**, 4587–4599 (1997).
7. B. W. Pogue and M. S. Patterson, "Frequency-domain optical absorption spectroscopy of finite tissue volumes using diffusion theory," *Phys. Med. Biol.* **39**, 1157–1180 (1994).
8. A. Sassaroli, F. Martelli, G. Zaccanti, and Y. Yamada, "Performance of fitting procedures in curved geometry for retrieval of the optical properties of tissue from time-resolved measurements," *Appl. Opt.* **40**, 185–197 (2001).
9. D. Piao, H. Xie, W. Zhang, J. S. Kransinski, G. Zhang, H. Dehghani, and B. W. Pogue, "Endoscopic, rapid near-infrared optical tomography," *Opt. Lett.* **31**, 2876–2878 (2006).
10. D. Piao, Z. Jiang, K. E. Bartels, G. R. Holyoak, J. W. Ritchey, G. Xu, C. F. Bunting, and G. Slobodov, "In vivo trans-rectal ultrasound-coupled near-infrared optical tomography of intact normal canine prostate," *J. Innovative Opt. Health Sciences* **2**, 215–225 (2009).
11. C. Li, R. Liengsawangwong, H. Choi, and R. Cheung, "Using a priori structural information from magnetic resonance imaging to investigate the feasibility of prostate diffuse optical tomography and spectroscopy: a simulation study," *Med. Phys.* **34**, 266–274 (2007).
12. J. Boutet, L. Herve, M. Debourdeau, L. Guyon, P. Peltie, J.-M. Dinten, L. Saroul, F. Duboeuf, and D. Vray, "Bimodal ultrasound and fluorescence approach for prostate cancer diagnosis," *J. Biomed. Opt.* **14**, 064001 (2009).
13. J. D. Jackson, "Expansion of Green functions in cylindrical coordinates," in *Classical Electrodynamics*, 3rd ed. (Wiley, 1998), pp. 125–126.
14. G. B. Arfken and H. J. Weber, *Mathematical Methods for Physicists*, 6th ed. (Harcourt, 2005).
15. L. V. Wang and H. Wu, *Biomedical Optics, Principles and Imaging* (Wiley, 2007).
16. K. S. Fine and C. F. Driscoll, "The finite length diocotron mode," *Phys. Plasmas* **5**, 601–607 (1998).
17. V. Ntziachristos, "Concurrent diffuse optical tomography, spectroscopy and magnetic resonance imaging of breast cancer," Ph.D. dissertation (University of Pennsylvania, Philadelphia, Pennsylvania, 2000).
18. S. T. Cui, "Electrostatic potential in cylindrical dielectric media using the image charge method," *Mol. Phys.* **104**, 2993–3001 (2006).
19. IEEE 754-2008 Standard for Floating-Point Arithmetic (IEEE, 2008).
20. C. Moler, "Floating points: IEEE standard unifies arithmetic model," Cleve's Corner, The MathWorks, Inc., 1996.

Alternative Transrectal Prostate Imaging: A Diffuse Optical Tomography Method

Daqing Piao, *Member, IEEE*, Kenneth E. Bartels, Zhen Jiang, Gilbert Reed Holyoak, Jerry W. Ritchey, Guan Xu, Charles F. Bunting, *Member, IEEE*, and Gennady Slobodov

Abstract—This paper presents a transrectal dual-modality near-infrared (NIR) diffuse optical tomography technique coupled with ultrasonography that provides an integrated method for detecting prostate cancer (PCa). The study that provides an alternative transrectal prostate imaging system stems from the perceived inadequacy of conventional transrectal ultrasound (TRUS) in PCa imaging. The transrectally applied diffuse optical tomography aims to characterize the spatially resolved optical properties of the intact prostate that are known to have intraorgan and intersubject heterogeneities. A canine model of PCa using canine transmissible venereal tumor was used to demonstrate the utility of this technology in detecting PCa. Tumors in the pelvic canal, including tumors in the prostate, were found to be detectable at 2-week postinjection based upon the NIR absorption contrast, which was detected a few weeks earlier than using NIR-reduced scattering and effective attenuation contrasts, as well as TRUS. Transrectal optical tomography detection of cancerous tissues *in vivo* in intact canine prostate based upon NIR contrasts may prove useful for diagnostic imaging of PCa and potentially aid in pretreatment planning for phototherapy applications.

Index Terms—Biomedical acoustics, biomedical optical imaging, diffuse optical tomography, prostate cancer (PCa).

I. INTRODUCTION

THE PROSTATE gland may not be considered as a life-sustaining organ, but prostate cancer (PCa) claims the lives of about 28 000 American men every year [1]. Lifetime risks for a diagnosis of PCa and as the cause of death for American men are 16% and 3%, respectively [2], [3]. Although the death rate of PCa has declined steadily in the past decade [1], [4], PCa remains a compelling medical health problem in American men [5].

There is broad consensus that current methods of diagnosing, staging, and treating PCa are inadequate [5], [6]. The diagnosis of PCa currently involves determination of prostate-specific

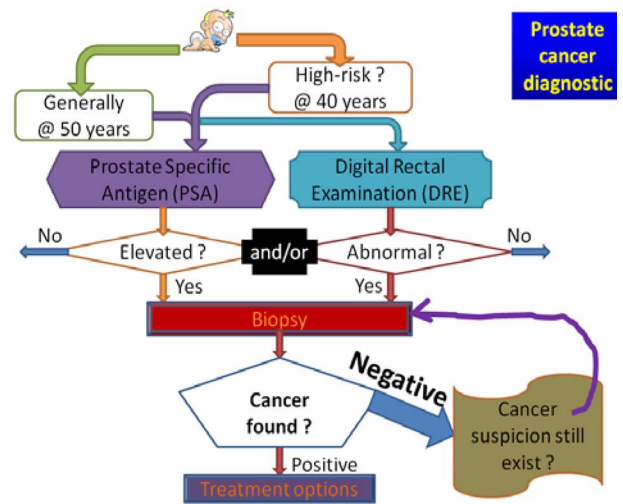


Fig. 1. Procedures involved in a PCa diagnostic.

antigen (PSA) and digital rectal examination (DRE), recommended to begin at 50 years of age for men with general risk or at 40 years of age for men with high risk, such as those individuals having a family history of PCa [7]. An abnormal PSA or DRE that provides a presumptive diagnosis of PCa is typically followed by biopsy procedures (illustrated in Fig. 1), which are performed on approximately 1 million American men each year. Prostate biopsy involves ultrasound (US)-guided transrectal needle insertion that provides at least six cores of tissue samples. Sampling 12–16 cores is the most commonly used template, but when indicated, saturation biopsies of up to 24–50 cores may be performed [8]–[10]. These multiple needle cores or “chips,” each ~1 mm wide and ~2 cm long, are sampled systematically from the entire gland, with some preference given to the peripheral zone of the prostate wherein most cancers are found [11]. Sampling of more than one core during the biopsy procedure is necessary because up to 85% of PCas are multifocal [12]; however, current systematic biopsy techniques have an overall cancer-positive rate of only 20%–25% [11], [13]. This low “positive” biopsy rate illustrates shortcomings to reliably detect and localize PCa using current outpatient imaging modalities.

Of the ~200 000 patients diagnosed with PCa each year, men with high-grade disease have a significantly greater survival rate with radical treatment (total excision), but men with low-grade PCa have a smaller absolute survival rate with radical treatment that is further compromised by the potentially adverse effects of current radical therapies [14]. Optimal treatment is thus directed

Manuscript received July 31, 2009; revised September 10, 2009 and September 28, 2009. This work was supported by the U.S. Department of Defense Army Medical Research Program under Grant W81XWH-07-1-0247.

D. Piao, Z. Jiang, G. Xu, and C. F. Bunting are with the School of Electrical and Computer Engineering, Oklahoma State University, Stillwater, OK 74078 USA (e-mail: daqing.piao@okstate.edu; zhen.jiang@okstate.edu; gary.xu@okstate.edu; reverb@okstate.edu).

K. E. Bartels and G. R. Holyoak are with the Department of Veterinary Clinical Sciences, Oklahoma State University, Stillwater, OK 74078 USA (e-mail: kenneth.bartels@okstate.edu; reed.holyoak@okstate.edu).

J. W. Ritchey is with the Department of Veterinary Pathobiology, Oklahoma State University, Stillwater, OK 74078 USA (e-mail: jerry.ritchey@okstate.edu).

G. Slobodov is with the Department of Urology, University of Oklahoma Health Sciences Center, Oklahoma City, OK 73104 USA (e-mail: Gennady-Slobodov@ouhsc.edu).

Color versions of one or more of the figures in this paper are available online at <http://ieeexplore.ieee.org>.

Digital Object Identifier 10.1109/JSTQE.2009.2034026

toward eradicating clinically relevant cancer, while at the same time leaving nonpathologic structures surrounding the prostate intact [14]. The optimal “targeted treatment” may include therapeutic choices, such as photodynamic therapy (PDT) [15] or photothermal therapy [16], for localized or recurrent PCa. The efficacy of phototherapy is dependent upon many factors, including the accuracy of profiling the cancer in the prostate, which is largely based upon transrectal ultrasound (TRUS) during treatment monitoring.

The need for more accurate imaging modalities, for both “targeted biopsy” and “targeted treatment,” have evoked investigation and development of a number of novel imaging technologies besides the standard modalities, such as US, MRI, computed tomography (CT), etc. Some of these novel approaches, which will be briefly reviewed in this paper, have emerged as alternative prostate imaging methods that provide new insights valuable in differentiating PCa from benign tissues. Among these emerging alternative prostate imaging technologies, the approach using near-infrared (NIR) light has seemed to provide unique information regarding optical properties of the *intact* prostate that may be useful for detecting malignant tissue and pretreatment dosimetry planning. Interpretation of the “noninvasively” acquired optical tomography images of the prostate relies on previous knowledge of prostate optical properties; therefore, a summary of what is known regarding the optical properties of both the canine and human prostate is also necessary.

This paper comprises following sections. In Section II, a brief review is provided regarding emerging alternative transrectally applicable prostate imaging modalities. In Section III, the known optical properties of canine and human prostates are summarized. The remaining sections discuss the transrectal diffuse optical tomography approach that is integrated with standard TRUS, and demonstrate the capability of detecting PCa *in vivo* in the canine model using transmissible venereal tumor (TVT).

II. EMERGING ALTERNATIVE TRANSRECTAL IMAGING TECHNOLOGIES FOR PROSTATE IMAGING

The deep intrapelvic position of the prostate dictates employing “transrectal” application in most prostate imaging modalities. Unlike MRI or CT scanners that are capable of imaging the whole body, but with the option of imaging a specific organ or tissue volume (such as in MRI using surface coils) for improved resolution, US is optimal for imaging a specific organ like the prostate gland, since the tissue–ultrasonic interaction requires dedicated transducer designs. The TRUS has become a “gold standard” for outpatient evaluation of the prostate because of its ability to reveal in real time the prostate morphology as well as the blood flow or tissue harmonic responses within the gland. For any alternative prostate imaging modalities developed for outpatient use, it is most likely that the modality would have to integrate with or rely on TRUS, unless the modality itself has real-time capability of visualizing the identifiable prostate morphology. A number of new approaches for prostate imaging, most of which have been demonstrated “transrectally” and some of which are in the stage of advancing to “transrectal” mode, are

briefly reviewed later to provide a “side-by-side” comparison of these modalities and their potential for PCa detection.

A. Alternative Transrectal Prostate Imaging Approaches Based on Tissue Mechanical Properties

The conventional TRUS images are formed based on the echogenicity originating from the acoustic index mismatches within the tissue. By taking advantages of tissue mechanical properties other than the acoustic indexes and other forms of tissue–ultrasonic interactions, a number of modalities are under development for prostate imaging.

The prostate mechanical imaging unit developed by Artann Laboratories, Trenton, NJ, employed a transrectal probe fitted with pressure sensor arrays and a 3-D orientation sensor. The pressure sensor array in the head of the probe evaluates spatial distribution of tissue hardness by measuring changes in pressure pattern in response to palpation of the prostate. The technique permitted real-time, cross-sectional imaging of the prostate and produced 3-D reconstructed elasticity images of the gland [17], [18].

The elastography or strain imaging is based on the fact that the backscattered US signal changes its local characteristic pattern only to a comparably small extent if the insonified tissue is slightly compressed and decompressed during the examination [19]. The time or space differences between local regions of interest under different compression ratios change with differences in compressibility of the insonified tissue. As the compressibility of local tissue regions is dependent upon the surrounding tissue and the applied compression force, estimation of tissue elasticity helps to discriminate hard-tissue from soft-tissue regions [19]. Prostate imaging has also been investigated by use of acoustic radiation force that produces a map of the mechanical response of an object to a dynamic force applied at each point. The method remotely exerts a localized acoustic stress field, at a desired frequency, within or on the surface of an object, and records the resultant acoustic response or acoustic emission. Depending on the elastic properties of the object, the radiation force may cause the object to vibrate at a predetermined frequency. Such acoustic response is a measure of the tissue viscoelasticity that has shown differences between malignant and benign prostate tissues [20], [21].

All these modalities have relied upon mechanical signatures that PCa may have. The advantages of these modalities, for those employing ultrasonic energy, are the minimal modification necessary to the US transducer, signal detection, and image formation when comparing with other approaches.

B. Alternative Transrectal Prostate Imaging Approaches Based on Tissue Electrical Properties

The electrical property of tissue is primarily a result of its underlying morphology [22]. The relative intracellular and extracellular fluid volumes and ionic concentrations, and the cellular membrane extent in the tissue, respectively, constitute a frequency-dependent reactive component of bioimpedance, which also has a relatively frequency-independent resistive component [23]. The complex electrical properties represented by

bioimpedance include conductivity and relative permittivity. Imaging of these electrical properties [24] have been proposed by using transrectal electrical impedance tomography [22], [23] coupled with TRUS that may act as a screening device secondary to PSA monitoring or serve as an imaging technique with enhanced lesion specificity for biopsy guidance. Such development has been based on pilot studies suggesting that the electrical properties of PCa may be noticeably different from those of benign tissues within the gland; specifically, the conductivity of malignant tissue in the prostate is found less than that of benign tissues [22], [23].

C. Alternative Transrectal Prostate Imaging Approaches Based on Tissue Optical Properties

Recently, there are several investigations into using NIR light to detect PCa. All these methods are based on optical contrasts of chromophores, either intrinsic or exogenous, which have different concentration in malignant and benign tissues. If the intrinsic optical contrast comes from the difference of hemoglobin content (e.g., total hemoglobin and proportion of oxygenated hemoglobin), it is considered to be associated with angiogenesis and hypoxic changes that are characteristic for a proliferating tumor. One example of utilizing the intrinsic optical contrast is a hybrid laser optoacoustic and ultrasonic imaging method [25], [26]. Transient acoustic signals are generated by pressure that precedes thermal expansion of tissue following the absorption of a short laser pulse. The optoacoustic imaging reconstructs ultrasonic images of intrinsic light absorber that shows regions of tissue with enhanced absorption contrast. Some other approaches have implemented optical contrasts that are exogenously administered, such as utilizing gold-nanorod contrast agent [27], Cytate [28], and other fluorescent imaging approaches [29]. All these modalities are suited for transrectal development.

The aforementioned approaches involve using NIR light. It is noted that the efficacy of light-based imaging modalities not only depends upon the existence of an intrinsic or exogenous optical contrast associated with the cancer, but also the optical properties of the normal tissue, which determines if the photon illumination can reach a specific tissue volume, and if the optical contrast of the malignant tissue over normal tissue is resolvable out of any background heterogeneity. In this regards, it is necessary to examine the current knowledge of the prostate optical properties.

III. OPTICAL PROPERTIES OF CANINE AND HUMAN PROSTATES

Using light to image prostate cancer will not be achievable unless a benign and cancerous prostate tissues present different optical properties that can be resolved by means of optical interrogation. Revealing the contrast of PCa over normal tissue will be challenging if significant baseline heterogeneities exist in the optical properties of benign tissues. There have been a number of studies on prostate optical properties in which certain consensus have been made. Although these studies are conducted at different wavelengths, in different samples, and using different methods, spectrally these studies shall offer informa-

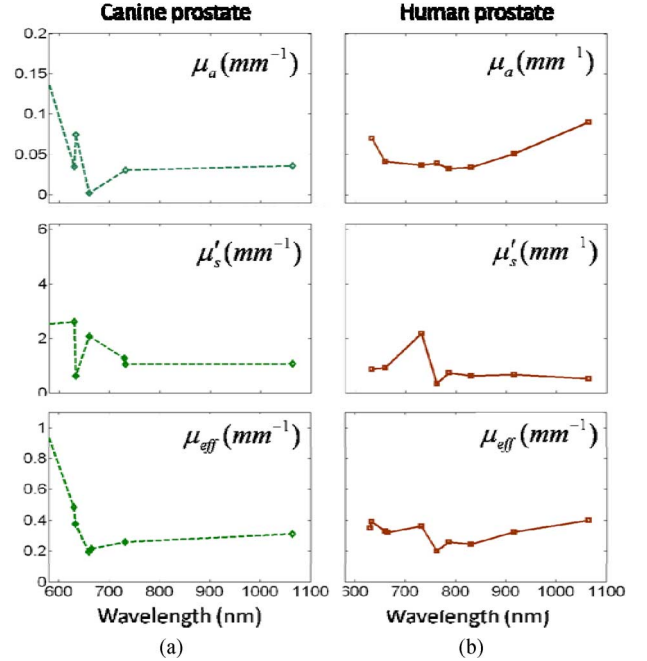


Fig. 2. Optical properties, including absorption, reduced scattering, and effective attenuation coefficients, averaged for existing studies at available spectral band for (a) canine and (b) human. The canine data are of normal tissue only, but the human data are of benign and malignant tissues.

tion invaluable to understanding the potentials of detecting PCa as well as difficulties facing the optical imaging of prostate. In this section, we give a side-by-side review of the known optical properties of canine and human prostates.

Dogs have been used in a number of prostate studies because of the similarity between canine and human prostate glands. In [30], we have summarized the studies previous to ours, on optical properties, including absorption coefficient μ_a , reduced scattering coefficient μ'_s , and effective attenuation coefficient μ_{eff} of canine prostate within the spectral range from 355 to 1064 nm. These measurements, all performed invasively, include the following:

- 1) coefficients μ_a , μ'_s , and μ_{eff} of normal canine prostate tissue *in vitro* at 355, 532, and 1064 nm, respectively, using optoacoustic measurements of slab tissue samples [31];
- 2) coefficients μ_a , μ'_s , and μ_{eff} at 630 nm by interstitial measurements on excised normal prostate [32];
- 3) *in vitro* μ_a and μ'_s of slab samples of normal canine prostate tissues evaluated at 633 nm by using the standard double-integrating sphere technique [33];
- 4) coefficient μ_{eff} at 630, 665, 730, 732 nm by interstitial measurements on normal canine prostate *in vivo* before and after PDT [34]–[37];
- 5) coefficient μ_{eff} at 732 nm by reflection measurement upon exposed normal canine prostate *in vivo* [38];
- 6) transperineal interstitial measurement [35], [36], [39], [40] demonstrating that μ_{eff} of prostatic urethral regions is statistically higher than that of the prostatic capsular regions.

These measurements together constitute the spectra of the optical properties of normal canine prostate [30], as replotted in Fig. 2(a), after averaging at each band.

TABLE I
LEGEND INDICATING THE MEASUREMENT METHODS USED IN TABLE II





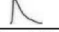

























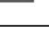

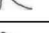





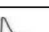






				
Integrating sphere on slab tissue	Interstitial on excised prostate	Interstitial trans-perineally on prostate	Steady-state fluence rate measurement	Time-resolved fluence rate measurement

TABLE II
CURRENT “INVASIVE” KNOWLEDGE OF THE OPTICAL PROPERTIES OF HUMAN PROSTATE (EXPANDED UPON THE TEMPLATE IN [41])

Study	Year	Sample	Path	N	Method	Photon	λ (nm)	μ_a (mm ⁻¹)	μ'_s (mm ⁻¹)	μ_{eff} (mm ⁻¹)
Lee [48]	1999	<i>In vivo</i>	PCa	7			630			0.35±0.07 (0.22-0.44)
Pantelides [42]	1990	<i>Ex vivo</i>	Normal	3			633	0.07±0.02	0.86±0.05	0.43±0.05
Whitehurst [46]	1994	<i>In vivo</i>	BPH PCa	11			633			0.35±0.02 0.36±0.02
Lee [47]	1995	<i>In vivo</i>	BPH PCa	11			633			0.39±0.05 (0.24-0.42)
Wei [43]	2008	<i>In vitro</i>	BPH	?			640	0.44~0.96	1.12~1.66	2.09±0.54
Svensson [41]	2007	<i>In vivo</i>	PCa	9			660	0.05±0.01	0.87±0.19	0.36±0.08
Svensson [52]	2008	<i>In vivo</i>	PCa	1			660	~0.032	~0.5-1.4	0.23-0.37
Lee [47]	1995	<i>In vivo</i>	BPH UT PCa	11			665			0.32±0.05 (0.24-0.42)
Zhu [49]	2005	<i>In vivo</i>	RC PCa	13			732	0.037±0.024 (0.007—0.162)	1.40±1.10 (0.11—4.4)	0.29±0.07 (0.091—0.67)
Zhu [50]	2005	<i>In vivo</i>	RC PCa	2			732	0.011—0.16	0.12—4.0	0.019—0.63
Li [53]	2008	<i>In vivo</i>	RC PCa	1			732	2-D map 0.01—0.1	2-D map 0.5—4.5	0.65±0.37
Wang [54]	2009	<i>In vivo</i>	RC PCa	1			732	3-D map 0.01—0.07	3-D map 0.1—5.5	0.19-0.41
Weersink [51]	2005	<i>In vivo</i>	RC PCa	22			762	0.039±0.018	0.34±0.16	0.20±0.06
Svensson [41]	2007	<i>In vivo</i>	PCa	9			786	0.04±0.01	0.71±0.16	0.29±0.07
Svensson [52]	2008	<i>In vivo</i>	PCa	1			786	0.025	0.35-1.2	0.17-0.30
Svensson [52]	2008	<i>In vivo</i>	PCa	1			830	0.034	0.25-1.0	0.17-0.32
Svensson [41]	2007	<i>In vivo</i>	PCa	9			916	0.06±0.01	0.77±0.18	0.38±0.08
Svensson [52]	2008	<i>In vivo</i>	PCa	1			916	0.042	0.24-0.9	0.19-0.34
Essebreis [44]	1992	<i>Ex vivo</i>	Normal	?			1064	0.15±0.02	0.64	0.60
Roggan [45]	1995	<i>Ex vivo</i>	Normal	?			1064	0.03	0.4	0.2

UT: untreated and RC: recurrent.

Following [30], the published values on optical properties of human prostate, all acquired invasively, as illustrated in Table I, are summarized in Table II, which enriched the template given in [41] with latest studies. The studies summarized in Table II include the following:

- 1) *ex vivo* steady-state measurements of μ_{eff} and $\mu'_t = \mu_a + \mu'_s$ at 633 nm in three whole, nonmalignant human prostates [42];
- 2) three postmortem studies estimating prostate optical properties (μ_a , scattering coefficient μ_s , scattering anisotropy g , and μ'_s) at 640 [benign prostatic hyperplasia (BPH)] [43] and 1064 nm (normal prostate) [44], [45] by measuring through thin prostate slices;
- 3) coefficient μ_{eff} of prostate *in vivo* diagnosed with BPH or PCa estimated at 633 nm by steady-state interstitial mea-

surements [46], [47] that indicated similar μ_{eff} between benign and malignant prostate tissues;

- 4) at wavelengths of 630, 665, 732, 762 nm, transperineal interstitial steady-state measurements on prostate *in vivo* with untreated BPH, untreated PCa, and recurrent PCa conducted before and after PDT [47]–[51] to determine μ_{eff} or both μ_a and μ'_s ;
- 5) coefficients μ_a , μ'_s , and μ_{eff} of untreated PCa *in vivo* at 660, 786, 830 and 916 nm, respectively, using time-resolved fluence rate measurements [41], [52];
- 6) a few studies on hemoglobin and oxygen saturation [41], [50], [51] indicating relatively small variations of oxygen saturation, but large variations on total hemoglobin concentration within the same gland or different subjects.

Recently, interstitially measured 2-D or 3-D distribution of μ_a and μ'_s , in human prostate, are reported [53], [54] for PDT dosimetry.

Studies [49], [51] have indicated that the optical properties of canine prostate and human prostate may be substantially different, specifically the absorption properties. It is noted that the studies of canine prostate optical properties have been performed on all normal glands, but that of human include both normal, benign hyperplastic, and malignant prostate tissues. It is also noted that these studies are conducted at different wavelengths, using different methods, on *ex vivo* or *in vivo* samples. Direct wavelength-specific and tissue-specific comparisons of the canine and human prostate optical properties are, thereby, difficult, but nonetheless, the spectra of the optical properties of canine and human prostates may reveal useful information. To facilitate spectral comparison, for those original measurements of human prostate shown in Table II that have only the absorption and reduced scattering coefficients available, the effective attenuation coefficient is calculated following the method in our previous study [30]. Fig. 2(b) illustrates the spectra of μ_a , μ'_s , and μ_{eff} of human prostates that are averaged for existing data at a specific wavelength. The distributions of the optical properties of both canine and human prostates are substantially large, as seen in [30] and Table II, and are not plotted in Fig. 2.

The spectra shown in Fig. 2 are the invasively characterized optical properties of normal canine prostates and mostly malignant human prostates. The similarity or dissimilarity between canine and human prostate optical properties is difficult to draw as the optical properties of malignant canine prostate tissue were previously unavailable; however, previous studies that are summarized in [30] and Table II, and seen in Fig. 2, have important implications to optical interrogation of the prostate in the following aspects.

- 1) The reduced scattering coefficient of prostate is approximately an order higher than the absorption coefficient of prostate. As this has been confirmed by time-resolved measurements, the prostate can be treated as a scattering-dominant tissue, thereby diffuse optical methods can be applied to modeling the photon propagation as in PDT and image reconstruction in transrectal imaging of the prostate.
- 2) There are noticeable intersubject and intraorgan heterogeneities in optical properties of prostate. The intraorgan heterogeneity poses a substantial challenge to differentiating malignant tissue from normal tissue, since the optical contrast of the malignant tissue over the normal tissue must be greater than the background heterogeneity for the malignant lesion to be resolved. The intraorgan heterogeneity may also partially contribute to the previous finding that the effective attenuation coefficients of benign and malignant human prostate tissues were similar. It is noted that none of the previous measurements of prostate optical heterogeneities have been examined on intact prostate *in vivo*. Our approach of transrectal NIR diffuse optical tomography, which aims at imaging the intact prostate in its real-time *in vivo* condition, shall demonstrate if and which

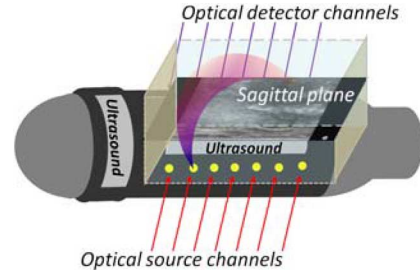


Fig. 3. Geometry of transrectal NIR imaging probe coupled to the sagittal US transducer of a biplane prostate-imaging TRUS probe.

type of intrinsic optical property contrasts are available for differentiating the malignant prostatic tissue from benign tissue.

IV. METHODS AND MATERIALS

A. Transrectal NIR Imaging Probe

Due to the limitation of spatial resolution and the time needed for image formation in diffuse optical tomography, it is imperative to give transrectal NIR prostate imaging a real-time positioning guidance, which most conveniently can be rendered by TRUS. The need of dual-modality endorectal application leaves limited options as to what can be done to the NIR applicator designs. There has to be a clear window for the TRUS transducer, and there has to be a relatively longitudinal NIR array to allow co-parallel imaging into deeper tissue. The NIR probe design is shown in Fig. 3. The longitudinal NIR source array and detector array are placed lateral to the sagittal TRUS transducer of a biplane TRUS probe [55]. This NIR array geometry allows imaging a tissue volume that is dissected by the sagittal TRUS imaging plane. As the NIR array has a dimension of 60 mm \times 20 mm (longitudinal \times lateral), the NIR image reconstruction is performed in 3-D in a volume of 80 mm \times 70 mm \times 50 mm (longitudinal \times lateral \times depth). Since the sagittal US performs only 2-D imaging, obtaining a 3-D morphological profile of the prostate from US becomes unreliable using single sagittal US image. Therefore, no spatial *a priori* information has been implemented in the transrectal NIR tomography image reconstruction, which utilizes a mesh of uniform density. The NIR wavelength is chosen at 840 nm.

B. Image Reconstruction

As the transrectal NIR optical tomography system takes continuous-wave measurement [55], the forward computation is based upon the steady-state photon diffusion equation

$$\nabla \kappa(\vec{r}) \nabla \Phi(\vec{r}) - \mu_a(\vec{r}) \Phi(\vec{r}) = -q(\vec{r}) \quad (1)$$

where κ is the diffusion coefficient that is equal to $1/[3(\mu_a + \mu'_s)]$, Φ is the photon fluence rate at position \vec{r} , and q is the source at \vec{r} .

The probe-tissue boundary is represented by an index-mismatched type-III condition (also known as the Robin boundary condition), in which the photon fluence existing at the edge

of the tissue does not return [56], [57]. This boundary condition is described by

$$\Phi(\vec{r}_\Omega) + 2A\kappa \hat{n} \cdot \nabla \Phi(\vec{r}_\Omega) = 0 \quad (2)$$

where \vec{r}_Ω corresponds to the point on the boundary, \hat{n} is a unit vector pointing outward (from the tissue to probe) and normal to the tissue–probe interface, and A is determined by the relative refractive index mismatch between the tissue domain and the probe (air) domain. Specifically

$$A = \frac{(2/(1 - R_0)) - 1 + |\cos \theta_c|^3}{1 - |\cos \theta_c|^2} \quad (3)$$

$$R_0 = \frac{((n_{\text{tissue}}/n_{\text{air}}) - 1)^2}{((n_{\text{tissue}}/n_{\text{air}}) + 1)^2} \quad (4)$$

$$\theta_c = \arcsin \left(\frac{n_{\text{air}}}{n_{\text{tissue}}} \right) \quad (5)$$

where n_{tissue} is the refractive index of tissue (chosen as 1.33) and n_{air} is the refractive index of the probe/air (chosen as 1.0).

Equation (1) is solved by finite-element method (FEM) formulated as [1]

$$[K(\kappa) + C(\mu_a) + \xi F] \Phi = Q_0 \quad (6)$$

where $\xi = (2A)^{-1}$ is a constant to implement the boundary condition in (2). For each element of the FEM mesh

$$K_{ij}^e = \int_{\Omega} \kappa(r) \nabla u_i(r) \cdot \nabla u_j(r) d\Omega \quad (7)$$

$$C_{ij}^e = \int_{\Omega} \mu_a(r) u_i(r) u_j(r) d\Omega \quad (8)$$

$$F_{ij}^e = \oint_{\partial\Omega} u_i(r) u_j(r) d\Lambda \quad (9)$$

$$Q_{0i}^e = \int_{\Omega} u_i(r) q_0(r) d\Omega \quad (10)$$

where $u = a + bx + cy + dz$ is a linear shape function for each nodes, K , C , and Q are the volume integrals of each element, and F is the surface integral of the boundary element. Following the FEM routine of matrix assembly and fluence rate calculation, the boundary measurements are interpolated as weighted averages of the fluence rates of the nodes adjacent to the measurement points.

The inverse problem involves Levenberg–Marquardt algorithm implemented as

$$x_{k+1} = x_k + \alpha [J^T(x_k) J(x_k) + \lambda I]^{-1} J^T(x_k) \Delta v(x_k) \quad (11)$$

where x is the optical properties to be reconstructed, Δv is the forward projection error, λ is a regularization term, J is the Jacobian or the weight matrix containing the first-order derivative of the measurements with respect to the changes of optical properties, and α is a damping factor in the range of (0, 1) used for preventing over-adjustment of optical properties and rendering stable convergence [58]. The iteration stops when the

projection error changes less than 1% or negative values in x occur.

The Jacobian in (11) is calculated by an adjoint method [1] based on the following equations with the basis matrix of FEM:

$$J_{i,j}^\kappa = \frac{\Psi_j^{*T} V(\kappa) \Phi_i}{v_{i,j}} \quad (12)$$

$$J_{i,j}^{\mu_a} = \frac{\Psi_j^{*T} V(\mu) \Phi_i}{v_{i,j}} \quad (13)$$

where Φ_i is the fluence rate at each node in the FEM mesh generated by the i th source, Ψ_j is the fluence rate generated by assuming an adjoint source at the position of the j th detector, $v_{i,j}$ is the computed measurements at the j th detector for the i th source. $V(\kappa)$ and $V(\mu)$ are the finite-element system basis of

$$V_{ij}^e(\kappa) = \int_{\Omega} \nabla u_i(r) \cdot \nabla u_j(r) d\Omega \quad (14)$$

$$V_{ij}^e(\mu_a) = \int_{\Omega} u_i(r) u_j(r) d\Omega \quad (15)$$

The assembled Jacobian in (11) contains two parts as

$$[J_{i,j}^{\mu_a} \quad J_{i,j}^\kappa] = \begin{bmatrix} \frac{\partial I_{i,j}}{\partial \mu_a} & \frac{\partial I_{i,j}}{\partial \kappa} \end{bmatrix} \quad (16)$$

where i is the sequence number of the source and j is the sequence number of the detector. A mesh of 8881 nodes is used for the forward computation, and the inverse reconstruction basis contains a mesh of 832 nodes. After the μ_a and κ are reconstructed, μ_s' is computed as $[(1/3\kappa) - \mu_a]$, and μ_{eff} is estimated by $\sqrt{\mu_a/\kappa}$.

C. Animal Models

The studies were conducted at Oklahoma State University under protocols approved by the University's Institutional Animal Care and Use Committee, and approved by the US Army Medical Research and Materiel Command after an on-site inspection. For this study, the prostate of a 12-kg sexually intact adult purpose-bred Beagle dog, estimated to be approximately 4 years of age, was injected with canine TVT cells [59]. The TVT cell line was propagated *in vivo* in the subcutis of nonobese-diabetic (NOD)/severe-combined-immunodeficiency (SCID) mice. When the subcutaneous tumor reached an appropriate volume, the neoplastic cells were recovered and homogenized for injection into the canine prostate gland. With the dog under general anesthesia, approximately 3 cc of TVT cells were aseptically injected transperineally into the right lobe of the prostate using a 6-in-16-gauge hypodermic spinal needle under TRUS visualization. The spinal needle was retracted without inserting the inner stylet; therefore, it was assumed that TVT cells could potentially leak from the prostate injection site and be “seeded” along the needle insertion tract. The dog underwent monitoring in 2, 5, 6, and 7 weeks postinjection, and was then humanly euthanized for necropsy and histological examinations at 8 weeks postinjection.

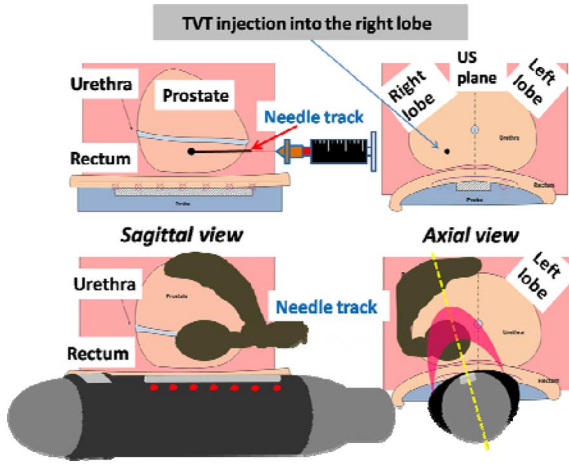


Fig. 4. (Top) Injection of canine TVT cells to the right lobe of a dog prostate. (Bottom) Growth pattern of the tumor revealed by later necropsy and histological examinations.

V. RESULTS

During the first two-week evaluation after TVT injection, there was no evidence of tumor growth on TRUS and rectal examination. The TRUS examination at 5 weeks postinjection showed hypoechoic masses in the prostatic parenchyma, periprostatically around the right lobe of the prostate, and perirectally along the injection track.

A. NIR Absorption Imaging

The NIR absorption images taken prior to TVT injection, at 2-weeks, and at 5 weeks postinjection are displayed in Fig. 5. The sagittal TRUS image and the sagittal NIR image, to which it coupled, are identified in Fig. 5. The axial TRUS images were acquired in week-5 only, therefore, comparison of the axial NIR with axial TRUS images could not be made for results obtained at either preinjection or at week-2 post-injection.

The US and NIR images are displayed with the same dimension of 60 mm \times 30 mm (cranial-caudal \times dorsal-ventral) for sagittal, 40 mm \times 30 mm (right lateral-left lateral \times dorsal-ventral) for axial, and 60 mm \times 40 mm (cranial-caudal \times right lateral-left lateral) for coronal views, respectively. The sagittal transrectal US images were taken at the middle portion of the right lobe (see Fig. 4, bottom right for the imaging view). For week-5 US images, the hypoechoic region L1 indicates an intraprostatic mass. The large hypoechoic region L2 indicates a mass ventral and caudal to the prostate that may have connection with L1. The NT on the US image denotes the needle trajectory for introducing the TVT cells. Longitudinal hypoechoic regions including L3 are seen along the NT. The hyperabsorptive regions on sagittal NIR images correspond to L1, L2, and L3 on sagittal US image. The 10-mm-medial NIR image displays the absorptive masses at reduced NIR contrast, and the 10-mm-lateral NIR image reveals connected strong absorptive masses.

The three axial TRUS images were taken at the cranial edge of the prostate at a plane crossing L1, the caudal edge of the prostate at a plane crossing L2, and the perirectal region at a plane crossing L3, using the axial TRUS transducer. The axial

US images show a small hypoechoic intraprostatic mass at the cranial aspect of the prostate, the distortion of the right lobe boundary, and the extension of L2 over the prostate midline. These correlate with the findings on other sagittal US performed at midline, and the imaging of a large perirectal hypoechoic mass cranial to the perineum. The locations of axial NIR images are comparable to those of the axial transrectal US. The axial NIR image A2 should contain L1, and the axial NIR image A5 should contain L3. The coronal NIR images are reconstructed at planes of 5, 10, and 15 mm ventral to the rectum. On coronal images, the hyperabsorptive mass, indicative of L1, is seen medial to the hyperabsorptive masses indicative of L2 and L3. The masses indicative of L2 and L3 are seen to align longitudinally, a feature corresponding to tumors developed along the needle track running parallel to the rectum or the transrectal probe surface.

At the week-2 NIR absorption images, hyperabsorptive regions were found intraprostatically in the right lobe and dorsal to the pelvic bone. The longitudinal locations of these hyperabsorptive regions correlated well with those of the US hypoechoic and NIR hyperabsorptive regions found in week-5. The change of the hyperabsorptive regions from week-2 to week-5 implied tumor growing in the right lobe and potentially extending toward the middle line of the prostate. The growth of the tumor was indicated earlier by the NIR absorption images than by the TRUS, and combining the information of NIR and TRUS could lead to earlier and more accurate findings of tumor growth than with TRUS alone.

B. NIR-Reduced Scattering and Effective Attenuation Imaging

The NIR-reduced scattering and effective attenuation images, with timeline and geometry identical to those of NIR absorption in Fig. 5, are displayed in Figs. 6 and 7, respectively.

The hyperabsorptive masses presumed to be TVTs in NIR absorption images are shown with different contrast patterns for the reduced scattering and effective attenuation coefficients. In both the NIR-reduced scattering and effective attenuation images of week-5, the indications of masses corresponding to L1, L2, and L3 are not as profound, as in NIR absorption images, whereas L3 has much higher contrast than do the masses corresponding to L1 and L2. The contrast elsewhere is also more heterogeneous compared with that in the absorption image at the given color scales.

On the NIR-reduced scattering and effective attenuation coefficient images of week-2, it is difficult to find regions with elevated contrast that could correlate with the hyperabsorptive regions in the NIR absorption images that were located intraprostatically in the right lobe and dorsal to the pelvic bone.

C. Overall Changes of Optical Properties of the Three Tumor Regions Identified in Week-5

From the three hyperabsorptive regions on week-5 images that have longitudinal position correlation with the US hypoechoic tumor-suspecting regions, three circular regions are defined, as

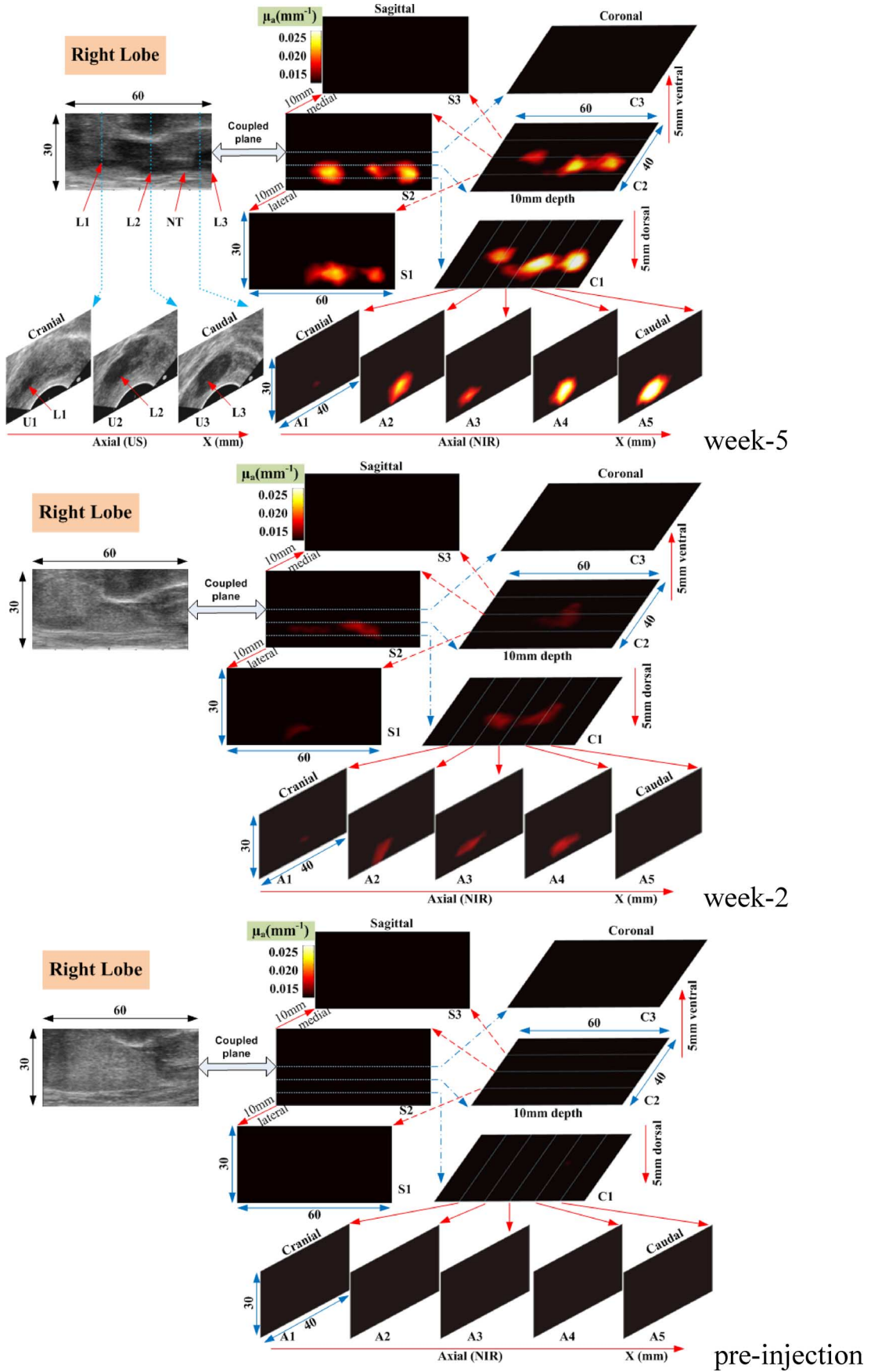


Fig. 5. Transrectal NIR optical tomography of canine TVT tumor images of absorption coefficient.

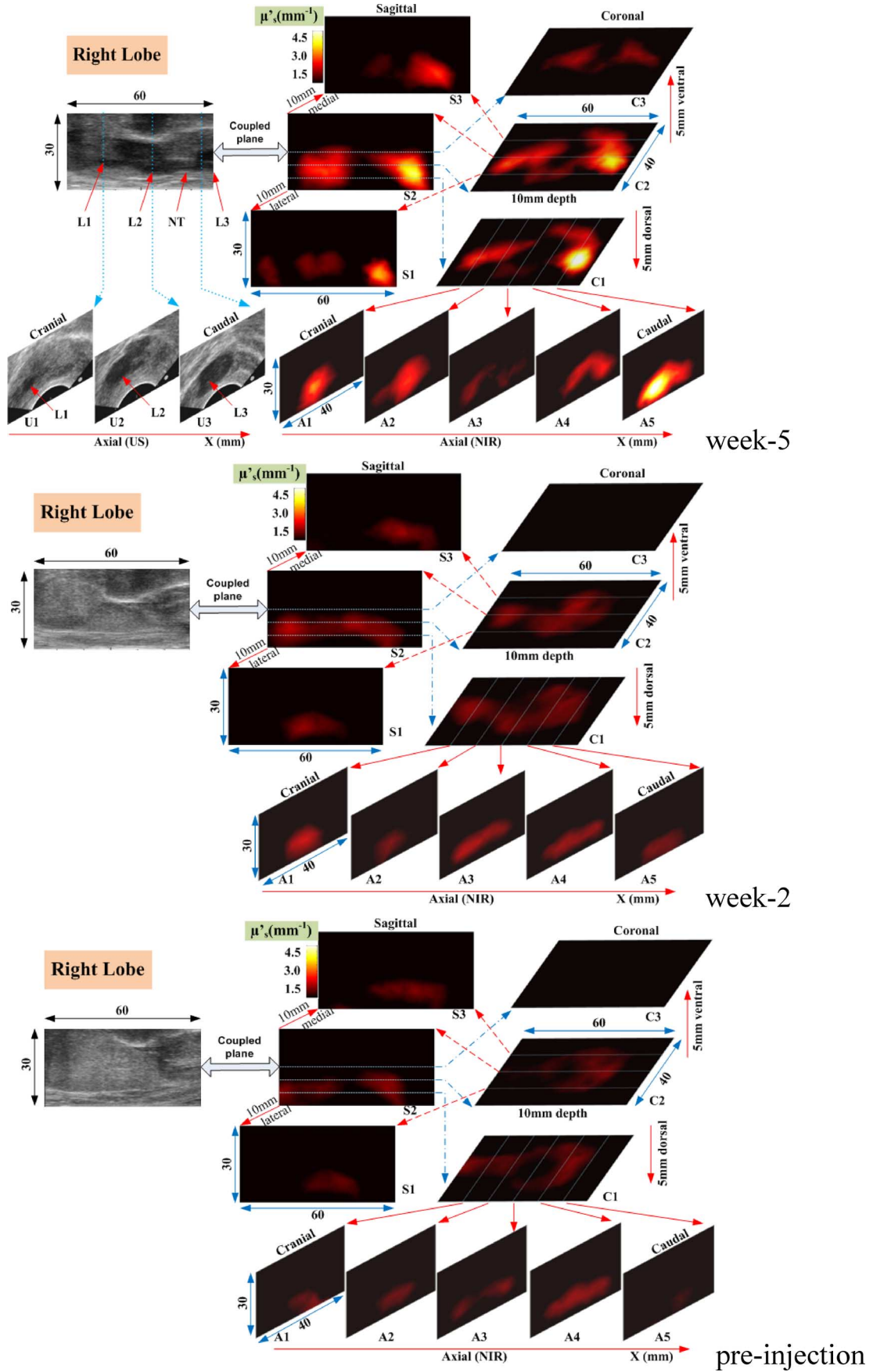


Fig. 6. Transrectal NIR optical tomography of canine TVT tumor images of reduced scattering coefficient.

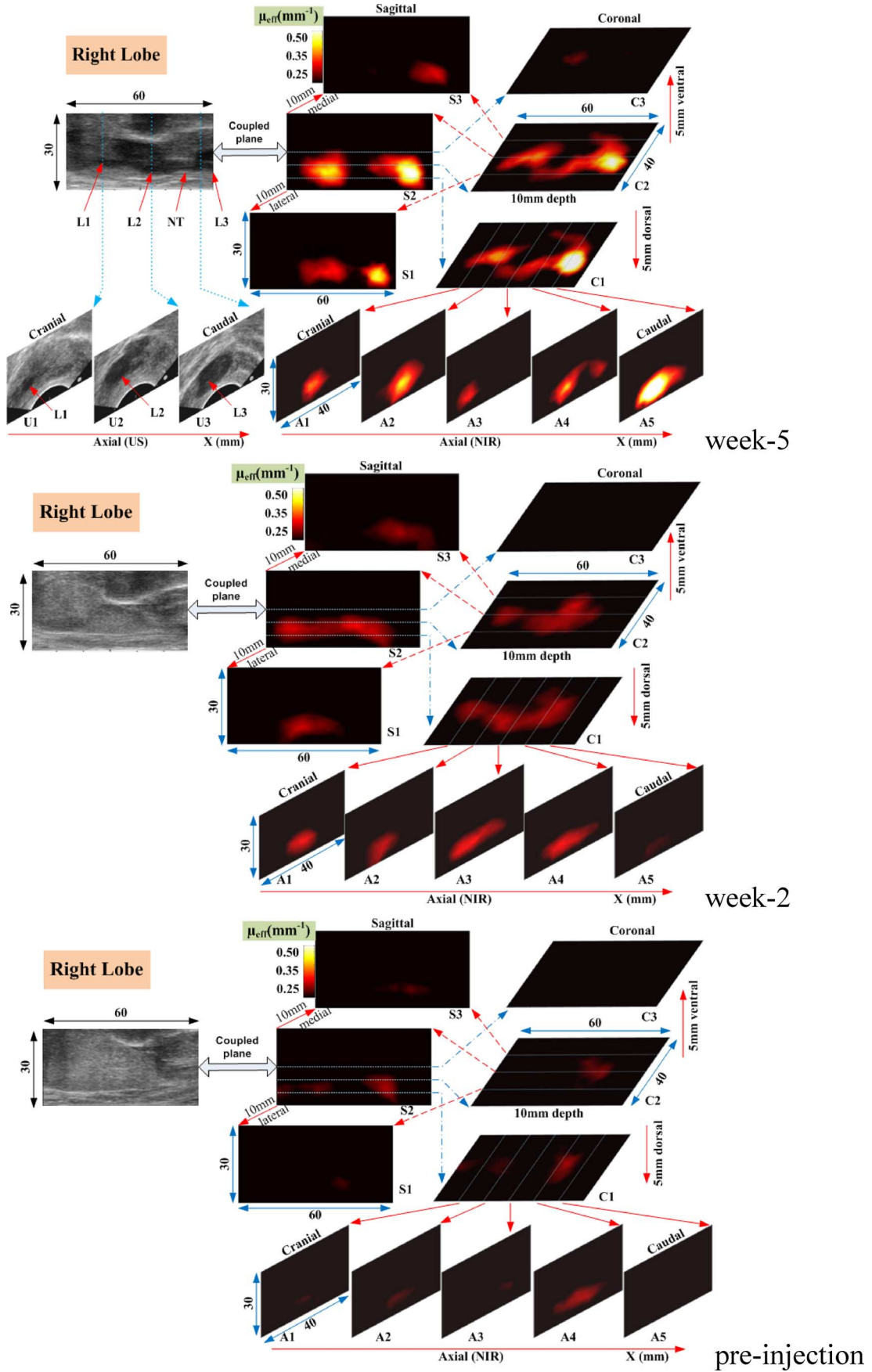


Fig. 7. Transrectal NIR optical tomography of canine TVT tumor images of effective attenuation coefficient.

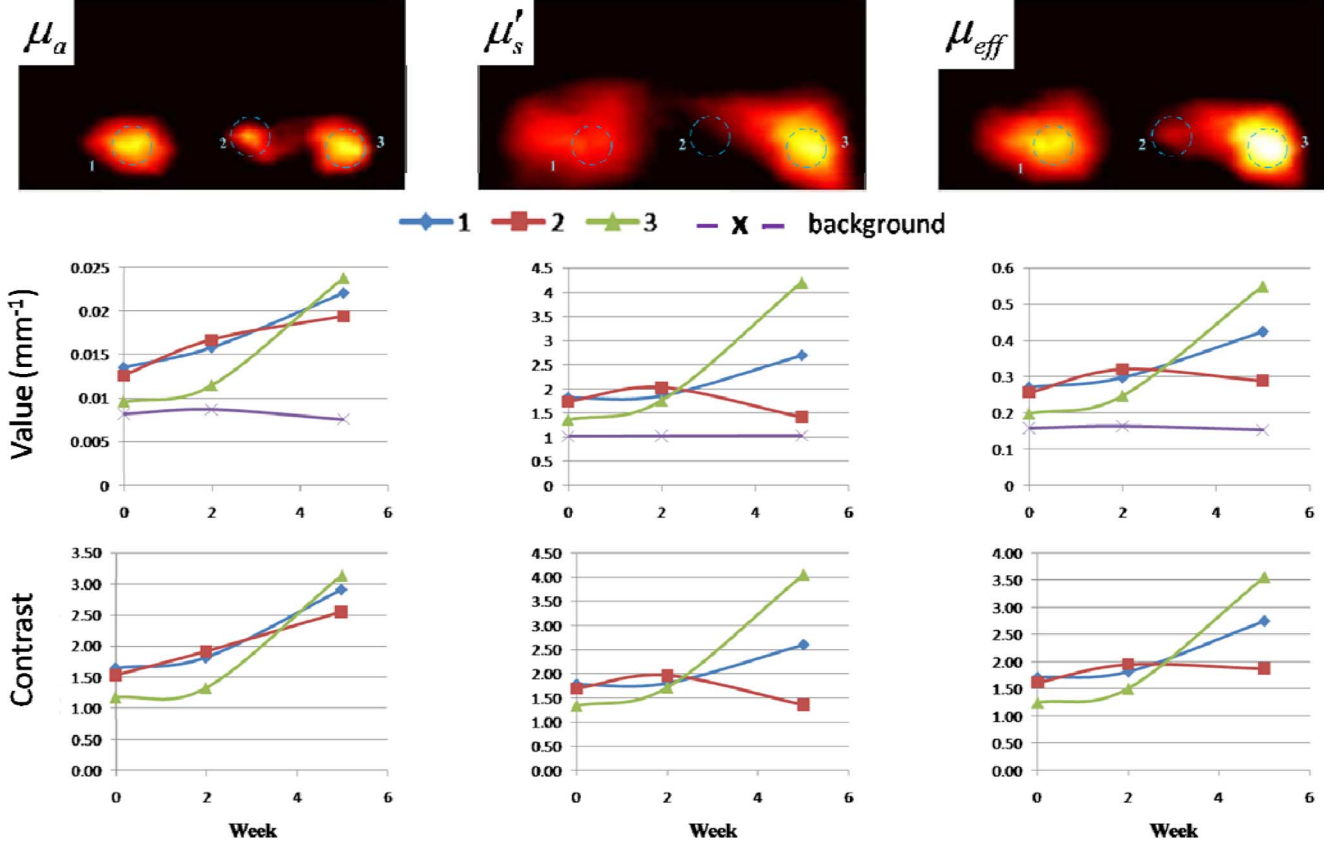


Fig. 8. Changes of the reconstructed optical properties at the three circular regions corresponding to L1, L2, and L3 in Figs. 5, 6, and 7, respectively. (Top) NIR absorption, reduced scattering, and effective attenuation acquired at the middle of the right lobe in week-5, corresponding to those in Figs. 5, 6, and 7 that are “coupled with” the single sagittal US image. (Middle) Absolute values of the mean optical properties in the three circular regions. (Bottom) Contrast of these optical properties with respect to the background values calculated by averaging after excluding the three circular regions.

seen in Fig. 8. The changes of the reconstructed optical properties at the three regions with respect to the background value (averaged on the sagittal plane with the three circular regions excluded) over the 5-week time line are shown in Fig. 8. The absorption coefficients at all the three regions show moderate increase at week-2 and substantial increase in week-5. However, the increase of the reduced scattering and effective attenuation coefficients are seen for regions 1 and 3 only, and at week-5, but not at week-2.

D. Confirmation of the Tumor Growth

The gross and histological findings confirmed intra- and periprostatic neoplastic infiltrates with masses also located along the pelvic urethra and perirectal tissue; the latter related to dissemination along the needle track, as the needle was withdrawn following TVT inoculation in the prostate. Histologically, all masses consisted of diffuse sheets of a monomorphic population of neoplastic round cells dissecting through pre-existing fibrovascular stroma. The neoplastic cells have large hyperchromatic nuclei, single conspicuous nucleoli, and moderate amounts of featureless cytoplasm—features histologically consistent with canine TVT.

VI. DISCUSSIONS

It is noted that the NIR probe consists of a linear source array and a linear detector array separated 20 mm laterally and sym-

metrically parallel to the TRUS imaging plane. The NIR lateral detection sensitivity is thereby peaked at the midline plane [30]. As the 6-cm-long NIR array performs side-way imaging, the detection sensitivity is optimal at approximately 1.5 cm from the probe surface. In the transrectal NIR image reconstruction, a uniform meshing throughout the entire imaging volume is implemented, therefore, the target located at regions with higher detection sensitivity may be recovered successfully, but targets located at regions with much lower detection sensitivity may not be fully resolved. This accounts for the lack of visualized lesions on the 15-mm coronal plane and those extending ≥ 15 mm lateral to the midline plane. Improvement in the recovery of the lesions at deeper region and more lateral aspect may be achieved by advanced reconstruction approaches, such as applying accurate spatial prostate profile information to the reconstruction process, which nonetheless requires 3-D TRUS capability for this study.

The advanced TVT tumors developed in the canine prostate and elsewhere in the pelvic canal are shown as highly absorbing and more scattering, thereby more attenuating, over the peripheral tissues. However, it seems that the TVT tumor development induced a detectable NIR absorption contrast much earlier than the detectable reduced scattering and effective attenuation contrasts. Previous studies revealed similar effective attenuation properties between benign and malignant prostatic tissues, which are in agreement with this study for the

measurements made at the earlier stage of tumor development. However as the tumor becomes much advanced, the effective attenuation contrast of the tumor becomes elevated substantially over the background.

The TVT is a round cell tumor that has characteristics such as distinct tumor boundary, higher and homogenous cell density, large hyperchromatic nuclei, single conspicuous nucleoli, etc. All these characteristics could contribute to the elevation of optical properties as revealed by transrectal NIR optical tomography. The higher cell density and large hyperchromatic nuclei could increase both the absorption cross-section and scattering cross-section of the NIR light being used. The distinct tumor boundary may introduce specular light reflection at the tumor boundary, as the refractive indexes will highly likely have an abrupt change between the normal tissue and the high-density tumor. The specular reflection, if it occurs, may be reconstructed as elevated absorption, as seen distinct to the TVT nodules. As the specular reflection scatters more light into the tissue peripheral to the tumor, the "true" scattering of the peripheral tissues may be reconstructed with artifacts that may reduce the overall scattering contrast of the tumor over its peripheral tissues, as may have been shown in the figures.

We recognize that since the cellular and subcellular structures of the TVT tumor are distinctly different from those of prostate adenocarcinoma, the absorption, scattering, as well as effective attenuation features of the prostate adenocarcinoma may become much different from those of TVT, as seen in this study. If the PCa develops into larger cells, the absorption and scattering cross sections may be decreased, but the malignant irregular cellular structures may increase the scattering, and the onset of angiogenesis may increase the absorption. As the PCa typically does not have a distinct boundary as the TVT tumor does, the influence of specular reflection may be minimized under light interrogation; thereby, the PCa may be presented with its more unaltered absorption contrast if imaged by NIR light. There are limited studies on the contrast of the optical properties of PCa versus benign tissue from which controversial observations are often implicated. The introduction of this transrectal optical tomography, which aims to spatially resolve the optical properties of intact prostate, may help to first discover which type of optical contrast exists between the adenocarcinoma and benign tissues in prostate at the intact real-time status. If the TRUS of the prostate can be augmented by such fundamental "optical" signatures for PCa, the likelihood that the biopsy of PCa will be image-targeted is greatly improved. The knowledge of intact optical properties of adenocarcinoma and benign tissues may also improve the pretreatment light dosimetry in phototherapy applications.

VII. CONCLUSION

This paper presented an overview of the current alternative technologies for prostate imaging, and demonstrated a transrectal dual-modality NIR diffuse optical tomography and ultrasonography-integrated method of detecting PCa. The technology of endorectally applied NIR diffuse optical tomography in combination with the conventional TRUS aims to characterize the spatially resolved optical properties of the *intact* prostate that

are known to have intraorgan and intersubject heterogeneities. A canine model of PCa using canine TVT was used to demonstrate the utility of this technology in detecting PCa. The tumors in the pelvic canal, including the prostate were found detectable at 2-week post-injection based upon the NIR absorption contrast, which was earlier than using NIR-reduced scattering and effective attenuation contrasts and US. Transrectal NIR tomography can potentially render pathognomic "optical" contrast information to the standard US of the prostate.

REFERENCES

- [1] American Cancer Society, *Cancer Facts & Figures 2009*. Atlanta: American Cancer Society, 2009.
- [2] H. Hricak, P. L. Choyke, S. C. Eberhardt, S. A. Leibel, and P. T. Scardino, "Imaging prostate cancer: A multidisciplinary perspective," *Radiology*, vol. 243, no. 1, pp. 28–53, 2007.
- [3] J. H. Pinthus, D. Pacik, and J. Ramon, "Diagnosis of prostate cancer," *Recent Results Cancer Res*, vol. 175, pp. 83–99, 2007.
- [4] J. L. Colli and C. L. Amling, "Exploring causes for declining prostate cancer mortality rates in the United States," *Urol. Oncol.*, vol. 26, no. 6, pp. 627–633, Nov./Dec. 2008.
- [5] S. M. Collin, R. M. Martin, C. Metcalfe, D. Gunnell, P. C. Albertsen, D. Neal, F. Hamdy, P. Stephens, J. A. Lane, R. Moore, and J. Donovan, "Prostate-cancer mortality in the USA and UK, in 1975–2004: An ecological study," *Lancet Oncol.*, vol. 9, no. 5, pp. 445–452, May 2008.
- [6] AUA, *The Management of Localized Prostate Cancer*. Orlando, FL: American Urologic Association, 2008.
- [7] H. B. Carter, "PSA scores: Should we use a lower threshold?," *Johns Hopkins Med. Lett. Health After 50*, vol. 17, no. 8, p. 6, 2004.
- [8] C. R. Porter, "Does the number of prostate biopsies performed affect the nature of the cancer identified?," *Nat. Clin. Pract. Urol.*, vol. 4, pp. 132–133, 2007.
- [9] R. Narayanan, P. N. Werahera, A. Barqawi, E. D. Crawford, K. Shinohara, A. R. Simoneau, and J. S. Suri, "Adaptation of a 3-D prostate cancer atlas for transrectal ultrasound guided target-specific biopsy," *Phys. Med. Biol.*, vol. 53, no. 20, pp. N397–N406, Oct. 2008.
- [10] The man, the gland, the dilemmas (2009, Mar. 31). *Wall Street J.* [Online]. Available: <http://online.wsj.com/article/SB123845699393571631.html>
- [11] A. C. Loch, A. Bannowsky, L. Baeurle, B. Grabski, B. König, G. Flier, O. Schmitz-Krause, U. Paul, and T. Loch, "Technical and anatomical essentials for transrectal ultrasound of the prostate," *World J. Urol.*, vol. 25, pp. 361–366, 2007.
- [12] A. M. Wise, T. A. Stamey, J. E. McNeal, and J. L. Clayton, "Morphologic and clinical significance of multifocal prostate cancers in radical prostatectomy specimens," *Urology*, vol. 60, pp. 264–269, 2002.
- [13] C. M. Coley, M. J. Barry, C. Fleming, and A. G. Mulley, "Early detection of prostate cancer. Part I: Prior probability and effectiveness of tests," *Amer. College Phys. Ann. Intern. Med.*, vol. 126, no. 5, pp. 394–406, 1997.
- [14] C. M. Moore, D. Pendse, and M. E. Medscape, "Photodynamic therapy for prostate cancer—A review of current status and future promise," *Nat. Clin. Pract. Urol.*, vol. 6, no. 1, pp. 18–30, 2009.
- [15] S. R. Davidson, R. A. Weersink, M. A. Haider, M. R. Gertner, A. Bogaards, D. Giewercer, A. Scherz, M. D. Sherar, M. Elhilali, J. L. Chin, J. Trachtenberg, and B. C. Wilson, "Treatment planning and dose analysis for interstitial photodynamic therapy of prostate cancer," *Phys. Med. Biol.*, vol. 54, no. 8, pp. 2293–2313, 2009.
- [16] M. Atri, M. R. Gertner, M. A. Haider, R. A. Weersink, and J. Trachtenberg, "Contrast-enhanced ultrasonography for real-time monitoring of interstitial laser thermal therapy in the focal treatment of prostate cancer," *Can. Urol. Assoc. J.*, vol. 3, no. 2, pp. 125–130, 2009.
- [17] R. Weiss, V. Egorov, S. Ayrapetyan, N. Sarvazyan, and A. Sarvazyan, "Prostate mechanical imaging: A new method for prostate assessment," *Urology*, vol. 71, no. 3, pp. 425–429, 2008.
- [18] V. Egorov, S. Ayrapetyan, and A. Sarvazyan, "Prostate mechanical imaging: 3-D image composition and feature calculations," *IEEE Trans. Med. Imag.*, vol. 25, no. 10, pp. 1329–1340, Oct. 2006.
- [19] K. Koenig, U. Scheipers, A. Pesavento, A. Lorenz, H. Ermer, and T. Senge, "Initial experiences with real time elastography guided biopsies of the prostate," *J. Urol.*, vol. 174, no. 1, pp. 115–117, 2005.

- [20] F. G. Mitri, B. J. Davis, M. W. Urban, A. Alizad, J. F. Greenleaf, G. H. Lischer, T. M. Wilson, and M. Fatemi, "Vibro-acoustography imaging of permanent prostate brachytherapy seeds in an excised human prostate—Preliminary results and technical feasibility," *Ultrasonics*, vol. 49, no. 3, pp. 389–394, 2009.
- [21] L. Zhai, V. Mouraviev, J. F. Madden, T. J. Polascik, and K. Nightingale, "Acoustic radiation force impulse (ARFI) imaging of human prostate in vivo," presented at the Focal Ther. Imag. Prostate Kidney Cancer, Amsterdam, Jun. 10–13, 2009.
- [22] A. Borsic, R. Halter, Y. Wan, A. Hartov, and K. D. Paulsen, "Sensitivity study and optimization of a 3-D electric impedance tomography prostate probe," *Physiol. Meas.*, vol. 30, no. 6, p. S1–S18, 2009.
- [23] R. J. Halter, A. Schned, J. Heaney, A. Hartov, S. Schutz, and K. D. Paulsen, "Electrical impedance spectroscopy of benign and malignant prostatic tissues," *J. Urol.*, vol. 179, no. 4, pp. 1580–1586, 2008.
- [24] J. Jossinet, E. Marry, and A. Matias, "Electrical impedance endotomography," *Phys. Med. Biol.*, vol. 47, no. 13, pp. 2189–202, 2002.
- [25] M. A. Yaseen, H. P. F. Brecht, S. A. Ermilov, R. R. Ghareeb, A. Conjusteau, and A. A. Oraevsky, "Hybrid optoacoustic and ultrasonic imaging system for detection of prostate malignancies," *Proc. SPIE*, vol. 6856, pp. 68560T-1–68560T-11, 2008.
- [26] V. G. Andreev, A. E. Ponomarev, P. M. Henrichs, M. Motamedi, E. Orihuela, E. Eyzaguirre, and A. A. Oraevsky, "Detection of prostate cancer with optoacoustic tomography," *Proc. SPIE*, vol. 4960, pp. 45–47, 2003.
- [27] A. Agarwal, S. W. Huang, M. O'Donnell, K. C. Day, M. Day, N. Kotov, and S. Ashkenazi, "Targeted gold nanorod contrast agent for prostate cancer detection by photoacoustic imaging," *J. Appl. Phys.*, vol. 102, pp. 064701-1–064701-4, 2007.
- [28] Y. Pu, W. B. Wang, B. B. Das, S. Achilefu, and R. R. Alfano, "Time-resolved fluorescence polarization dynamics and optical imaging of Cytate: A prostate cancer receptor-targeted contrast agent," *Appl. Opt.*, vol. 47, no. 13, pp. 2281–2289, 2008.
- [29] J. Boutet, L. Guyon, M. Debourdeau, J. M. Dinten, D. Vray, and P. Rizo, "Advances in bi-modal optical and ultrasound detection of prostate cancer diagnosis," *Proc. SPIE*, vol. 7171, pp. 71710E-1–71710E-6, 2009.
- [30] D. Piao, Z. Jiang, K. E. Bartels, G. R. Holyoak, J. W. Ritchey, G. Xu, C. F. Bunting, and G. Slobodov, "In vivo trans-rectal ultrasound-coupled near-infrared optical tomography of intact normal canine prostate," *J. Innovative Opt. Health Sci.*, vol. 2, no. 3, pp. 215–225, 2009.
- [31] A. A. Oraevsky, S. L. Jacques, and F. K. Tittel, "Measurement of tissue optical properties by time-resolved detection of laser-induced transient stress," *Appl. Opt.*, vol. 36, pp. 402–415, 1997.
- [32] Q. Chen, B. C. Wilson, S. D. Shetty, M. S. Patterson, J. C. Cerny, and F. W. Hetzel, "Changes in in vivo optical properties and light distributions in normal canine prostate during photodynamic therapy," *Radiat. Res.*, vol. 147, pp. 86–91, 1997.
- [33] W. H. Nau, R. J. Roselli, and D. F. Milam, "Measurement of thermal effects on the optical properties of prostate tissue at wavelengths of 1,064 and 633 nm," *Lasers Surg. Med.*, vol. 24, pp. 38–47, 1999.
- [34] L. K. Lee, C. Whitehurst, Q. Chen, M. L. Pantelides, F. W. Hetzel, and J. V. Moore, "Interstitial photodynamic therapy in the canine prostate," *Brit. J. Urol.*, vol. 80, pp. 898–902, 1997.
- [35] J. Jankun, L. Lilge, A. Douplik, R. W. Keck, M. Pestka, M. Szkudlarek, P. J. Stevens, R. J. Lee, and S. H. Selman, "Optical characteristics of the canine prostate at 665 nm sensitized with tin etiopurpurin dichloride: Need for real-time monitoring of photodynamic therapy," *J. Urol.*, vol. 172, pp. 739–743, 2004.
- [36] J. Jankun, R. W. Keck, E. Skrzypczak-Jankun, L. Lilge, and S. H. Selman, "Diverse optical characteristic of the prostate and light delivery system: Implications for computer modelling of prostatic photodynamic therapy," *Brit. J. Urol.*, vol. 95, pp. 1237–1244, 2005.
- [37] T. C. Zhu, S. M. Hahn, A. S. Kapatkin, A. Dimofte, C. E. Rodriguez, T. G. Vulcan, E. Glatstein, and R. A. Hsi, "In vivo optical properties of normal canine prostate at 732 nm using motexafin lutetium-mediated photodynamic therapy," *Photochem. Photobiol.*, vol. 77, pp. 81–88, 2003.
- [38] M. Solonenko, R. Cheung, T. M. Busch, A. Kachur, G. M. Griffin, T. Vulcan, T. C. Zhu, H. W. Wang, S. M. Hahn, and A. G. Yodh, "In vivo reflectance measurement of optical properties, blood oxygenation, and motexafin lutetium uptake in canine large bowels, kidneys, and prostates," *Phys. Med. Biol.*, vol. 47, pp. 857–873, 2002.
- [39] R. A. Weersink, A. Bogaards, M. Gertner, S. Davidson, K. Zhang, G. Netchev, D. J. Giewercer, J. Trachtenberg, and B. C. Wilson, "Optical delivery and monitoring of photodynamic therapy of prostate cancer," *Proc. SPIE*, vol. 5578, pp. 117–127, 2004.
- [40] L. Lilge, N. Pomerleau-Dalcourt, A. Douplik, S. H. Selman, R. W. Keck, M. Szkudlarek, M. Pestka, and J. Jankun, "Transperineal in vivo fluence-rate dosimetry in the canine prostate during SnET2-mediated PDT," *Phys. Med. Biol.*, vol. 49, pp. 3209–3225, 2004.
- [41] T. Svensson, S. Andersson-Engels, M. Einarsson, and K. Svanberg, "In vivo optical characterization of human prostate tissue using near-infrared time-resolved spectroscopy," *J. Biomed. Opt.*, vol. 12, pp. 014022-1–014022-10, 2007.
- [42] M. L. Pantelides, C. Whitehurst, J. V. Moore, T. A. King, and N. J. Blacklock, "Photodynamic therapy for localized prostatic cancer—Light penetration in the human prostate gland," *J. Urol. (Baltimore)*, vol. 143, no. 2, pp. 398–401, 1990.
- [43] H. J. Wei, D. Xing, B. H. He, R. H. Wu, H. M. Gu, G. Y. Wu, and X. M. Chen, "Absorption and scattering characteristics of human benign prostatic hyperplasia tissue with Ti: Sapphire laser irradiation in vitro," (in Chinese), *Guang Pu Xue Yu Guang Pu Fen Xi*, vol. 28, no. 1, pp. 10–13, 2008.
- [44] M. Essenpreis, "Thermally induced changes in optical properties of biological tissues," Ph.D. thesis, Univ. College London, London, 1992.
- [45] A. Roggan, K. Dörschel, O. Minet, D. Wolff, and G. Müller, "The optical properties of biological tissue in the near infrared wavelength range—review and measurements," in *Laser-induced Interstitial Thermotherapy*, G. Müller and A. Roggan, Eds.: Washington: SPIE Optical Engineering Press, 1995, pp. 10–44.
- [46] C. Whitehurst, M. L. Pantelides, J. V. Moore, P. J. C. Brooman, and N. J. Blacklock, "In vivo laser-light distribution in human prostatic carcinoma," *J. Urol. (Baltimore)*, vol. 151, no. 5, pp. 1411–1415, 1994.
- [47] L. K. Lee, C. Whitehurst, M. L. Pantelides, and J. V. Moore, "In situ comparison of 665 nm and 633 nm wavelength light penetration in the human prostate gland," *Photochem. Photobiol.*, vol. 62, no. 5, pp. 882–886, 1995.
- [48] L. K. Lee, C. Whitehurst, M. L. Pantelides, and J. V. Moore, "An interstitial light assembly for photodynamic therapy in prostatic carcinoma," *BJU Int.*, vol. 84, no. 7, pp. 821–826, 1999.
- [49] T. C. Zhu, A. Dimofte, J. C. Finlay, D. Stripp, T. Busch, J. Miles, R. Whittington, S. B. Malkowicz, Z. Tochner, E. Glatstein, and S. M. Hahn, "Optical properties of human prostate at 732 nm measured in mediated photodynamic therapy," *Photochem. Photobiol.*, vol. 81, no. 1, pp. 96–105, 2005.
- [50] T. C. Zhu, J. C. Finlay, and S. M. Hahn, "Determination of the distribution of light, optical properties, drug concentration, and tissue oxygenation in vivo in human prostate during motexafin lutetium-mediated photodynamic therapy," *J. Photochem. Photobiol. B*, vol. 79, no. 3, pp. 231–241, 2005.
- [51] R. A. Weersink, A. Bogaards, M. Gertner, S. R. H. Davidson, K. Zhang, G. Netchev, J. Trachtenberg, and B. C. Wilson, "Techniques for delivery and monitoring of TOOKAD_WST09-mediated photodynamic therapy of the prostate: Clinical experience and practicalities," *J. Photochem. Photobiol. B*, vol. 79, no. 3, pp. 211–222, 2005.
- [52] T. Svensson, E. Alerstam, M. Einarsson, K. Svanberg, and S. Andersson-Engels, "Towards accurate in vivo spectroscopy of the human prostate," *J. Biophoton.*, vol. 1, pp. 200–203, 2008.
- [53] J. Li and T. C. Zhu, "Determination of in vivo light fluence distribution in a heterogeneous prostate during photodynamic therapy," *Phys. Med. Biol.*, vol. 53, no. 8, pp. 2103–2114, Apr. 2008.
- [54] K. K. Wang and T. C. Zhu, "Reconstruction of in-vivo optical properties for human prostate using interstitial diffuse optical tomography," *Opt. Exp.*, vol. 17, no. 14, pp. 11665–11672, 2009.
- [55] Z. Jiang, D. Piao, G. Xu, J. W. Ritchey, G. R. Holyoak, K. E. Bartels, C. F. Bunting, G. Slobodov, and J. S. Krasinski, "Trans-rectal ultrasound-coupled near-infrared optical tomography of the prostate. Part II: Experimental demonstration," *Opt. Exp.*, vol. 16, no. 22, pp. 17505–17520, 2008.
- [56] M. Schweiger, S. R. Arridge, M. Hiroaka, and D. T. Delpy, "The finite element model for the propagation of light in scattering media: Boundary and source conditions," *Med. Phys.*, vol. 22, pp. 1779–1792, 1995.
- [57] H. Dehghani, B. Brooksby, K. Vishwanath, B. W. Pogue, and K. D. Paulsen, "The effects of internal refractive index variation in near infrared optical tomography: A finite element modeling approach," *Phys. Med. Biol.*, vol. 48, pp. 2713–2727, 2003.
- [58] X. Yu, G. Chen, and S. Cheng, "Dynamic learning rate optimization of the backpropagation algorithm," *IEEE Trans. Neural Netw.*, vol. 6, no. 3, pp. 669–677, May 1995.
- [59] B. Rivera, K. Ahrar, M. M. Kangasniemi, J. D. Hazle, and R. E. Price, "Canine transmissible venereal tumor: A large animal transplantable tumor model," *Comp. Med.*, vol. 55, no. 4, pp. 335–343, 2005.



Daqing Piao (S'03–M'03) received the B.Sc. degree in physics from Tsinghua University, Beijing, China, in 1990, the M.Sc. and Ph.D. degrees in biomedical engineering from the University of Connecticut, Storrs, in 2001 and 2003, respectively.

From 1990 to 1994, he was with the Guangdong Weida Medical Apparatus Group Corporation, Jiexi, China, where he was engaged in magnetic resonance imaging instrumentation. From 1994 to 1999, he was with Shanghai Kanglian Medical Engineering Corporation, Ltd., Shanghai, China, where he was engaged in biomedical applications of radio frequency and millimeter wave. He is currently an Assistant Professor of bioengineering with the School of Electrical and Computer Engineering, Oklahoma State University, Stillwater. His research interests include transrectal optical tomography for prostate cancer detection, investigating endoscopic tomography of hemodynamics, and developing alternating magnetic field device for magnetically activated nanothermal cancer therapy, which were funded by the Department of Defense Army Medical Research and Material Command, the Oklahoma Center for the Advancement of Science and Technology, and the National Institutes of Health, respectively. He has authored or coauthored around 30 papers published in various journals, and authored a chapter in the book *Translational Multimodality Optical Imaging* (Norwood, MA: Artech House, 2008).

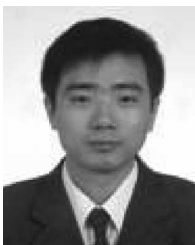
Prof. Piao is the Member of the Optical Society of America and the International Society of Optical Engineering. He received the FY2002 Predoctoral Traineeship Award from the Department of Defense (DOD) Breast Cancer Research Program and the FY2006 New investigator Award from the DOD Prostate Cancer Research Program.



Kenneth E. Bartels received the M.Sc. degree in veterinary surgery from Colorado State University, Fort Collins, in 1977, and D.V.M. degree from the College of Veterinary Medicine, Iowa State University, Iowa City, in 1973.

He is currently a Professor with the Department of Veterinary Clinical Sciences, Center for Veterinary Health Sciences, Oklahoma State University, Stillwater, where he is also the Director of the Biomedical Laser Laboratory and the McCasland Foundation Laser Surgery Professor. He is the Kerr Foundation Chair, where he is engaged in providing extended support for the Veterinary Center's Laser Laboratories. His research interests include lasers in veterinary surgery, laser/tissue interactions, and comparative medicine and surgery. He has authored or coauthored more than 75 peer-reviewed articles, seven book chapters, and edited one book involving surgery and the use of lasers in both humans and animals. He was with the U.S. Army Veterinary Corps for two years. He was with Army Reserve for 27 years, before retiring recently as a Colonel and Deputy Commander of the U.S. Army Veterinary Command.

Prof. Bartels is a Fellow of the American Society for Laser Medicine and Surgery.



Zhen Jiang received the B.Sc. degree in electronics and information technology and the M.Sc. degree in electromagnetism and microwave engineering from Southeast University, Nanjing, China, in 1998 and 2005, respectively. He is currently working toward a Ph.D. degree with the School of Electrical and Computer Engineering, Oklahoma State University, Stillwater.

From 1998 to 2005, he worked in a number of R&D projects in the telecommunication network and wireless fields. His current research interests include the instrumentation and application of transrectal near-infrared optical tomography in detecting prostate cancer. He has authored or coauthored six journal papers.

Mr. Jiang is a Student Member of Optical Society of America and the International Society of Optical Engineering.



Gilbert Reed Holyoak received the B.Sc. degree in animal science, the M.Sc. degree in animal reproduction from Brigham Young University, Salt Lake City, in 1983 and 1984, respectively, the D.V.M. degree in veterinary medicine from Washington State University, Pullman, in 1988, and the Ph.D. degree in veterinary science from the University of Kentucky, Lexington, in 1992.

From 1992 to 1999, he was a Research Assistant Professor and Assistant Professor in Department of Animal, Dairy, and Veterinary Sciences, Utah State University, Logan. Since 1999, he has been an Assistant Professor, an Associate Professor, and a Professor with the Department of Veterinary Clinical Sciences, Oklahoma State University, Stillwater. He has authored or coauthored more than 45 peer-reviewed articles, and written seven book chapters.

Prof. Holyoak is a Diplomat of American College of Theriogenologists.



Jerry W. Ritchey received the B.Sc. degree in microbiology and the Doctor of Veterinary Medicine degree from Oklahoma State University, Stillwater, in 1987 and 1991, respectively, and the Ph.D. degree in immunology from North Carolina State University, Raleigh, in 1997.

From 1991 to 1993, he was a Resident in anatomic pathology with the College of Veterinary Medicine, North Carolina State University. Since 1997, he has been a Faculty member in the Department of Veterinary Pathobiology, Oklahoma State University, Stillwater, where he is currently a Professor. He has authored or coauthored more than 48 peer-reviewed articles.

Dr. Ritchey is a Diplomat of American College of Veterinary Pathologists, a Member of the American Veterinary Medical Association, Phi Zeta, Sigma Xi, and has been twice recognized as a Regents' Distinguished Teacher.



Guan Xu received the B.Sc. degree in electrical engineering from Hebei University of Technology, Tianjin, China, in 2006. He is currently working toward the Ph.D. degree with the School of Electrical and Computer Engineering, Oklahoma State University, Stillwater, OK.

His current research interests include the algorithms and simulations of transrectal near-infrared optical tomography for prostate imaging. He has authored or coauthored four journal papers.

Mr. Xu is a Student Member of Optical Society of America and the International Society of Optical Engineering.



Charles F. Bunting (S'89–M'94) was born in Virginia Beach, VA, in 1962. He received the A.A.S. degree in electronics technology from Tidewater Community College, Virginia Beach, in 1985, and the B.S. degree in engineering technology from Old Dominion University, Norfolk, VA, in 1989, the M.S. and Ph.D. degrees in electrical engineering from Virginia Polytechnic Institute and State University (Virginia Tech), Blacksburg, in 1992 and 1994, respectively.

From 1994 to 2001, he was an Assistant/Associate Professor with the Department of Engineering Technology, Old Dominion University, where he worked with the NASA Langley Research Center on electromagnetic field penetration in aircraft structures and reverberation chamber simulation using finite-element techniques. In 2001, he was an Associate Professor in Oklahoma State University. He is currently the Director of the Robust Electromagnetics and Field Testing and Simulation Laboratory, School of Electrical and Computer Engineering, Oklahoma State University, Stillwater. His current research interests include emphasis on statistical electromagnetics, electromagnetic characterization and application of reverberation chambers, characterization of electromagnetic compatibility of telecommunications, electronics systems in aircraft and shipboard environments, computational electromagnetics as applied to biological sensors, and applied research in engineering education.



Gennady Slobodov received the B.Sc. degree in chemical engineering from the University of Oklahoma, Norman, OK, in 1996, and the M.D. degree from the University of Oklahoma Health Sciences Center, Oklahoma City, in 2000.

Since 2005, he has been an Assistant Professor with the Department of Urology, University of Oklahoma Health Sciences Center, where he was a resident in Urologic Surgery from 2000 to 2005. He has authored or coauthored six peer-reviewed papers in the *Journal of Biomedical Optics*, the *Journal of Innovative Optical Health Sciences*, the *Journal of Urology and Molecular Cancer*, is an invited lecturer, and has had numerous abstracts accepted and presented at National meetings. He has been a subinvestigator in seven National research studies.

Prof. Slobodov is board certified by the American Board of Urology and is a Member of the American Medical Association, the American Urological Association, the Southwest Oncology Group, the American Urogynecologic Society, the American Association of Clinical Urologists, the Endourological Society, the National Cancer Institute, the Oklahoma State Medical Association, the Oklahoma State Urological Association, the Society of Laparoendoscopic Surgeons, the South Central Section of the American Urological Association, the International Society for the Study of Women's Sexual Health, and the International Continence Society. He has been the recipient of numerous awards including National Institutes of Health Intramural Research Fellowship, the Engineering Undergraduate Research Fellowship, the Outstanding Sophomore in Chemical Engineering, the Golden Key National Honor Society, the National Engineering Honor Society, the Chemical Engineering Program of Excellence, the Boyd Gunning Scholar, the Alpha Lambda Delta Honor Society, and the President's Honor Roll.

International School for Junior Scientists and Students on Optics, Laser Physics and Biophysics

Saratov Fall Meeting

SFM'09September 21-24, 2009, Saratov,
Russia

Biophotonics / Internet Invited Lecture

IN VIVO OPTICAL ABSORPTION, REDUCED SCATTERING, AND EFFECTIVE ATTENUATION TOMOGRAPHY OF INTACT NORMAL AND CANCEROUS CANINE PELVIC CANAL INCLUDING THE PROSTATE

Daqing Piao, Zhen Jiang, Kenneth E. Bartels, G. Reed Holyoak, Jerry W. Ritchey, Guan Xu, Charles F. Bunting (all Oklahoma State University, Stillwater, Oklahoma, USA)
Gennady Slobodov (University of Oklahoma Health Sciences Center, Oklahoma City, Oklahoma, USA)

ABSTRACT

Spatially-resolved optical properties, including absorption coefficient, reduced scattering coefficient, and effective attenuation coefficient of the normal canine prostate and those from a dog with an induced canine prostate tumor model were assessed in vivo by trans-rectal ultrasound-coupled near-infrared optical tomography at 840nm. Three optical properties were reconstructed from steady-state measurements using a model-based iterative approach. Normal prostatic tissues revealed much greater intra-organ and inter-subject heterogeneity for reduced scattering and effective attenuation coefficients compared to the absorption coefficient. Such tissue heterogeneities correlated well with the fact that tumor growth in the pelvic canal, including tumors in the prostate, were detectable earlier using NIR absorption contrast than with using NIR reduced scattering and effective attenuation contrasts by themselves. Results suggest that an earlier diagnosis of prostatic cancer than is currently available is possible using this novel imaging approach.

**JOINT POSTER SESSION AND INTERNET DISCUSSION, Building 3, 3rd floor &
Room 57, 2009-09-23 18:00**

Representing Author:

, Oklahoma State University, Assistant Professor (Stillwater, Oklahoma, USA)

This page was accessed **102** times.

Photon Diffusion Associated with a Cylindrical Applicator Boundary for Axial Trans-luminal Optical Tomography: Experimental Examination of the Steady-State Theory

Anqi Zhang,¹ Daqing Piao,^{1*} Gang Yao,² Brian W. Pogue³

¹*School of Electrical and Computer Engineering, Oklahoma State University, Stillwater, OK 74078, USA*

²*Department of Biological Engineering, University of Missouri, Columbia, MO, 65211, USA*

³*Thayer School of Engineering, Dartmouth College, Hanover, NH, 03755, USA*

*Corresponding Author: daqing.piao@okstate.edu

Abstract: A new approach for steady-state photon diffusion modeling associated with a cylindrical applicator boundary for trans-luminal optical tomography was evaluated numerically and experimentally. In the diffusion regime the theoretical predictions agree well with experimental findings.

©2010 Optical Society of America

OCIS codes: (170.3660) Light propagation in tissues; (170.5280) Photon migration; (170.6960) Tomography

1. Introduction

Using near-infrared (NIR) light to image deep tissue volumes non-invasively has largely been based upon transport modeling with the diffusion approximation to the radiative transport equation [1]. The photon diffusion in a medium enclosed by a circular cylindrical applicator has been analyzed previously in two elegant studies [2, 3]. The analytic results of these studies, however, were not in an explicit format that could guide the data calibration, and it has also been difficult to assess from these results how much the circular applicator boundary affects the photon diffusion when compared with the more studied semi-infinite boundary. Recent work by our group [4] has investigated the photon diffusion theory as applied to the geometries corresponding to an external ring-structure applicator or an internal cylinder probe, which leads to analytic solutions of the photon diffusion in a homogenous medium bounded externally or internally by an infinitely long circular cylindrical applicator. These analytic solutions can be further developed into the form that includes an isotropic “physical” source & its image source, with respect to a semi-infinite boundary that is tangential to the circular boundary at the location of directional physical source. As well, there is a radial-dependent term that approaches unity as the circular cylindrical geometry reaches semi-infinite case. Given that this theory qualitatively makes sense, the current paper attempts to confirm that the theory matches experimental data. Initial experimental work was conducted along the azimuthal plane of the cylindrical boundary, corresponding to a “convex” axial-imaging application, like that used in trans-luminal diffuse optical tomography.

2. Analytic Approach and Its Numerical Evaluations

Using the modified Bessel functions of the 1st and 2nd kind, the cylindrical-coordinate solution of the steady-state photon fluence rate in a concave geometry for an infinitely long circular cylindrical applicator with radius R_0 , is [4]:

$$\Psi = \frac{S}{2\pi^2 D} \int_0^\infty dk \left\{ \cos[k(z-z')] \sum_{m=0}^\infty \varepsilon_m I_m[k_{eff}(R_0 - R_a)] K_m[k_{eff} R_0] \left(1 - \frac{I_m(k_{eff} R_0)}{K_m(k_{eff} R_0)} \frac{K_m[k_{eff}(R_0 + R_b)]}{I_m[k_{eff}(R_0 + R_b)]} \right) \cos[m(\varphi - \varphi')] \right\} \quad (1\text{-conc})$$

This latter geometry is commonly seen when the sources and detectors are on the exterior of the cylindrical volume. Similarly, the cylindrical-coordinates solution of the steady state photon fluence rate in a convex geometry imposed by an infinitely long circular cylindrical applicator with radius R_0 , as seen in trans-rectal prostate imaging, is [4]:

$$\Psi = \frac{S}{2\pi^2 D} \int_0^\infty dk \left\{ \cos[k(z-z')] \sum_{m=0}^\infty \varepsilon_m I_m(k_{eff} R_0) K_m[k_{eff}(R_0 + R_a)] \left(1 - \frac{K_m(k_{eff} R_0)}{I_m(k_{eff} R_0)} \frac{I_m[k_{eff}(R_0 - R_b)]}{K_m[k_{eff}(R_0 - R_b)]} \right) \cos[m(\varphi - \varphi')] \right\} \quad (1\text{-conv})$$

where in both (1-conc) and (1-conv) Ψ is the photon fluence rate at position (R_0, φ', z') with source at (R_0, φ, z) , $D = [3(\mu_a + \mu'_s)]^{-1}$ is the diffusion coefficient with μ'_s being the reduced or transport scattering coefficient, μ_a is the absorption coefficient, S is the source term, $R_b = 2AD$, $R_a = 1/\mu'_s$ and A is a constant depending on the relative refractive index mismatch between cylindrical applicator and tissue.

For a cylindrical applicator, a virtual “semi-infinite” image source can be introduced, as shown in Fig. 1(a) for “concave” geometry and in Fig. 1(b) for “convex” geometry. The virtual “semi-infinite” image source is defined as the image of the equivalent isotropic source of the physical source with respect to the semi-infinite boundary that is tangential to the circular boundary at the location of the physical source. Using the asymptotic expressions of the

modified Bessel functions, one can have $\Psi_{imag}^{ph} = \Psi_{imag}^{semi} \cdot \sqrt{(R_0 + R_a + 2R_b)/(R_0 - R_a)}$ for concave geometry and $\Psi_{imag}^{ph} = \Psi_{imag}^{semi} \cdot \sqrt{(R_0 - R_a - 2R_b)/(R_0 + R_a)}$ for convex geometry, where Ψ_{imag}^{ph} is the fluence rate associated with the image of the isotropic source with respect to the actual circular boundary, and Ψ_{imag}^{semi} is the fluence rate associated with the virtual “semi-infinite” image source. Then for a source-detector separation of l , (1-conc) and (1-conv) can be converted to the spherical-coordinate forms, given as:

$$\Psi = \frac{S}{4\pi D} \frac{e^{-k_0 l_r}}{l_r} - \frac{S}{4\pi D} \frac{e^{-k_0 l_i}}{l_i} \sqrt{\frac{R_0 + R_a + 2R_b}{R_0 - R_a}} \quad \Psi = \frac{S}{4\pi D} \frac{e^{-k_0 l_r}}{l_r} - \frac{S}{4\pi D} \frac{e^{-k_0 l_i}}{l_i} \sqrt{\frac{R_0 - R_a - 2R_b}{R_0 + R_a}} \quad (2)$$

both of which asymptotically approach the solution for a semi-infinite boundary as the radius of the applicator R_0 becomes infinity

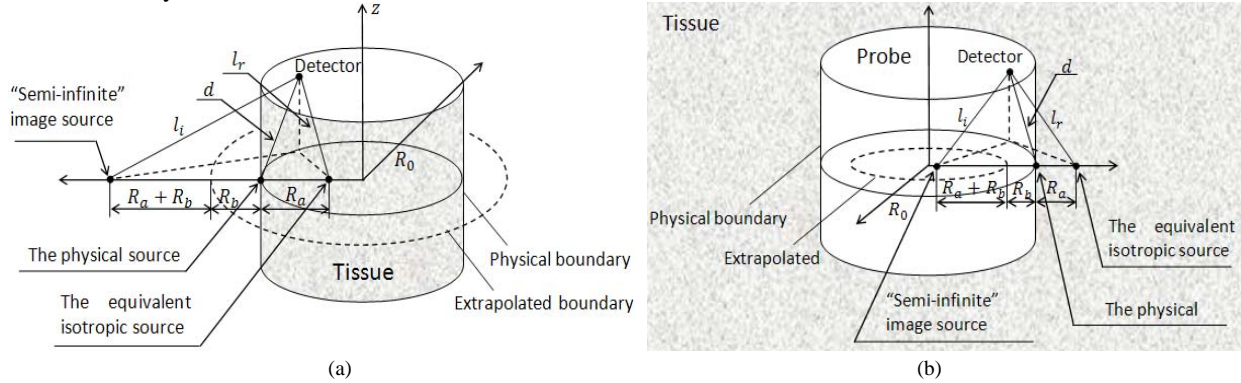


Figure 1. Details of the cylindrical boundary geometry indicating the equivalent isotropic source, the extrapolated boundary, and the virtual “semi-infinite” image source. (a) Concave geometry (b) Convex geometry.

The original form of the analytic solution in (1-conc) and (1-conv) are evaluated numerically for the specific geometries of having the source and the detector on the surface positioned only along the azimuthal or the longitudinal directions. Placing the source-detector either azimuthally or longitudinally helps demonstrate explicitly the effect of the applicator curvature shape, either concave or convex, and the radius of the applicator curvature on the decay of photon fluence rate as a function of the source-detector distance, in comparison to that in the semi-infinite geometry. In both (1-conc) and (1-conv), for sufficiently large k , hence large k_{eff} [4], the modified Bessel functions in the integrands approach their asymptotic expressions which drop to zero. Therefore the contribution of the integrands associated with k greater than a certain limit can be neglected. According to the IEEE standard for floating-point arithmetic [5], there is a limit for the biggest number and the smallest number to be stored in computer. In Matlab the criterion [6] for overflow is 1.7977×10^{308} in decimal, and for underflow is 2.2251×10^{-308} . In (1-conc) and (1-conv), the modified Bessel function of the 1st and 2nd kinds are exponentially growing and decaying functions, respectively, for which overflow will readily occur for a large order m and underflow for a large argument k . A strategy of “pre-enlarge” and “pre-reduce” is implemented, based on the principle that before evaluating each modified Bessel function individually, the modified Bessel function of the 1st kind is “pre-reduced” for large order m and the modified Bessel function of the 2nd kind is “pre-enlarged” by the same degree, by which the product of each pair remains unchanged. Additionally, it is also found in (1-conc) and (1-conv) that the radius R_0 has a great effect on the evaluation outcome. When R_0 is as large as $8cm$ as an instance in (1-conc), for $k = 40$, the integrand does not converge sufficiently even for summing m up to 500, but for a smaller radius $R_0 = 1cm$, the same integrand converges quickly at $m = 100$. A method of “repeated averaging” is thus employed to improve the convergence when computing the integrand. The principle is to first examine if the integrand presents an oscillating pattern. If there is an oscillation, the envelop-profile of the maxima and minima of the oscillation is implemented to form a finite converging alternative series, and the last series of maxima and minima are averaged to get the value of the integrand. If not, the last result is chosen as the value of the integrand.

These numerical techniques were implemented to evaluate the analytic solutions given in (1), to examine if the theoretical predictions agree with experimental findings.

3. Experimental Examination

The initial experimental examinations were conducted for the “convex” cylinder geometry only. The experimental setup is shown in Fig. 2(a). A 0.5% bulk Intralipid solution was used as the diffusive medium. The cylinder probe was made of black acetal. In terms of the A parameter in diffusion approximation, a value of 2.82 is often assigned for a tissue-air interface [7][8], which is less-likely to be true for the cylinder probe material and the probing

geometry used in this study. To determine the A value associated with the cylinder material, we used both an infinite geometry to determine the optical properties of the Intralipid medium and a semi-infinite geometry using a material identical to that of the cylinder probe to determine A , based on the well-known semi-infinite theory. It was found that $A = 1.86$.

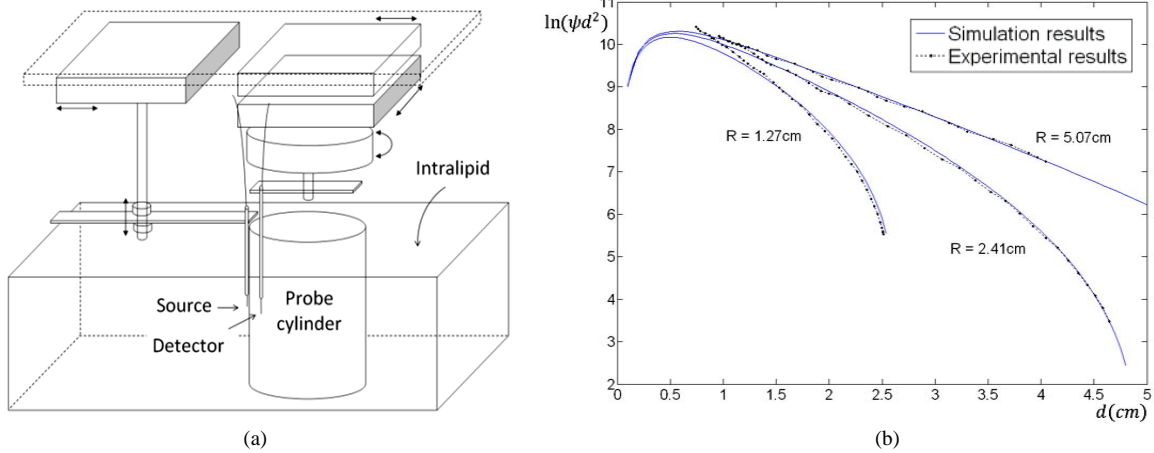


Figure 2. System diagram for the convex geometry experiments (a) and the experimental results (b)

The experimental data were compared in Fig. 2(b) with the numerical evaluations based on (1-conv), which corresponded to photon diffusion in a homogenous medium bounded internally by a cylindrical probe that was infinitely long, not as the finite-length probe used in experiments. The optical properties of the medium were $\mu_a = 0.025\text{cm}^{-1}$, $\mu_s' = 5\text{cm}^{-1}$ and $A = 1.86$. The results in Fig. 2 (b) indicated that: (1) As the radius R increases, the photon diffusion gradually reached that in a semi-infinite medium (a straight-line in Fig. 2(b)); (2) At larger source-detector separation that renders valid diffusion process, the theory accurately predicted the change of the photon fluence rate versus the source-detector distance and versus the boundary radius; (3) At smaller source-detector separation, which shall be in non-diffuse regime, the theoretical prediction was inaccurate as expected.

4. Discussions and Future Work

Experimental work were conducted to examine the predictions based on the theory derived for photon diffusion associated with an infinitely-long cylindrical applicator for axial trans-luminal optical tomography. For finite-length applicator, the theory could be improved by considering the effects of two longitudinal boundaries. The experimental results, however, demonstrate that the current theory may be sufficiently accurate in the diffusion regime. Our future plans include experimental examinations with a “concave” cylinder probe applicable to external imaging, to further simplify the theory into a closer form to the well-known logarithm-form of the semi-infinite geometry, and to amend the experimental examinations with Monte Carlo methods.

Acknowledgement: This work has been supported in part by a research grant HR06-171 from the Oklahoma Center for the Advancement of Science and Technology (OCAST), a Big-XII Faculty fellowship awarded to Daqing Piao, and the Prostate Cancer Research Program of Department of Defense through a grant #W81XWH-07-1-0247.

References

1. A. Ishimaru, “Diffusion of light in turbid material,” *Appl. Opt.*, 28, 2210—2215 (1989).
2. S.R. Arridge, M. Cope, D.T. Delpy, “The theoretical basis for the determination of optical pathlengths in tissue: temporal and frequency analysis,” *Phys Med Biol.*, 37(7):1531-60 (1992).
3. B.W. Pogue, and M.S. Patterson, “Frequency-domain optical absorption spectroscopy of finite tissue volumes using diffusion theory,” *Phys Med Biol.*, 39(7):1157-80 (1994).
4. Zhang A, Piao D, Yao G, Bunting CF, Krasinski JS, Pogue BW, “Forward modeling of axial trans-luminal diffuse optical imaging with a cylindrical applicator using continuous-wave photon-illumination,” *International Symposium on Biomedical Optics*, San Jose, CA, Jan. 24-29, 2009. *Proceedings of SPIE*, Vol. 7174, Paper #717404.
5. IEEE 754-2008 Standard for Floating-Point Arithmetic, IEEE, Aug 2008
6. Moler, C., “Floating points: IEEE Standard unifies arithmetic model.” *Cleve's Corner*, The MathWorks, Inc., 1996.
7. B. W. Pogue, S. Geimer, T. O. McBride, S. Jiang, U. L. Osterberg, and K. D. Paulsen, “Three-dimensional simulation of near-infrared diffusion in tissue: boundary condition and geometry analysis for finiteelement image reconstruction,” *Appl. Opt.* 40, 588-600 (2001).
8. Xu G, Piao D, Musgrove CH, Bunting CF, Dehghani H, “Trans-rectal ultrasound-coupled near-infrared optical tomography of the prostate Part I: Simulation,” *Optics Express*, Vol. 16, Iss. 22, pp. 17484–17504 (2008).

FPGA-Assisted Strategy toward Efficient Reconstruction (FAStER) in Diffuse Optical Tomography

Yuanyuan Jiang, Sovanlal Mukherjee, James E. Stine, Charles F. Bunting, Daqing Piao*

School of Electrical and Computer Engineering, Oklahoma State University, Stillwater, OK, 74078, USA

Corresponding author: daqing.piao@okstate.edu

Abstract: The finite-element computation of photon fluence and adjoint photon fluence necessary to image reconstruction in steady-state DOT has been implemented on field-programmable-gate-array (FPGA). Preliminary results encourage further exploration toward efficient DOT image reconstruction using FPGA.

©2010 Optical Society of America

OCIS codes: (170.6960) Tomography; (170.3010) Image reconstruction techniques.

1. INTRODUCTION

Diffuse optical tomography (DOT) utilizes near-infrared (NIR) light to interrogate biological tissues at a depth up to several centimeters to recover the distribution of internal optical properties based on boundary measurements. The image reconstruction of DOT is most often rendered by diffusion-model-based forward computation and iterative non-linear optimization [1], which is inevitably computationally expensive. Consequently, using application-specific computer architecture to accelerate the DOT computation becomes attractive. A number of computer architectures useful for accelerating the data acquisition and processing in optical imaging have been demonstrated recently. Examples include using field-programmable gate array (FPGA) technology to accelerate raw data processing in optical imaging [2, 3], using FPGAs or graphic processing units (GPUs) to accelerate Monte Carlo computation of photon migration [4-6], using FPGAs to solve partial differential equations (PDEs) governing heat transfer [7] or wave propagation [8], and using GPU to perform finite-element-method (FEM) computation [9].

In this work the FEM solution to photon diffusion in biological tissue is implemented using an FPGA. The FPGA executes conjugate gradient (CG) solver of 12 linear equations formulated in an FEM framework, which are associated with 6 sources and 6 detectors, for computing the photon fluence rate and the adjoint fluence rate. Preliminary results demonstrate that a lower-end FPGA outperforms a higher-end PC in CG-based solution of the 12 linear equations, thereby encouraging further exploration toward efficient DOT image reconstruction using FPGA.

2. METHOD AND MATERIALS

2.1 Development of an open-code FEM-based forward solver for steady-state diffuse optical tomography

Implementing the DOT image reconstruction routine in FPGA requires an algorithm architecture that is transparent to FPGA. An open-code forward FEM solver for steady-state DOT reconstruction is developed. The solver is based on the steady-state photon diffusion equation [1] $\nabla \cdot \kappa(\vec{r}) \nabla \Phi(\vec{r}) - \mu_a(\vec{r}) \cdot \Phi(\vec{r}) = -q(\vec{r})$ (where μ_a is the absorption coefficient, κ is the diffusion coefficient, Φ is the photon fluence rate at position \vec{r} , and q is the source at \vec{r}), and the boundary condition [1] of $\Phi(\vec{r}_\Omega) + 2A\kappa\hat{n} \cdot \nabla \Phi(\vec{r}_\Omega) = 0$ (where \vec{r}_Ω corresponds the point on the boundary, \hat{n} is a unit vector pointing outward (from the tissue to probe) and normal to the tissue-probe interface, and A is the boundary mismatch factor determined by the relative refractive indices of the tissue domain and the probe (air) domain). These equations formulate into the FEM framework $[K(\kappa) + C(\mu_a) + B/(2A)]\Phi = Q_0$, where the K , C and Q are volume integrals of each element with regard to κ , μ_a and q , and B is the surface integral of the boundary element. The FEM forward solver results in a set of linear equations containing sparse matrices. The inverse problem performs a non-linear optimization of the objective function of $b = \|\Phi_{\text{measurement}} - \Phi_{\text{estimation}}\|$ by updating the pixel or voxel-wise values of κ and μ_a . The inverse solver requires finding $\partial\Phi/\partial\kappa$ and $\partial\Phi/\partial\mu_a$, which are integrated into the forward computation process by using the adjoint method of deriving the Green's function associated with an impulse source at the detector position, as shown in Fig. 1(a) (b). Therefore, the number of sources, s , and the number of detectors, s generate $2s$ sets of linear equations for solving by the CG method.

Our open-code FEM-solver is developed in MATLAB (Mathworks, Inc. Natick, MA) platform. A comparison of our solver with the NIRFAST package [10] is given in Fig. 1(c), where the target has an absorption coefficient of 0.02 mm^{-1} and a reduced scattering coefficient of 1.2 mm^{-1} , in a background of 0.002 mm^{-1} absorption and 0.8 mm^{-1} reduced scattering. The performance of our solver is comparable to that of NIRFAST, at the same 1% noise-level.

2.2 Implementation of the conjugate gradient solution of the linear equations in FPGA

The FPGA implementation of the linear equations for DOT forward computation is composed of four modules. The calculation module, which includes two floating point adders and two floating point multipliers, is capable of two simultaneous floating point vector operations with an approximately throughput of four floating point operations per clock cycle. The memory modules utilize on-chip block memory. And the sparse FEM matrix is stored by compressed row storage (CRS) [11]. The DOT sources are considered Gaussian and the adjoint sources are impulse, which also lead to sparse structure.

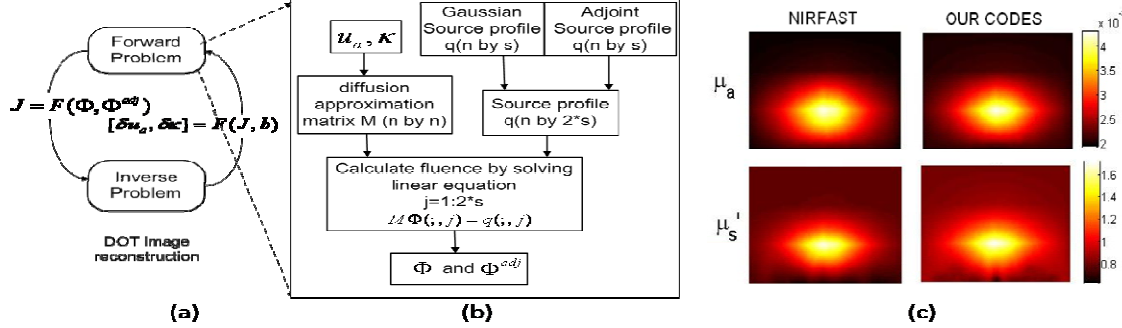


Fig.1 (a) Flow chart for DOT reconstruction (b) Forward problem (c) DOT image reconstructed by NIRFAST and our codes

We have temporarily used the RS232 protocol for the data transfer between the FPGA and PC (shown in Fig. 2). We have also temporarily implemented only the forward computation in FPGA, and performed the inverse solver algorithm on a PC. The control module, which is a finite state machine (FSM), controls the data flow in forward computation, as shown in Fig. 3. The data flow starts from loading FEM matrix from PC and then clears all the intermediate memories. The source profile is restored as originally vector sequence according to the address offset and address index. At the same time, the initial calculation of residual norm, or α_0 , which is out of the CG loop, is calculated. Then it enters the CG iteration and three states, updates α , β , and Φ , runs iteratively until α_0 is below a threshold. Then the FSM jumps out of the CG iteration, sends the computed fluence to PC, clears the state, and loads the next source or adjoint source profiles. The complete fluence data set are transferred to PC for running the inverse solver that leads to a new set of FEM matrices for being transferred to FPGA for the next iteration.

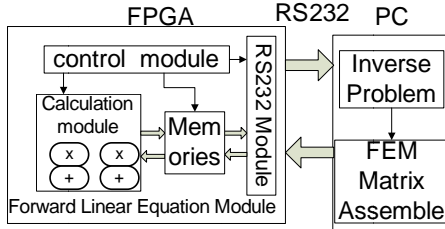


Fig.2. System sketch

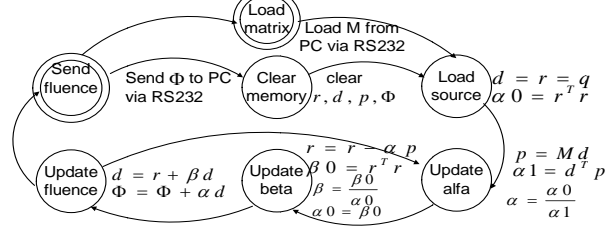


Fig.3 Control flow (finite state machine)

3. RESULTS AND DISCUSSIONS

The FEM solver is implemented on PC only and on FPGA-PC unit as specified above for comparison of the speed. On PC, the FEM-solver is executed on an Intel® quad-core 2.33 GHz processor. The linear equation is solved by using “bicgstab” function in Matlab with the FEM matrix being specified as sparse, which means the nonzeros in the matrix are stored together in main memory and the low spacial-locality caused by the zeros in sparse matrix is solved. A 2-D mesh with 1,705 nodes and 11,593 non-zeros in the corresponding FEM matrix, for an imaging dimension of 54mm×30 mm with 6 sources and 6 detectors on the boundary, is generated for DOT image reconstruction. The background is set at absorption coefficient of 0.01mm^{-1} and reduced scattering of 1mm^{-1} , with a target of 0.025mm^{-1} absorption and 1.75mm^{-1} reduced scattering. A Xilinx VirtexII Pro FPGA (XC2VP30 Package ff896 Speed Grade -7) is used, which contains 30,816 logic cells, 136 18×18 multipliers and 2,448 Kbits of Block RAM [12] with maximum clock frequency of 150MHz (the actual clock frequency being used is 100MHz). The execution speeds of PC-only and FPGA-PC unit, both in IEEE 754R double precision, are given in Fig. 4 (red and blue bars). The bars #1 and #2 correspond to CG algorithms with 50 and 100 iterations, respectively, for a 1705×1705 matrix. The bars #3 correspond to solving one above-mentioned FEM-associated linear equation. The bars #4 correspond to one complete forward computation of solving 12 linear equations. For each group of the bars, there are two FPGA-runtime settings. The “one-instance” corresponds to using 32 out of 136 on-board DSP modules that is necessary to computing the linear equation one by one, and the “two-instances” corresponds to using 64 out

of 136 on-board DSP modules to compute two linear equations simultaneously. Compared with PC running time, there is a 1.8 folds and 3.6 folds of speed improvements with the “1-instance” and “2-instances”, respectively. The 136 DSP modules ideally allow simultaneous computation of 4 linear equations that could lead to 7.2 folds of speed improvement at the given clock frequency, but the insufficient on-chip memory has limited implementing more than 64 DSP modules for this study. The images reconstructed by PC only and by FPGA-PC unit are compared in Fig. 5.

It is noted that the FPGA used in this study is a low-end sample unit with limited on-board resources. Using high-end FPGAs with more on-board resources could further speed up the above computations. Higher-end FPGAs such as Virtex 5 and Virtex 6 families has more DSP resources which accommodate 25×18 instead of 18×18 multipliers, thereby could further improve the speed. Table 1 lists the performance improvement that could be expected, with the present study listed as the first one, by using the existing higher-end FPGAs.

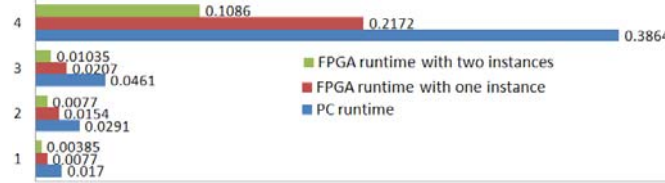


Fig.4. Runtime comparison between FPGA and PC

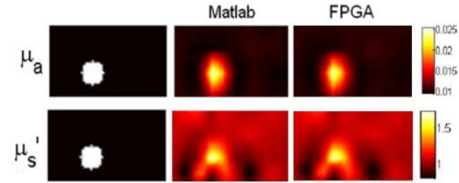


Figure 5. Images reconstructed by PC and using FPGA

Table 1 FPGA performance improvement achieved by different FPGA

FPGA	VirtexII Pro XC2VP30 (136 18×18 DSPs)		VirtexII Pro XC2VP100 (444 18×18 DSPs)	Virtex 5 XC5VSX240T (1056 25×18 DSPs)	Virtex6 VSX475T (2016 25×18 DSPs)
	100M, 1 instance	150M, 4 instances	150M 12 instances	150M 40 instances	150M 76 instances
Speedup	1.8 folds	10.8 folds	32.4 folds ^{*(1)}	108 folds ^{*(2)}	205.2 folds ^{*(3)}

^{*(1)} the maximum speed improvement for system employs 6 detectors and 6 sources

^{*(2)} the expected speed improvement for a DOT geometry with 20 detectors and 20 sources

^{*(3)} the expected speed improvement for a DOT geometry with 38 detectors and 38 sources

The use of RS232 protocol in this initial study has resulted in overall slower DOT iteration due to the initial and final data transmissions between the FPGA and PC. There are a number of approaches to improve the overall performance, including implementing a real-time data transmission protocol such as USB or Ethernet, developing a stand-alone on-board operating system, and performing both the forward and inverse solver algorithms on the FPGA.

4. CONCLUSION AND FUTURE DIRECTION

In summary, FPGA implementation of FEM based forward computation for steady-state DOT is demonstrated. For a system employing 6 sources and 6 detectors with a mesh having 1,705 nodes, forward computations involving 12 linear equations solved by CG method are performed by FPGA. The preliminary results, even though hindered by the slow RS232 data transfer protocol and limited resources on the FPGA, encourage implementing complete forward and inverse iteration on FPGA for efficient reconstruction.

Acknowledgement: This work has been supported by Oklahoma Center for the Advancement of Science and Technology (OCAST) (HR06-171), and DOD Prostate Cancer Research Program (#W81XWH-07-1-0247).

REFERENCES

- [1] Arridge SR, "Optical tomography in medical imaging," Invers. Prob. 15, R41-R93 (1999).
- [2] Browne TA, Condell JV, Prasad g, McGinnity TM, "An investigation into optical flow computation on FPGA hardware," Proc. Inter. Machine Vis. Image Process. Conf., pp.176-181 (2008).
- [3] Watt D, Harmon K, Srivastava A, Faris GW, "High speed processing of frequency domain images," in Biomedical Optics, OSA Technical Digest (CD) (Optical Society of America, 2008), page BWG3.
- [4] Lo WC, Redmond K, Luu J, Chow P, Rose J, Lilje L, "Hardware acceleration of a Monte Carlo simulation for photodynamic therapy treatment planning," J. Biomed. Opt., 14(1), 014019 (2009).
- [5] Alerstam E, Svensson T, Andersson-Engels S, "GPU-Based Monte Carlo Simulations of Photon Migration in Heterogenous Materials," European Conf. Biomed. Opt., pp. 14-18 (2009).
- [6] Fang Q, Boas DA, "Monte Carlo Simulation of Photon Migration in 3D Turbid Media Accelerated by Graphics Processing Units." Opt. Express, 17(22), pp. 20178-20190 (2009).
- [7] Pardo E, Lopez R, Cabello D, Balsi M, "FPGA finite difference time domain solver for thermal simulation," Inter. Conf. Field Program. Logic Appl., pp. 721-722 (2005).
- [8] Gibbons JA, Howard DM, Tyrrell AM, "FPGA implementation of 1D wave equation for real-time audio synthesis," IEE proceedings: Comp. Digital Tech., 152, pp. 619-631 (2005).
- [9] Goddeke D, "Accelerating Double Precision FEM simulations with GPUs," Simul. Tech. 18th Sympos. (ASIM), 139-144(2005).
- [10] Dehghani H, Eames ME, Yalavarthy PK, Davis SC, Srinivasan S, Carpenter CM, Pogue BW, Paulsen KD, "Near infrared optical tomography using NIRFAST: Algorithms for numerical model and image reconstruction algorithms," Commun. Num. Meth. Engi., DOI: 10.1002/cnm.1162 (2008)
- [11] DeLorimier M, DeHon A, "Floating-point sparse matrix-vector multiply for FPGAs," Proc. Inter. Symp. FPGA, 75-78 (2005).
- [12] Xilinx, Xilinx University Program Virtex-II Pro Development System: Hardware Reference Manual, March, 2005.

Trans-rectal ultrasound-coupled spectral optical tomography at 785nm and 830nm detects elevation of total hemoglobin concentration in canine prostate associated with the development of transmissible venereal tumors

Zhen Jiang,¹ Kenneth E. Bartels,² G. Reed Holyoak,² Jerry W. Ritchey,³ Jerzy S. Krasinski,¹
Charles F. Bunting,¹ Gennady Slobodov,⁴ Daqing Piao^{1*}

1. School of Electrical and Computer Engineering, Oklahoma State University, Stillwater, Oklahoma, U.S.A.

2. Department of Veterinary Clinical Sciences, Oklahoma state University, Stillwater, Oklahoma, U.S.A.

3. Department of Veterinary Pathobiology, Oklahoma state University, Stillwater, Oklahoma, U.S.A.

4. Department of Urology, University of Oklahoma Health Sciences Center, Oklahoma City, Oklahoma, U.S.A.

* Correspondence: Email: daqing.piao@okstate.edu

Abstract: Spectral trans-rectal ultrasound-coupled optical tomography at 785nm and 830nm has revealed non-invasively longitudinal elevation of total hemoglobin concentration associated with development of transmissible venereal tumors in canine prostate over a 6-week time-course.

©2010 Optical Society of America

OCIS codes: (170.3880) Medical and biological imaging; (170.6960) Tomography; (170.7230) Urology; (170.1610) Clinical applications.

1. Introduction

Prostate cancer is the leading cause of death in American men. Since its introduction [1, 2], trans-rectal ultrasound (TRUS) guided biopsy has evolved to become a standard procedure used in prostate cancer diagnosis when indicated by elevated serum prostate-specific antigen (PSA) levels or abnormal digital rectal examination (DRE). However, TRUS of the prostate has limitations. The ultrasonographic finding of the classic hypoechoic peripheral zone lesion has a sensitivity of 85.5%, specificity of 28.4%, positive predictive value of 29%, negative predictive value of 85.2% and overall accuracy of 43% [3] in prostate cancer detection. The prevalence of isoechoic or nearly invisible prostate cancers visualized with TRUS ranges from 25 to 42% [4]. As a result, the overall cancer detection rates for patients undergoing repeat prostate needle biopsy with various biopsy templates range from 10% - 38% [5]. Improving the cancer detection rate using TRUS-guided biopsy requires TRUS imaging be augmented or aided with a potentially pathognomonic indicator of prostate cancer development that can be detected non-invasively.

Recently there have been several approaches utilizing endogenous [6] or exogenous [7] near-infrared (NIR) absorption of the tissue to assist detecting prostate cancer. We have developed a TRUS-coupled NIR optical tomography probe, and with which the development of a transmissible venereal tumor (TVT) within the canine prostate was detected *in vivo* [8]. In that study, the optical information aiding TRUS was the NIR absorption and reduced scattering of the prostatic tissue at a single wavelength of 840nm. The tumor progression was associated with significant elevation of the NIR absorption earlier in the tumor development, and heterogeneous/moderate elevation of NIR reduced scattering that was resolved later than the NIR absorption at that wavelength. The significant elevation of NIR attenuation, as a result of combined absorption and reduced scattering elevations, in the tumor has been attributed partially to substantially denser cellular structure and morphology changes at sub-cellular level that could increase the NIR attenuation cross-sections. However, as the tumor aggression is associated with angiogenesis [9], the elevation of the total hemoglobin concentration ([HbT]) could have been observed in that study if we had had the capability of spectral optical tomography in a band covering the isosbestic point of hemoglobin.

Based on this hypothesis, we have upgraded our trans-rectal NIR tomography system to spectroscopic detection, at dual-bands of 785nm and 830nm only. Although it is theoretically feasible to quantify both hemoglobin concentration and oxygen saturation using these two bands, providing that the absorptions by other chromophores could be neglected in these bands, it has been reported that the accuracy of oxygen saturation based on only these two bands or in their vicinity is limited [10]. We therefore have focused on quantifying the [HbT] only, in the prostatic tissue. This study is the first demonstration of non-invasive optical tomographic detection of [HbT] in the canine prostate *in vivo*, which reveals significant increase of the [HbT] at the cancer foci in a time-course of 6-weeks of tumor development. Such non-invasively acquired information of the hemoglobin contrast of prostate cancer over that of benign prostatic tissue, which shall be a result of tumor vasculature change, may improve the overall accuracy of prostate cancer detection by coupling the ultrasonography with NIR tomography.

2. Materials and Methods

The system is upgraded from our previously demonstrated integrated trans-rectal NIR/US sagittal-imaging system [11]. The outputs from one 785nm and one 830nm laser diodes (Thorlabs Inc.) are combined by a bifurcated fiber (FiberTech Optica Inc.), as shown in Fig. 1 (a), and sequentially delivered to the 7 source channels of NIR applicator via a fiber switch made with a linear translation stage (Zaber Technology Inc.). The 7 detection channels are coupled to a 300mm focal-length spectrometer (Acton Research) for separating the two bands of remitted light. The acquisition of the spectrally separated light by a 16-bit intensified CCD camera (Princeton Instruments) is synchronized with the sequential source illumination. The acquisition time for one set of data was 3 seconds.

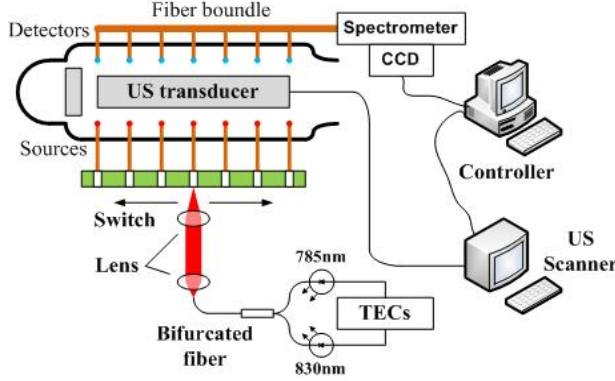


Fig. 1 (a) Dual-band trans-rectal NIR/US imaging system

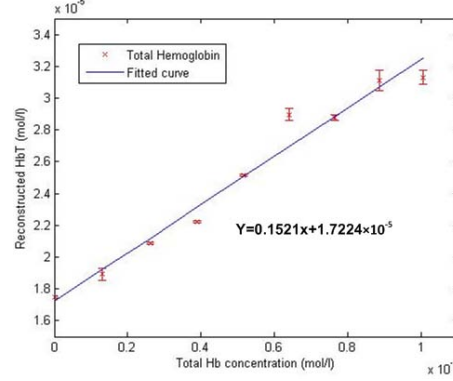


Fig.1 (b) System calibration with bovine blood

The calibration of the measurement of [HbT] was conducted with fresh bovine blood, whose optical absorption spectra in 600-850nm are very close to that of human blood [12]. The blood was held in a cylinder-container with $\mu_a=0.006\text{mm}^{-1}$ and $\mu_s'=1.0\text{mm}^{-1}$, which was embedded in a 1% bulk Intralipid solution ($\mu_a=0.0023\text{mm}^{-1}$ and $\mu_s'=1.0\text{mm}^{-1}$). The blood was diluted with an isotonic saline solution to establish a hemoglobin concentration gradient. The [HbT] of the fresh bovine blood is 12.8 ± 0.8 grams per 100cc [13]. The absorption coefficients at the two bands were reconstructed without spatial *prior* information of the cylinder, then the [HbT] was calculated by:

$$[HbT] = [HbO_{(Oxygenized)}] + [Hb_{(Deoxygenized)}] = \frac{\mu_a^{\lambda_1} \cdot e^{\lambda_2} - \mu_a^{\lambda_2} \cdot e^{\lambda_1}}{e^{\lambda_1} \cdot e^{\lambda_2} - e^{\lambda_2} \cdot e^{\lambda_1}} + \frac{\mu_a^{\lambda_1} \cdot e^{\lambda_2} - \mu_a^{\lambda_2} \cdot e^{\lambda_1}}{e^{\lambda_1} \cdot e^{\lambda_2} - e^{\lambda_2} \cdot e^{\lambda_1}} \quad (1)$$

where “ e ” denotes the extinction coefficient. The measurements given in Fig. 1(b) reveal a residue error in the reconstructed [HbT] when no blood was present, albeit it indicates a linear relationship between the reconstructed [HbT] above that residue value and the actual [HbT], which thereafter was applied to calibrating the *in vivo* results.

The animal protocols were approved by the Institutional Animal Care and Use Committee of Oklahoma State University. The canine protocol was also approved after an on-site inspection by the U.S. Army Medical Research and Material Command. For this study, the prostate of a 20-kg sexually intact mix-bred Beagle dog estimated to be approximately six years of age was used. The TVT cell line was propagated in non-obese-diabetic/severe combined-immunodeficiency (NOD/SCID) mice. The neoplastic TVT cells were recovered and homogenized for injection into the canine prostate gland. Approximately 3 cc of TVT cells were aseptically injected transperineally into the right lobe of the prostate using a 6-in. 16-gauge hypodermic needle via TRUS visualization. The TVT cells were confined within the right prostatic lobe during the injection in two locations, one near the cranial aspect, and the second slightly caudal to the mid-point of the right lobe as the needle was withdrawn. The dog underwent weekly monitoring, including physical rectal examination, TRUS, and trans-rectal NIR tomography, for 7 weeks and was then humanly euthanized for necropsy and histological examinations. Color and power Doppler TRUS evaluations performed at and after 5-weeks revealed blood circulating to the clearly hypo-echoic tumor masses.

3. Results

The sagittal TRUS/NIR imaging view taken across the right lobe of the prostate is given in Fig. 2 (a), and the NIR [HbT] images are presented in Fig. 3. The image dimension is 60mm×30mm (cranial-caudal×dorsal-ventral) for both US and NIR. A cluster of prostatic cysts looking like a “face” were used as a landmark to facilitate multiple images to be taken in the same relative areas over time throughout the course of the imaging study. Week 0 was the baseline images measured before the TVT cell injection. The base-line [HbT] is approximately 150uMol, that is in the lower range of the values of human prostate obtained by invasive time-resolved method [14]. At week 3, the tumor in the right lobe became visible in NIR images with a higher contrast while it was ambiguous in US images. The TVT continued to expand and became a large, infiltrative mass by week 6. Post mortem examination confirmed multiple coalescing foci of TVT in the caudal aspect of the prostate, and significant infiltration of the tumor from the

right lobe to the left lobe that was also indicated earlier by other NIR images. Histological examination of prostate sections confirmed TVT. Fig. 2(b) depicts the changes of the peak and averaged [HbT] in a 10mm-diameter region-of-interest specified in Fig. 3. Approximately 300% increase of the [HbT] has been indicated.

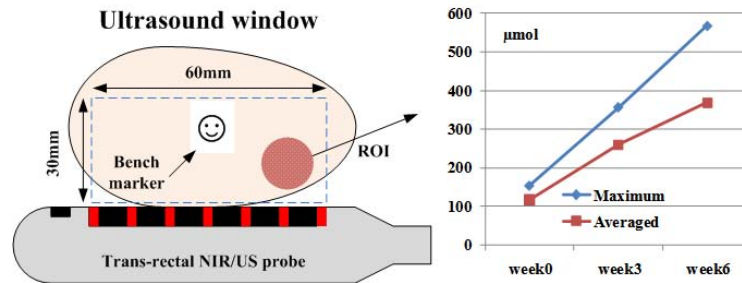


Fig. 2 (a). The view of sagittal US/NIR of the right lobe; (b) The changes of [HbT] at the region specified in Fig. 3, in week 0, 3 and 6

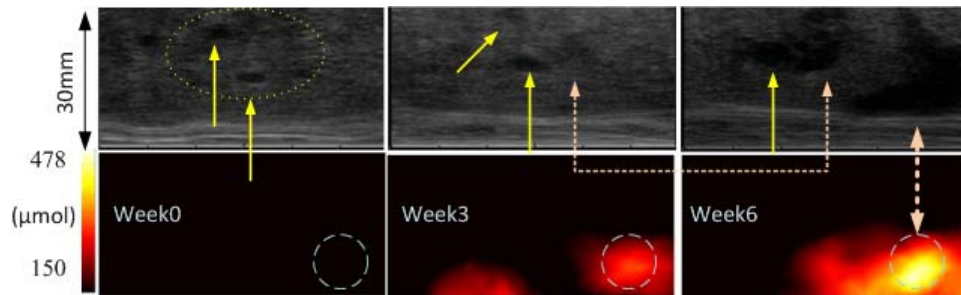


Fig. 3 The US and NIR images acquired at the right lobe, longitudinally in the middle-point and the caudal side, from week 0 to 6.

4. Discussions and Conclusions

This study reveals the first time non-invasive optical measurement of [HbT] changes associated with tumor development in the canine prostate. If spectral trans-rectal optical tomography can be implemented with an improved arrangement of the dual-bands or with more wavelength bands, the changes of oxygen saturation associated with tumor progression may be detected along with the elevations of [HbT], thereby providing another dimension of information for non-invasively characterizing the prostate cancer.

5. Acknowledgement

The study has been supported by **DOD Prostate Cancer Research Program through a New Investigator Award to Piao (PC060814)**, and an endowment fund to Bartels from the Kerr Foundation, Oklahoma City, Oklahoma.

6. Reference

- [1] Wild J, Reid J, "Echographic tissue diagnosis," Fourth Annual Conference on Ultrasound Therapy, Philadelphia, PA, 1955
- [2] Watanabe H, Kaiho J, Tanaka M, Terasawa Y, "Diagnostic application of ultrasonography of the prostate." *Invest Urol.*; **8**:548-559 (1971).
- [3] Brawer M. Chetner M. "Ultrasonography of the prostate biopsy," in Campbell's Urology, Walsh P, Retick A, Vaughna EJ, Wein A, eds., W.B. Saunders Company, Philadelphia, pp. 2506-2518 (1998).
- [4] Ellis WJ, Brawer MK, "The significance of isoechoic prostate carcinoma," *J. Urol.*; **152**: 2304-2307 (1994).
- [5] Loch AC, Bannowsky A, Baeurle L, Grabski B, König B, Flier G, Schmitz-Krause O, Paul U, Loch T, "Technical and anatomical essentials for transrectal ultrasound of the prostate," *World J. Urol.* **25**, 361-366 (2007).
- [6] Yaseen MA, Brecht HPF, Ermilov SA, Gharieb RR, Conjusteau A, Oraevsky AA, "Hybrid optoacoustic and ultrasonic imaging system for detection of prostate malignancies," *Proc. SPIE*, **6856**, 68560T (2008).
- [7] Boutet J, Herve L, Debourdeau M, Guyon L, Peltie P, Dinten JM, Saroul L, Duboeuf F, Vray D, "Bimodal ultrasound and fluorescence approach for prostate cancer diagnosis," *J. Biomed. Opt.*; **14**: 064001-1-064001-7 (2009).
- [8] Jiang Z, Holyoak GR, Bartels KE, Ritchey JW, Xu G, Bunting CF, Slobodov G, Piao D, "In vivo trans-rectal ultrasound coupled near-infrared optical tomography of a transmissible venereal tumor model in the canine pelvic canal," *J. Biomed. Opt. Lett.*, **14**(3): 030506-1-030506-3 (2009)
- [9] Bigler SA, Deering RE, and Brawer MK, "Comparison of microscopic vascularity in benign and malignant prostate tissue," *Hum Pathol.* **24**(2):220-6 (1993).
- [10] Zhu Q, Cronin EB, Currier AA, Vine HS, Huang M, Chen N, Xu C. "Benign versus malignant breast masses: optical differentiation with US-guided optical imaging reconstruction," *Radiology*; **237**(1):57-66 (2005).
- [11] Jiang Z, Piao D, Xu G, Ritchey JW, Holyoak GR, Bartels KE, Bunting CF, Slobodov G, Krasinski JS, "Trans-rectal ultrasound-coupled near-infrared optical tomography of the prostate Part II: Experimental demonstration," *Optics Express*, **16**(22): 17505-17520 (2008)
- [12] Hayes MD, Vanzant ES, Stombaugh TS, Gates RS, "Comparison of bovine blood absorption coefficients to human curves," *Livestock Environment VIII, Proceedings*, 981-985 (2008).
- [13] McCay CM, "The hemoglobin and total phosphorus in the blood of cows and bulls," *J. Dairy Sci.*, **14** (4): 373-378 (1931).
- [14] Svensson T, Andersson-Engels S, Einarsdóttir M, Svanberg K, "In vivo optical characterization of human prostate tissue using near-infrared time-resolved spectroscopy," *J Biomed Opt.*; **12**(1): 014022-1-014022-10 (2007).

The pain and gain of DC-based diffuse optical tomography reconstruction---New insights into an old-like problem

Guan Xu,¹ Daqing Piao,^{1*} Charles F. Bunting,¹ Hamid Dehghani²

¹ School of Electrical and Computer Engineering, Oklahoma State University
Stillwater, OK, 74078-5032, USA

² University of Birmingham, Birmingham, UK

*Corresponding Author: daqing.piao@okstate.edu

Abstract: For diffuse optical tomography reconstruction, DC-based method outperforms frequency-domain method in background artifacts, at the known cost of increased coupling between absorption and scattering. The differences of these methods diminish when spatial *priors* are available.

©2010 Optical Society of America

OCIS codes: (170.3880) Medical and biological imaging; (170.3010) Image reconstruction techniques; (170.6960) Tomography; (170.5270) Photon density waves

1. Introduction

Diffuse optical tomography quantifies the spatial heterogeneities of NIR absorbing chromophors and scattering particles by measurement of light diffused through biological tissue. Steady-state and frequency-domain (FD) measurements are most commonly utilized to reconstruct the tissue absorbance and scattering distributions. Steady-state system only measures the attenuation of the direct-current (DC) amplitude of the photon while frequency domain system ideally acquires the same DC, the amplitude of the modulated light intensity (AC), and the phase of the modulation of the light intensity (referred to as “Phs” in this paper). The role of DC component in FD reconstruction has yet to be comprehensively analyzed and the confidence level of reconstruction with only the DC information available has yet to be clearly understood.

This paper compares the image reconstructions using three sets of measurements, which are DC only, AC/Phs and DC/AC/Phs, to evaluate the role of DC information in diffuse optical tomography reconstruction. It is found that, DC-based method outperforms FD method in background artifacts, at the known cost of increased coupling between absorption and scattering, and the differences of the methods diminish when spatial *priors* can be implemented.

2 Theory

Under the assumption of accurate forward computational model to describe the light propagation, it is necessary to consider two factors when evaluating the overall performance of the reconstruction: First, the assembled measurement error that could be mapped to the uncertainty in image reconstruction; Second, the determinacy of the inverse problem.

2.1 Analyses of the parameter recovery uncertainty caused by assembled measurement error (PRUAME)

The measurements for both FD and CW systems are typically governed by the diffusion approximation to the radiative transfer equation[1]. For the simplest case of recovering the optical properties of an infinite homogeneous medium, the photon densities for DC and FD measured at a position \vec{r}' that has a distance of d from a source at \vec{r} are:

$$U_{DC}(\vec{r}, 0) = \frac{S_{DC}(\vec{r}', 0)}{4\pi Dd} \exp\left(-\sqrt{\frac{\mu_a}{D}}d\right); \quad (1)$$

$$U_{AC}(\vec{r}, \omega) = \frac{S_{AC}(\vec{r}', \omega)}{4\pi Dd} \exp\left(-d \sqrt{\frac{\mu_a}{2D} \left(1 + \frac{\omega^2}{v^2 \mu_a^2} + 1\right)}\right) \cdot \exp\left(id \sqrt{\frac{\mu_a}{2D} \left(1 + \frac{\omega^2}{v^2 \mu_a^2} - 1\right)}\right) \quad (2)$$

Therefore the measurements made at source-detector separations of d_1 and $d_2 = d_1 + \rho$, respectively, may results in the following parameters: δ --attenuation of steady state light intensity (DC); α --attenuation of the amplitude of the modulated light intensity (AC); ϕ --phase shift of the modulation of the light intensity (Phs), as

$$\delta = \ln \frac{(d_2 |U_{DC}(d_2)|)}{(d_1 |U_{DC}(d_1)|)} = -\rho \cdot \sqrt{\frac{\mu_a}{D}}; \alpha = \ln \frac{(d_2 |U_{AC}(d_2)|)}{(d_1 |U_{AC}(d_1)|)} = -\rho \cdot \sqrt{\frac{\mu_a}{2D} \left(1 + \frac{\omega^2}{v^2 \mu_a^2} + 1\right)}; \phi = \Phi(d_2) - \Phi(d_1) = \rho \cdot \sqrt{\frac{\mu_a}{2D} \left(1 + \frac{\omega^2}{v^2 \mu_a^2} - 1\right)} \quad (3)$$

For small variations of the source-detector distance among different source-detector pairs, the signal variations may actually be sensed as the “assembled measurement error” [2]. Suggested by [2], the “**parameter recovery uncertainty caused by assembled measurement error**” (PRUAME) is derived for the reconstruction methods of DC, AC/Phs, and DC/AC/Pha, with respect to each unknown quantities, as shown in Table 1.

Table 1 PRUAME expressions.

	$\sigma_{\mu a}/\mu_a$		σ_D/D	$\sigma_{\mu s'}/\mu_{s'}$
DC	$2 \cdot \left(\frac{\sigma_\delta^2}{\delta^2} \right)^{1/2}$ [2]		$2 \cdot \left(\frac{\sigma_\delta^2}{\delta^2} \right)^{1/2}$	$\left[\left(\frac{1}{3D} \right)^2 + \mu_a^2 \right]^{1/2} \cdot 2 \left(\frac{\sigma_\delta^2}{\delta^2} \right)^{1/2} \cdot \left[\frac{1}{3D} - \mu_a \right]^{-1}$
	Est. Val.	2	2	2
AC/ Phs	$\frac{\alpha^2 + \phi^2}{\alpha^2 - \phi^2} \left(\frac{\sigma_\phi^2}{\phi^2} + \frac{\sigma_\alpha^2}{\alpha^2} \right)^{1/2}$ [2]		$\left(\frac{\sigma_\alpha^2}{\alpha^2} + \frac{\sigma_\phi^2}{\phi^2} \right)^{1/2}$	$\left[\left(\frac{1}{3D} \right)^2 \left(\frac{\sigma_\alpha^2}{\alpha^2} + \frac{\sigma_\phi^2}{\phi^2} \right) + \mu_a^2 \cdot \left(\frac{\alpha^2 + \phi^2}{\alpha^2 - \phi^2} \right)^2 \cdot \left(\frac{\sigma_\alpha^2}{\alpha^2} + \frac{\sigma_\phi^2}{\phi^2} \right) \right]^{1/2} \cdot \left[\frac{1}{3D} - \mu_a \right]^{-1}$
	Est. Val.	1.6189	1.4142	~1.4142
AC/ DC/ Phs	$\left(\frac{\sigma_\phi^2}{\phi^2} + \frac{\sigma_\alpha^2}{\alpha^2} + 4 \frac{\sigma_\delta^2}{\delta^2} \right)^{1/2}$		$\left(\frac{\sigma_\alpha^2}{\alpha^2} + \frac{\sigma_\phi^2}{\phi^2} \right)^{1/2}$	$\left[\left(\frac{1}{3D} \right)^2 \left(\frac{\sigma_\alpha^2}{\alpha^2} + \frac{\sigma_\phi^2}{\phi^2} \right) + \mu_a^2 \cdot \left(4 \frac{\sigma_\delta^2}{\delta^2} + \frac{\sigma_\alpha^2}{\alpha^2} + \frac{\sigma_\phi^2}{\phi^2} \right) \right]^{1/2} \cdot \left[\frac{1}{3D} - \mu_a \right]^{-1}$
	Est. Val.	2.4495	1.4142	~1.4142

To quantitatively compare the magnitude of the expressions, optical properties close to those of actual tissue, $\mu_a=0.005\text{mm}^{-1}$, $\mu_s'=0.005\text{mm}^{-1}$, and detector separation of $\rho=10\text{mm}$ are substituted into the previous equations. Further assumptions are made by the assumption that the error magnitudes are the same for all the measurements ($\frac{\sigma_\delta^2}{\delta^2} \cong \frac{\sigma_\alpha^2}{\alpha^2} \cong \frac{\sigma_\phi^2}{\phi^2}$) as indicated in [2]. By normalizing the values along column 2 and 3 with $\frac{\sigma_\delta}{\delta}$ and column 4 with $\frac{\sigma_\delta}{\delta} \cdot \left[\frac{1}{3D} - \mu_a \right]^{-1}$, the reconstruction uncertainties are given in Table 1 as the “estimated value”.

Comparison in Table 1 indicates that from only the PRUAME perspective, AC/Phs possesses the least overall reconstruction uncertainty, followed by AC/DC/Phs and DC only.

With ref [3,4], the above analyses for the PRUAME comparisons based on infinite medium can be extended to semi-infinite medium and reaches qualitatively similar estimations.

2.2 Inverse problem determinacy

The inverse problem includes two scenarios. When the spatial *prior* is unavailable, more independent measurements are desired to reduce the under-determinacy condition of piecewise reconstruction. Under such consideration, DC/AC/Phs measurement could be the most deterministic measurement combination, although DC components are sometimes ignored in the sense that it may be redundant to the AC components. However, by comparing the 2nd and 3rd sub-equations in equ (3), it can be concluded that the AC attenuation usually is not linearly proportional to the DC attenuation, therefore DC information may be necessary for complete recovery of tissue properties.

When a complementary imaging modality is available to provide a hard *a priori* to the image reconstruction [5], the inverse problem becomes over-determined. Under such condition, it is imperative to know how well DC-based image reconstruction performs as compared to the cases of having FD information available.

3 Simulations

Numerical methods are conducted to investigate the validity of the above theoretical analyses. The forward model is formulated with finite element method based on diffusion approximation and Robin type boundary condition [6]. The sensitivity matrices (Jacobian) are structured as the one in below, for each measurement category in Fig. 1

$$J = \begin{bmatrix} \frac{\partial \ln I_{AC}}{\partial \mu_a} & \frac{\partial \ln I_{AC}}{\partial D} & \frac{\partial \phi}{\partial \mu_a} & \frac{\partial \phi}{\partial D} & \frac{\partial \ln I_{DC}}{\partial \mu_a} & \frac{\partial \ln I_{DC}}{\partial D} \end{bmatrix} \quad (4)$$

The DC/AC/Phs combination utilizes all the measurements so it contains all terms shown in equ. (4); while for CW method, only the last two terms in equ (4) are used and the first four terms are retained for AC/Phs method. The Levenberg-Marquardt algorithm is integrated as the inverse solver for the simulative evaluations.

3.1 Piece-wise simulation

The simulation is to solve for the optical properties at 2760 nodes in FEM mesh 240 (16×15), the location and maximum optical properties (shown on the bar chart) within each target region are shown in Fig.1. For the target profile and optical property recovery, DC only reconstruction demonstrates lowest accuracy and most significant

crossstalk. DC/AC/Phs outperforms AC/Phs in most cases, especially for the μ_a contour of target 3 and μ_s/D value recovery of target 2. However, the background variations (σ^2 value of each reconstructed image) indicate that DC only reconstruction presents the best background homogeneity, followed by DC/AC/Phs and AC/Phs. The background homogeneity in image reconstruction is especially important for DOT of prostate cancer, because the cancer target is to be resolved within the optically heterogeneous prostatic tissue.

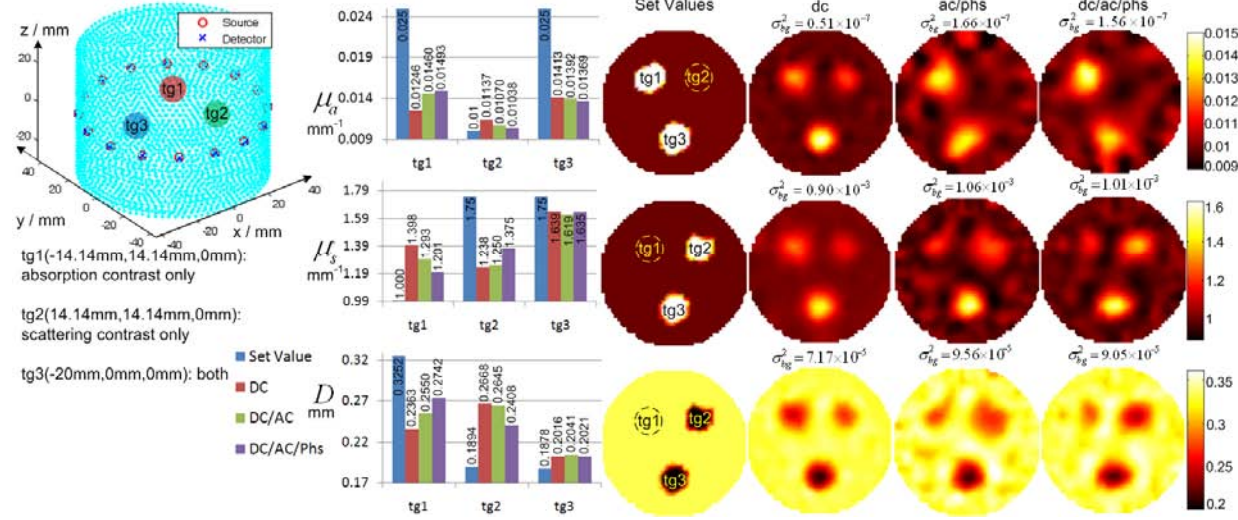


Fig.1 Piece-wise reconstruction

3.2 Region-wise simulation

With the same setup as the piecewise simulation and the assumption that the target region can be accurately segmented, region-wise reconstructions found that the DC only method, having less measurements, performs equivalently to the two methods with the FD information included.

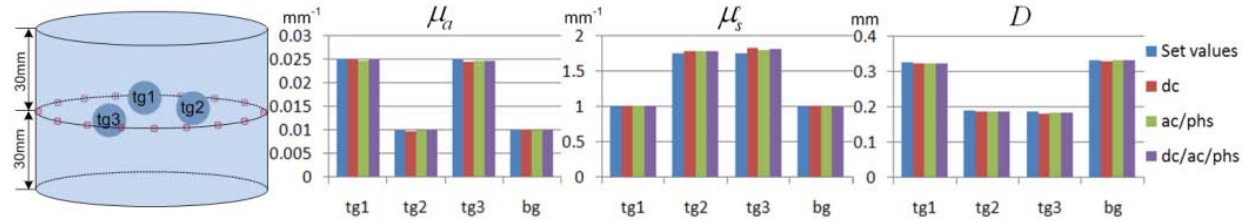


Fig.2 Region-wise reconstruction

4 Conclusions

The theoretical analysis and numerical studies have several implications to make: (1) DC-only piece-wise reconstruction outperforms other methods in background artifacts reduction but its performance on the target recovery accuracy and cross coupling suppression is less desirable; (2) DC/AC/Phs approach shows superiority over AC/Phs in piecewise reconstruction; (3) DC only region-wise reconstruction is equivalent to that based on FD system when the spatial *a priori* constraint is available.

Acknowledgment

This work has been supported in part by **DOD Prostate Cancer Research Program through a grant #W81XWH-07-1-0247**, and Oklahoma Center for the Advancement of Science and Technology (OCAST) through a grant HR06-171.

References

- [1] S. R. Arridge, "Optical tomography in medical imaging," *Inverse Probl.* 15, R41–R93(1999).
- [2] S. Fantini, M. A. Franceschini, J. B. Fishkin, B. Barbieriand, and E. Gratton, "Quantitative determination of the absorption spectra of chromophores in strongly scattering media: a light-emitting-diode based technique," *Appl. Opt.* 33, 5204-5213 (1994).
- [3] K. K. Wang and T. C. Zhu, "Reconstruction of in-vivo optical properties for human prostate using interstitial diffuse optical tomography," *Opt. Exp.* 17, 11665-11672 (2009).
- [4] S. Fantini, M. A. Franceschini, and E. Gratton, "Semi-infinite-geometry boundary problem for light migration in highly scattering media: a frequency-domain study in the diffusion approximation," *J. Opt.*
- [5] G. Xu, D. Piao, C. H. Musgrove, C. F. Bunting, and H. Dehghani, "Trans-rectal ultrasound-coupled near-infrared optical tomography of the prostate Part I: Simulation," *Opt. Exp.* 16, 17484–17504 (2008).
- [6] Z. Yuan and H. Jiang, "Image reconstruction scheme that combines modified Newton method and efficient initial guess estimation for optical tomography of finger joints," *Appl. Opt.* 46, 2757-2768 (2007).